# Underground flow, numerical methods and high performance computing

Nabil Birgle

# Thèse de doctorat

*présentée à*

## l'université pierre et marie curie

École Doctorale de
Science Mathématiques de Paris Centre (ED386)

*par*

**Nabil Birgle**

*pour obtenir le grade de*

Docteur

Spécialité : Mathématiques Appliquées

# *Écoulement dans le sous-sol, méthodes numériques et calcul haute performance*

Directeur de thèse : Jérôme Jaffré

Soutenue le 24 mars 2016
Devant la commission d'examen formée de :

| | | |
|---|---|---|
| M. Yvan Yotov | Université de Pittsburgh | Rapporteur |
| M. Robert Eymard | Université Paris-Est | Examinateur |
| M. Frédéric Hecht | Université Paris VI | Examinateur |
| M. Roland Masson | Université de Nice | Examinateur |
| M. Stéphane Lanteri | Inria Sophia Antipolis | Examinateur |
| M. Laurent Loth | Andra | Examinateur |
| Mme. Jean E. Roberts | Inria Paris | Examinateur |
| M. Jérôme Jaffré | Inria Paris | Directeur de thèse |

# A Thesis

*presented at*

## UNIVERSITY OF PIERRE ET MARIE CURIE

Doctoral School of
Mathematical Sciences of Central Paris (ED386)

*by*

**Nabil Birgle**

*to obtain the degree of*

Doctor

Speciality: Applied Mathematics

# *Underground flow, numerical methods and high performance computing*

Thesis advisor: Jérôme Jaffré

Defended on 24th March, 2016
In front of the examination committee consisting of:

| | | |
|---|---|---|
| Mr. Yvan Yotov | The University of Pittsburgh | Reviewer |
| Mr. Robert Eymard | The University of Paris-Est | Examiner |
| Mr. Frédéric Hecht | The University of Paris VI | Examiner |
| Mr. Roland Masson | The University of Nice | Examiner |
| Mr. Stéphane Lanteri | Inria Sophia Antipolis | Examiner |
| Mr. Laurent Loth | Andra | Examiner |
| Ms. Jean E. Roberts | Inria Paris | Examiner |
| Mr. Jérôme Jaffré | Inria Paris | Thesis advisor |

# Résumé

Nous construisons une méthode numérique fiable pour simuler un écoulement dans un milieu poreux modélisé par une équation elliptique. La simulation est rendue difficile par les hétérogénéités du milieu, la taille et la géométrie complexe du domaine de calcul.

Un maillage d'hexaèdres réguliers ne permet pas de représenter fidèlement les couches géologiques du domaine. Par conséquent, nous sommes amenés à travailler avec un maillage de cubes déformés. Il existe différentes méthodes de volumes finis ou d'éléments finis qui résolvent ce problème avec plus ou moins de succès. Pour la méthode que nous proposons, nous nous imposons d'avoir seulement un degré de liberté par maille pour la pression et un degré de liberté par face pour la vitesse de Darcy, pour rester au plus près des habitudes des codes industriels. Comme les méthodes d'éléments finis mixtes standards ne convergent pas, notre méthode est basée sur un élément fini mixte composite.

En deux dimensions, une maille polygonale est découpée en triangles en ajoutant un point au barycentre des sommets, et une expression explicite des fonctions de base a pu être obtenue. En dimension 3, la méthode s'étend naturellement au cas d'une maille pyramidale. Dans le cas d'un hexaèdre ou d'un cube déformé quelconque, la maille est divisée en 24 tétraèdres en ajoutant un point au barycentre des sommets et en divisant les faces en 4 triangles. Les fonctions de base de l'élément sont alors construites en résolvant un problème discret. Les méthodes proposées ont été analysées théoriquement et complétées par des estimateurs a posteriori. Elles ont été expérimentées sur des exemples académiques et réalistes en utilisant le calcul parallèle.

**Mot clés :** éléments finis mixtes, éléments finis composites, maillage polygonal, maillage hexahedrique, maillage pyramidal, écoulement en milieu poreux.

# Abstract

We develop a reliable numerical method to approximate a flow in a porous media, modeled by an elliptic equation. The simulation is made difficult because of the strong heterogeneities of the medium, the size together with complex geometry of the domain.

A regular hexahedral mesh does not allow to describe accurately the geological layers of the domain. Consequently, this leads us to work with a mesh made of deformed cubes. There exists several methods of type finite volumes or finite elements which solve this issue. For our method, we wish to have only one degree of freedom per element for the pressure and one degree of freedom per face for the Darcy velocity, to stay as close to the habits of industrial software. Since standard mixed finite element methods does not converge, our method is based on composite mixed finite element.

In two dimensions, a polygonal mesh is split into triangles by adding a node to the vertices's barycenter, and explicit formulation of the basis functions was obtained. In dimension 3, the method extend naturally to the case of pyramidal mesh. In the case of a hexahedron or a deformed cube, the element is divided into 24 tetrahedra by adding a node to the vertices's barycenter and splitting the faces into 4 triangles. The basis functions are then built by solving a discrete problem. The proposed methods have been theoretically analyzed and completed by a posteriori estimators. They have been tested on academical and realistic examples by using parallel computation.

**Keywords:** mixed finite element, composite finite elements, polygonal mesh, hexahedral mesh, pyramidal mesh, flow in porous media.

# Remerciements

Je tiens à exprimer ma vive reconnaissance à mon directeur de thèse Jérôme Jaffré et à Jean E. Roberts, tous deux anciens Directeurs de recherche *Inria* qui m'ont accompagné et soutenu durant ma thèse. Je tiens à les remercier pour leurs gentillesses et les conseils qu'ils m'ont prodigué pendant toutes ces années de recherche. Je remercie également Laurent Loth, Ingénieur à l'*Andra* qui a rendu ce projet de thèse possible et qui a été mon contact au sein de cette établissement.

Je remercie Ivan Yotov, Professeur de mathématiques à l'université de Pittsburgh et Gianmarco Manzini, Directeur de recherche *Imati*, qui m'ont fait l'honneur d'être les rapporteurs de ma thèse et d'évaluer mon travail. Je remercie également Robert Eymard, Professeur de mathématiques à l'université Paris-Est Marne-la-Vallée, Roland Masson, Professeur de mathématiques à l'université Nice Sophia Antipolis et Stéphane Lanteri, Directeur de recherche *Inria* et responsable de l'équipe *Nachos*, pour avoir accepté de faire partie de mon jury.

Je tiens à remercier tous les membres l'équipe *Serena* (anciennement *Pomdapi*) avec qui j'ai eu un grand plaisir de travailler. Je remercie une nouvelle fois Jérôme Jaffré et Jean E. Roberts ainsi que Martin Vohralík, Directeur de recherche *Inria* et responsable de l'équipe pour leurs accompagnements et leurs conseils. Je remercie également mes nombreux collègues et amis que contient l'équipe *Serena* et avec qui j'ai développé des liens forts ces dernières années. Je pense notamment à Clément Franchini, Patrik Daniel, Fatma Cheikh, Sarah Ali Hassan, Jad Dabaghi, Cédric Josz, avec qui j'ai partagé mon bureau pendant un temps et aux autres membres de l'équipe Pierre Weis, Géraldine Pichot, Elyes Ahmed, Michel Kern, Iain Smears, Caroline Japhet, François Clément, Vincent Martin que j'ai croisé au quotidien. Je tiens aussi à saluer Mohamed Hedi Riahi et les anciens membres de l'équipe *Pomdapi*, Zuqi Tang, Ibtihel Ben Gharbia et Émilie Joannopoulos.

Je remercie une nouvelle fois Laurent Loth, Stéphane Lanteri et Tristan Cabel, Ingénieur de recherche de l'équipe *Nachos*, avec qui j'ai eu le plaisir de travailler et qui m'ont beaucoup aidé sur le développement du logiciel *Traces* de l'*Andra*.

Enfin, je tiens à remercier mes parents et mes proches qui m'ont beaucoup aidé et soutenu pendant toutes ces années, mes anciens collègues de l'*Onera* à Châtillon et mes futures collègues à Nice.

# Contents

**Résumé** **i**

**Abstract** **iii**

**Remerciements** **v**

**Introduction** **1**

**Chapter 1. The porous media and the transport of radioactive particles** **7**
1.1 Flow equations . . . . . 7
1.1.1 Darcy's law . . . . . 7
1.1.2 The equation of mass conservation . . . . . 9
1.2 Transport equation . . . . . 11

**Chapter 2. A 2-D Composite Polygonal Mixed Finite Element** **15**
2.1 Introduction . . . . . 15
2.2 Numerical analysis for mixed methods . . . . . 16
2.3 A composite method for polygons . . . . . 18
2.4 An explicit expression for the flux across the interior edges of a composite element . . . . . 21
2.5 A bound on the velocities . . . . . 23
2.5.1 A bound of the remainder . . . . . 23
2.5.2 Projection operators . . . . . 24
2.5.3 A bound of the rotating velocity . . . . . 25
2.6 A priori error estimation . . . . . 26
2.6.1 A bound of the projection operator for the velocities . . . . . 26
2.6.2 Error estimates . . . . . 27
2.7 Numerical experiments . . . . . 29
2.8 Conclusion . . . . . 29

**Chapter 3. Composite Methods on Irregular Hexahedral and Pyramidal Meshes** **33**
3.1 Introduction . . . . . 33
3.2 Mixed finite element methods . . . . . 35
3.3 Convergence of composite mixed finite elements . . . . . 38
3.4 A composite mixed finite element method for pyramids . . . . . 40
3.4.1 Definition of the method . . . . . 40
3.4.2 Interpolation errors for pyramidal mixed finite elements . . . . . 42
3.5 A composite mixed finite element method for polyhedra . . . . . 44

3.5.1 Definition of the composite mixed finite elements for polyhedra . . . 45
3.5.2 Projection errors of the composite mixed finite elements for polyhedra 47
3.6 Numerical experiments for convergence . . . . . 48
3.6.1 Numerical experiments with meshes having planar faces . . . . . 49
3.6.2 Numerical experiments with meshes having curved faces . . . . . 50
3.7 A posteriori error estimate . . . . . 53
3.7.1 Definition of the error estimators . . . . . 53
3.7.2 Numerical experiments . . . . . 55
3.8 A realistic numerical experiment with parallel computing . . . . . 56
3.9 Conclusion . . . . . 60
3.A Appendix: Trace inequalities . . . . . 60

**Bibliography** **63**

# List of Figures


1 Carte de la France avec les départements de la Meuse et la Haute-Marne, où peuvent être situés le dépôt de déchets radioactif Cigéo. . . . . 2
2 Les différents domaines de calculs utilisés pour la simulation. Au cours du temps, les particules radioactives s'échappent du colis de déchets et du centre de stockage, ce qui rend leur déplacement difficile à prévoir. . . . . 2
3 Scellement d'une alvéole de stockage . . . . . 3

1.1 Porous medium [58, p. 163] . . . . . 8

2.1 The mesh $\widetilde{\mathcal{T}}_E$ for a pentagon $E$ divided into 5 triangles . . . . . 18
2.2 The mesh $\widetilde{\mathcal{T}}_E$ with a constant velocity . . . . . 26
2.3 Rectangular meshes for $n = 8$ and $n = 16$. . . . . 30
2.4 Non rectangular meshes with fixed aspect ratio for $n = 8$ and $n = 16$. . . . . 31

3.1 The mesh $\mathcal{T}_E$ for a pyramid $E$, divided into 4 tetrahedra . . . . . 41
3.2 Coordinate system on a pyramid-shape element . . . . . 43
3.3 Examples of internal edges joining the barycenter of the vertices . . . . . 44
3.4 The mesh $\mathcal{T}_E$ for a cube $E$, divided into 24 tetrahedra . . . . . 45
3.5 Regular meshes with respectively 8, 64 and 512 hexahedra. . . . . 49
3.6 Family of hexahedral meshes with respectively 8, 64 and 512 hexahedra. . . . 50
3.7 Example of deformed hexahedron, where a constant velocity and its approximation are shown on a diagonal cross section. . . . . 51
3.8 Mesh of the domain $\Omega$ having curved faces. . . . . 51
3.9 Family of random meshes with respectively 8, 64 and 512 deformed cubes. . . 52
3.10 Domain $\Omega$ with the planes $x = \frac{1}{2}$ and $x = \frac{2}{3}$. The domain $\Omega_r$ is shown in red and $\Omega_g$ in green. The velocity is assumed to move 10 time slower in $\Omega_r$, according to the variation of $\mathbf{K}$. . . . . 57
3.11 Coefficients $\eta_E$, around the plane $x = \frac{1}{2}$ and on $x = \frac{2}{3}$ . . . . . 57
3.12 Approximate error computed using a mesh 4 times finer, $|||\mathbf{u}_h - \mathbf{u}_{\frac{h}{4}}|||_{*,E}$ around the plan $x = \frac{1}{2}$ and on $x = \frac{2}{3}$ . . . . . 57
3.13 Computational domain modeling Meuse/Haute Marne district. Pink area is refined locally using prisms. Solutions of both methods are studied on the blue cross section. . . . . 58
3.14 Trace of permeability tensor $\mathbf{K}$ in logarithmic scale . . . . . 58
3.15 Approximate pressure on the horizontal cross section of $\Omega$. . . . . 58
3.16 $\mathbf{L}^2$ norm of approximate velocities on the horizontal cross section of $\Omega$. . . . 59

3.17 $\mathbf{L}^2$ norm of velocity approximated by the $\mathbf{RTN}_0$ method extended to deformed cubes, on the horizontal cross section of $\Omega$. The norm is clipped to fit to the range of the composite method. The non-physic maximum jump is located inside the red circle. . . . . 59

# List of Tables


2.1 Error of the composite method on rectangular meshes. . . . . 30
2.2 Error of the $\mathbf{RT}_0$ method on the triangular submeshes of the rectangular meshes. . . . . 30
2.3 Error of the composite method on non rectangular meshes with fixed aspect ratio. . . . . 31
2.4 Error of the $\mathbf{RT}_0$ method on non rectangular meshes with fixed aspect ratio. 31

3.1 Convergence errors on regular hexahedral meshes in Figure 3.5 . . . . . 49
3.2 Convergence errors on regular pyramidal meshes obtained from hexahedral meshes shown in Figure 3.5 . . . . . 49
3.3 Convergence errors on the family of hexahedral meshes in Figure 3.6 . . . . . 50
3.4 Convergence errors on the family of pyramidal meshes obtained from hexahedral meshes shown in Figure 3.6 . . . . . 50
3.5 Convergence errors on the hexahedral meshes having curved faces in Figure 3.8 51
3.6 Convergence errors on the pyramidal meshes having curved faces obtained from hexahedral meshes shown in Figure 3.8 . . . . . 51
3.7 Convergence errors on the family of random hexahedral meshes in Figure 3.9 52
3.8 Convergence errors on the family of random pyramidal meshes obtained from hexahedral meshes shown in Figure 3.9 . . . . . 52
3.9 Convergence of the global a posteriori error estimate and an approximate error computed with a finer mesh. . . . . 57

# Introduction

En France, la construction d'un nouveau centre de déchets radioactifs nommé Cigéo est étudiée pour entreposer des déchets radioactif de haute activité ou de moyenne activité à vie longue. Ces déchets proviennent principalement de résidus générés par le traitement des combustibles nucléaire usés ou d'anciens composants situés à l'intérieur d'un réacteur nucléaire. Une zone favorable à la construction de Cigéo est située dans la Haute-Marne, représenté sur la Figure 1. Ce site a été choisis pour les propriétés de sa roche argileuse qui limitent la circulation souterrain de l'eau. Aucune faille n'a été détectée à proximité du centre de stockage et l'activité sismique est faible dans la région. Les déchets radioactifs seraient enterrés sous 500m de profondeur pour les isoler du milieu extérieur, mais leur stockage en milieu profond soulèvent d'importantes questions.

## Contexte

Un colis de déchets radioactif de haute activité affiché sur la Figure 2a, contient 70kg d'éléments radioactifs, mélangés avec 400kg de verre adapté au stockage et placés dans un conteneur en inox. Certains éléments sont hautement radioactifs et possèdent une durée de vie très longue, entre $10^3$ et $10^6$ années et peuvent générer de la chaleur. Les colis de déchets radioactifs sont entreposés temporairement pendant plusieurs décennies pour être refroidis, puis ils sont entreposés dans Cigéo dans des alvéoles de stockage. Les colis sont espacés à intervalle régulier pour limiter le réchauffement de la roche, sa température ne devant pas dépasser 90°C. Ensuite, la fermeture du centre de stockage est effectuée graduellement. Les colis de déchets sont sellés dans les alvéoles par un bouchon d'argile et de béton, comme sur la Figure 3. Les différentes galeries sont remblayées de la même manière avec l'agile collecté pendant la construction de Cigéo.

Cependant sur ces échelles de temps longues, les matériaux utilisés pour la construction de Cigéo vont se dégrader à cause de la présence d'eau dans la roche. L'écoulement de cette eau va entraîner une certaine concentration de particules radioactives en dehors du colis et du centre de stockage. Les risques de contaminations sont réduits par la très faible perméabilité de la roche, mais d'autres phénomènes physiques doivent être pris en compte[1]. Lors de la construction de Cigéo, une partie de la roche autour du centre de stockage sera endommagée. Les techniques de construction doivent être adaptées pour minimiser l'apparition de micro fractures dans la roche, qui augmenteraient sa perméabilité. Les propriétés de la roche argileuse réduisent également ce risque. À long terme, la dispersion des particules radioactives doit être étudiée sur l'ensemble du domaine géologique, ce qui

[1]Des informations complémentaires sont disponibles sur le site internet de l'*Andra*, `http://www.andra.fr` et du projet dédié à Cigéo, `http://www.cigéo.com`. Les informations recueillies proviennent des rapports d'activités de l'*Andra* : "Stockage réversible profond - étape 2009 : Options de conception du stockage en formation géologique profonde", et "Stockage réversible profond - étape 2009 : Options de réversibilité du stockage en formation géologique profonde".


**Figure 1** – Carte de la France avec les départements de la Meuse et la Haute-Marne, où peuvent être situés le dépôt de déchets radioactif Cigéo.


**(a)** Colis de déchets radioactifs de haute activité (70cm de diamètre)


**(b)** Schéma d'un centre de stockage (2km × 2km)

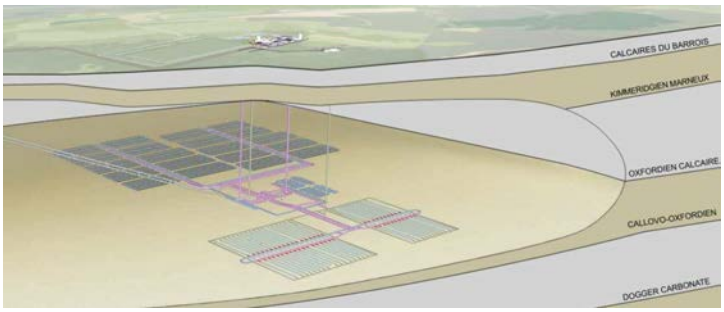


**(c)** Formation géologique autour du centre de stockage (20km × 20km × 500m)

**Figure 2** – Les différents domaines de calculs utilisés pour la simulation. Au cours du temps, les particules radioactives s'échappent du colis de déchets et du centre de stockage, ce qui rend leur déplacement difficile à prévoir.

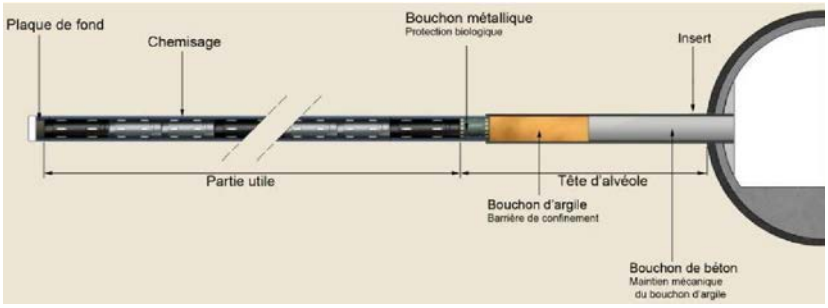


**Figure 3** – Scellement d'une alvéole de stockage

rend son évaluation difficile.

Mathématiquement parlant, on travaille sur des systèmes complexes d'équations aux dérivées partielles pour approcher les écoulement d'eau dans un milieu poreux souterrain, ainsi que le transport de particules radioactives. Il n'est pas possible de reproduire la complexité ce transport en laboratoire compte tenu de la lenteur du phénomène physique. C'est pourquoi la simulation numérique joue un rôle essentiel. Les caractéristiques particulières du problème posé se répercutent sur la résolution de ces équations :

- La simulation numérique utilisée pour résoudre les équations du modèle doit être fiable et efficace. Un intervalle de confiance doit être donné avec les résultats. De plus, certains paramètres comme la perméabilité du milieu proviennent d'estimation. Par conséquent, le temps de calcul de la simulation doit être raisonnable pour effectuer une étude de sensibilité par rapport à ces paramètres.

- La simulation fait intervenir des échelles de longueur différentes, de moins d'un mètre pour le colis de déchet radioactifs à plusieurs kilomètre pour le milieu géologique. De plus, ces différents domaines possèdent des propriétés hydrogéologiques propres. Le maillage utilisé pour la simulation doit être raffiné localement pour prendre en compte ces hétérogénéités et éviter des calculs inutiles.

- La géométrie du domaine est complexe. Le maillage peut inclure des faces courbes pour suivre le bord d'un colis de déchet radioactif, les galeries d'accès de Cigéo, ainsi que les différentes couches géologique du milieu. Le schéma numérique doit rester stable lorsque le maillage contient des faces courbes, tout en conservant un faible temps de calcul.

## Les éléments finis mixtes sur des maillages ayant des faces courbes

L'objectif de cette thèse est de développer une méthode numérique adaptée aux contraintes énumérées précédemment. Nous nous concentrons sur le cas des écoulements souterrains modélisés par une équation elliptique du second ordre. L'importance de ce travail tient au fait que le calcul d'un tel écoulement est ensuite utilisé pour simuler un transport de soluté, par exemple la propagation de particules radioactives dans le sous-sol, et évidemment la précision de cette simulation dépend beaucoup de la qualité du calcul de l'écoulement.

La nouvelle méthode que nous proposons fait partie de la famille des éléments finis mixtes [19, 68, 31]. Ce sont des méthodes localement conservatives, bien adaptées aux problèmes avec des tenseurs de perméabilité non-diagonaux et discontinus, ainsi qu'aux maillages de

triangles ou de tétraèdres et de carrés ou de cubes qui sont l'images d'une transformation linéaire de l'élément de référence. La méthode d'éléments finis mixtes de plus bas degré que nous notons $\mathbf{RTN}_0$ approche avec la même précision la variable scalaire, la pression, et la variable vectorielle, la vitesse de Darcy. Elle possède un degré de liberté par maille pour la pression et un degré de liberté par face, le flux, pour la vitesse de Darcy.

Cette méthode d'éléments finis mixtes est donc très proche des méthodes de volumes finis centrés sur les mailles [57, 44], et aussi des méthodes mimétiques [53, 56, 25]. De nombreux articles se sont intéressés aux relations étroites qui existent entre ces méthodes. Citons parmi d'autres [69, 52, 80, 11, 7, 6, 79, 81, 42, 78]. Des méthodes de volumes finis centrées sur les mailles [1, 46] et des méthodes mimétiques [26, 56] permettent maintenant de traiter les maillages d'hexaèdres quelconques.

Rappelons qu'en ce qui concerne la méthode des éléments finis mixtes, elle peut être aussi vue comme une méthode d'éléments finis non conforme avec un degré de liberté par face pour la pression [10, 28, 4, 30], mais pour des problèmes de stabilité numérique, la précision des résultats diminue si la perméabilité du domaine varie fortement d'une maille à l'autre [51].

La méthode des éléments finis mixtes a été développée et analysée par P.-A. Raviart, J.-M. Thomas et J.-C. Nédélec [66, 61]. Depuis les années 80, les méthodes mixtes se sont répandues dans de nombreuses applications, et en particulier pour résoudre des problèmes d'écoulement en milieu poreux, que ce soit pour l'hydrogéologie ou la simulation de réservoirs pétroliers. Citons par exemple [40, 41, 28, 33, 30, 65, 12, 36, 32, 47]. Dans le domaine du stockage de déchets radioactifs en milieu profond on peut citer [50, 70] et pour les écoulements dans un milieu fracturé [59, 35]. Pour ce qui est des estimations a posteriori on mentionnera simplement [82, 76, 77].

Le problème qui nous préoccupe dans cette thèse est l'extension de la méthode des éléments finis mixtes à des maillages d'hexaèdres (faces planes) ou même de cubes déformés (faces non planes). Ces éléments demandent une étude spécifique car la transformation vers un élément de référence (la transformation de Piola) n'est pas linéaire [15, 63, 60]. Des problèmes similaires apparaissent pour des pyramides. Des études préliminaires ont été faites en 2 dimensions [8, 72], montrant qu'une extension standard de la méthode $\mathbf{RTN}_0$ ne converge pas sur des maillages d'hexaèdres quelconques. Comme montré dans [49], cette erreur se répercute évidemment sur le calcul du transport de solutés.

Une manière d'obtenir la convergence de la méthode des éléments finis mixtes sur des maillages hexaèdriques quelconques est d'augmenter le nombre de degrés de liberté associés à la vitesse de Darcy [9, 81]. Une autre méthode consiste à ajouter un terme de stabilisation pour obtenir la convergence [39, 38]. Cependant, ces solutions augmentent le coût de calcul de la méthode. Une autre solution est de construire un élément composite. Un sous maillage tétraèdrique de l'élément est construit pour définir des fonctions de base polynomiales par morceaux sur l'élément, comme pour une méthode multi-échelle [78, 3]. On peut trouver dans [54, 55, 71] des propositions précédentes d'éléments finis composites. En particulier dans [71], les hexaèdres sont divisés en 5 tétraèdres et les faces en 2 sous faces triangulaires. Cependant, il n'est pas possible d'utiliser cette méthode sur un maillage ayant des faces courbes. En effet une face courbe est approchée par deux faces planes obtenues en joignant deux sommets opposés de la face, mais il y a deux choix possibles pour les sommets opposés, et si ces choix ne sont pas les mêmes pour les deux cubes déformés adjacents alors il se crée un vide dans le maillage.

Pour surmonter cette difficulté, et aussi obtenir de bonnes propriétés de symétrie, nous construisons un élément composite de 24 tétraèdres en ajoutant un point au barycentre des sommets. Les faces courbes sont alors approchées par 4 triangles. La problématique des faces courbes est détaillée de manière générale dans [63], avec une liste de méthodes abordant ce problème. Cet article montre que si le maillage contient des faces courbes, alors les vitesses

constantes n'appartiennent plus à l'espace d'approximation. Par conséquent, la convergence ne peut être obtenue que sous certaines conditions sur la manière de raffiner le maillage.

Avant d'aborder le cas des faces courbes, nous avons souhaité considérer le cas de la dimension 2. Une extension de la méthode $\mathbf{RT}_0$ a été développée dans [5] pour des maillages de quadrilatères quelconques. Il y est montré que la transformation de Piola non-linéaire modifie les fonctions de base de la vitesse, et introduit des vitesses dans le noyau de l'application $\mathrm{div}\colon \mathbf{H}(\mathrm{div}, E) \to L^2(E)$. Une décomposition de type Helmholtz-Hodge [16, 73] est utilisée pour identifier ces vitesses. Cette décomposition a été mise en évidence en 1990 dans [34, p. 51], elle décompose une vitesse continue comme la somme d'un gradient et d'un rotationnel possédant une divergence nulle. Son utilisation sur les espaces d'approximation des méthodes mixtes semble récent. La méthode présentée dans [5] conserve le même nombre de degré de liberté que la méthode $\mathbf{RT}_0$. Cependant elle n'a pas encore été étendue au cas de la dimension 3. Pour ce qui concerne notre méthode d'éléments finis composites, les cellules polygonales du maillage sont divisées en triangles en ajoutant un point au barycentre des sommets.

## Contenu de la thèse

Nous étendons la définition des éléments composites présentés dans [71] et [54, 55] en ajoutant un point au barycentre des sommets. Cette nouvelle décomposition de l'élément permet d'étudier la convergence de la méthode sur des maillages possédant des faces courbes.

Dans **le premier chapitre** de cette thèse, nous rappelons les modèles physiques et mathématiques les plus simples qui modélisent les écoulements d'eau ainsi que le transport de solutés dans le sous-sol. Dans cette thèse, nous nous concentrons sur le problème elliptique du second ordre.

Dans **le deuxième chapitre** nous définissons un élément fini composite en deux dimensions où une maille polygonale $E$ du maillage est divisée en triangles en ajoutant un point interne au barycentre des sommets de la cellule.

Les vitesses approchées de notre espace d'approximation sont déterminées par leur flux qui sont constants à travers les arêtes du maillage. La pression approchée est elle constante sur chaque maille. Les fonctions de base de la vitesse sont des fonctions de $\mathbf{H}(\mathrm{div}, E)$, qui sont définies sur chaque triangle du sous-maillage triangulaire comme des fonctions de l'espace $\mathbf{RT}_0$, espace des éléments finis mixtes de plus bas degré. Les fonctions de base de la vitesse sont déterminées par la valeur de leur flux à travers les arêtes du bord de $E$, elles sont à divergence constante sur $E$ comme pour la pression approchée. Enfin pour définir les fonctions de base de façon unique, on ajoute encore une condition éliminant la possibilité d'un champ de vitesse pouvant tourner autour du point interne. La définition et l'analyse de cet élément composite sont basées sur une décomposition des vitesses de l'espace de $\mathbf{RT}_0$ défini sur le sous-maillage triangulaire de $E$. Cette décomposition nous permet en même temps d'obtenir une expression explicite des fonctions de base. On termine ce chapitre par des expériences numériques confirmamt la validité des estimations a priori obtenues. Le chapitre fait l'objet de l'article [17] soumis à publication.

Nous définissons la méthode composite en 3 dimensions dans **le troisième chapitre**. Elle est définie à la fois pour des maillages d'hexaèdres et de pyramides. Le sous-maillage tétraèdrique de l'hexaèdre est construit en ajoutant un point au barycentre des sommets, et en divisant les faces en 4 sous-faces triangulaires. Celui d'une pyramide est construit en ajoutant un unique point à sa base pour la diviser en 4 tétraèdres. La méthode composite du second chapitre ne peut s'étendre à la dimension 3 que pour les maillage de pyramides. Dans le cas d'hexaèdres quelconques, un problème discret doit être résolu sur chaque élément pour

définir les fonctions de base. L'apparition de faces courbes dans le maillage est également étudiée numériquement : si elles sont approchées pendant le raffinement du maillage, alors la convergence de la méthode est obtenue. Une estimation d'erreur a posteriori de la méthode est ensuite présentée. Elle permet de majorer l'erreur commise sans connaitre la solution exacte. Un critère de raffinement local est également développé pour raffiner le maillage. Ensuite, nous testons la méthode composite sur un cas test concret regroupant les contraintes énoncées précédemment. La méthode composite a été implémentée dans le logiciel *Traces* de l'*Andra*, et est comparée avec une méthode $\mathbf{RTN}_0$ étendue à des maillages de cubes déformés. Le maillage utilisé décrit la formation géologique autour du centre de stockage. Il contient des faces courbes ainsi qu'un nombre important d'éléments. La méthode $\mathbf{RTN}_0$ étendue ne donne pas de bons résultats. Sur certains éléments la vitesse approchée atteint des valeurs non physiques qui perturbent le calcul de transport, alors que la méthode composite converge comme attendu.

# Chapter 1

# The porous media and the transport of radioactive particles

A porous medium as shown in Figure 1.1, is a solid structure containing pores that fluid or gas may go through. To facilitate our study, we assume that medium is saturated in water, i.e. that it contains only one fluid. Underground flows are estimated by performing a space average of fluid velocity over a representative elementary volume. Its size is chosen to be:

1. large enough to not distinguish differences between a pore and a grain,
2. small enough in oder that macroscopic quantities defined does not depends on its size.

Over an elementary volume, we define the total porosity of a solid $w$, which is the ratio of void volume over the solid volume,

$$w = \frac{\text{volume of voids}}{\text{volume of the solid}}.$$

Similarly, we define macroscopic quantities as pressure and fluid velocity, and we enunciate mathematical equations that must solve to estimate spreads of radioactive particles.

## 1.1 Flow equations

Underground flow is modeled by two equations: Darcy's law and the equation of mass conservation.

### 1.1.1 Darcy's law

Fluid moves through porous medium from highest energy levels to lowest. If we assume that only variations of pressure and gravity are enough strong to move fluid, we can approximate fluid flow in porous medium due to Darcy's law [58, Chapter 4]:

$$\mathbf{u} = -\frac{\mathcal{K}}{\mu}(\nabla P + \rho g \nabla z),$$

where

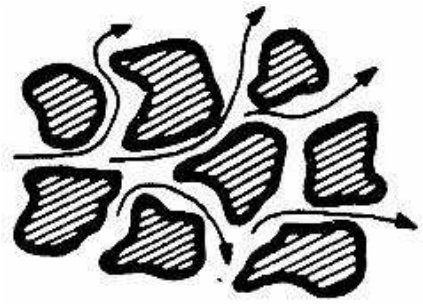

**Figure 1.1:** Porous medium [58, p. 163]

- $\mathbf{u}$ (m.s$^{-1}$) is Darcy's velocity. It is a space average of fluid velocity over an elementary volume.

- $\mathcal{K}$ (m$^2$) is the intrinsic permeability of the medium. It measures fluid abilities to flow through rocks, according to material type, temperature and links between pores. It does not depend on fluid characteristics. High permeability will allow fluids to move rapidly through rocks.

- $P$ (Pa) is the fluid pressure. It is an average value as for Darcy's velocity. We recall that Pa = N.m$^{-2}$ = kg.m$^{-1}$s$^{-2}$.

- $\mu$ (Pa.s) is the fluid dynamic viscosity.

- $\rho = \rho(P, c, \theta)$ (kg.m$^{-3}$) is the fluid density, which depends on fluid pressure, concentration of dissolved contaminants $c$ and temperature $\theta$.

- $g \simeq 9.8067$ (m.s$^{-2}$) is the magnitude of the gravitational acceleration.

- $z$ (m) is the height.

Darcy's law is valid only for slow and viscous flow. Moreover, if we assume that variations of fluid density are insignificant in space, then Darcy's velocity can be defined in two different ways:

$$\mathbf{u} = -\mathbb{K}\,\nabla\, h,$$

where

- $h = \frac{P}{\rho g} + z$ (m) is called the hydraulic head,

- $\mathbb{K} = \frac{\mathcal{K}\rho g}{\mu}$ (m.s$^{-1}$) is the hydraulic conductivity tensor. For a medium saturated in water, these coefficients vary from $10^{-2}$ (m.s$^{-1}$) for sand to $10^{-9}$ (m.s$^{-1}$) for clay. Moreover, if fluid flow is invariant in each direction of porous medium, then the medium is isotropic. In this case, intrinsic permeability together with hydraulic conductivity are scalar coefficients. Otherwise, hydraulic conductivity is a symmetric tensor,

$$\mathbb{K} = \begin{bmatrix} K_{xx} & K_{xy} & K_{xz} \\ K_{xy} & K_{yy} & K_{yz} \\ K_{xz} & K_{yy} & K_{zz} \end{bmatrix},$$

and the medium is said to be anisotropic. Choosing a coordinate system where axis follow characteristic directions of porous medium, hydraulic conductivity reduces itself to a diagonal tensor. Since geological layers are built by sediment deposit, we distinguish

a longitudinal permeability $K_{\mathrm{L}}$ and a transverse permeability $K_{\mathrm{T}}$. In the new coordinate system, we obtain

$$\mathbb{K} = \begin{bmatrix} K_{\mathrm{L}} & 0 & 0 \\ 0 & K_{\mathrm{L}} & 0 \\ 0 & 0 & K_{\mathrm{T}} \end{bmatrix}.$$

Second definition of Darcy's velocity is obtained from substitution $p = P + \rho g z$, which gives

$$\mathbf{u} = -\boldsymbol{K}\,\nabla p,$$

where

- $p$ (Pa) is the pressure,
- $\boldsymbol{K} = \frac{\mathcal{K}}{\mu}$ ($\mathrm{m^2 Pa^{-1} s^{-1}}$) is the permeability tensor. These properties are similar to hydraulic conductivity tensor.

### 1.1.2 The equation of mass conservation

This equation shows the principle of mass conservation of a fluid. In an elementary volume, mass variation of fluid over time is equal to the mass of injected of withdrawn fluid plus the sum of flows going through volume boundary. For porous medium, continuity equation is given in [58, Chapter 3] and [29] and writes

$$\frac{\partial(w\rho)}{\partial t} + \nabla\cdot(\rho\mathbf{u}) = \rho f,$$

where $f$ ($\mathrm{s^{-1}}$) is a sink or source term per volume unit. Since we have assumed that variations of fluid density are insignificant in space, previous equation becomes

$$\frac{1}{\rho}\frac{\partial(w\rho)}{\partial t} + \nabla\cdot\mathbf{u} = f.$$

Porosity and fluid density are functions depending on fluid pressure, which may varies in time. We define then the specific storage coefficient $s$ ($\mathrm{m^{-1}}$), such that

$$s = g\frac{\partial(w\rho)}{\partial P}.$$

It is used to measure capability of porous medium to release fluid in function of pressure variations. Introducing this variable, we highlight variations in time of fluid pressure,

$$\frac{s}{\rho g}\frac{\partial P}{\partial t} + \nabla\cdot\mathbf{u} = f.$$

Finally, we wish to replace fluid pressure by the hydraulic head. By definition, we have the relation $P = \rho g(h - z)$, which gives us

$$\left(1 - g(h-z)\frac{\partial\rho}{\partial P}\right)\frac{\partial P}{\partial t} = \rho g\frac{\partial h}{\partial t}.$$

The isothermal compressibility law set a relation between fluid density and pressure. For a constant temperature, we have

$$\beta_{\mathrm{l}} = \frac{1}{\rho}\frac{\partial\rho}{\partial P},$$

where $\beta_{\mathrm{l}}$ ($\mathrm{Pa}^{-1}$) is the fluid compressibility coefficient. However, this value is insignificant for fluids and approximate $\frac{\partial P}{\partial t} \simeq \rho g \frac{\partial h}{\partial t}$ is often performed [58, p. 82]. Adding Darcy's law, we obtain a closed system for a compressible flow with two unknowns, the scalar $h$ and the vector field $\mathbf{u}$:

$$\begin{aligned} \mathbf{u} &= -\mathbb{K} \nabla h, \\ s\frac{\partial h}{\partial t} + \nabla \cdot \mathbf{u} &= f. \end{aligned}$$

Remains to set behavior of the solution at the boundaries of the domain. Several kinds of limit conditions may be considered:

**Dirichlet boundary conditions** are used when hydraulic head at the boundary is set by a known function $h_{\mathrm{d}}$ which does not depends on Darcy's velocity inside the porous medium.

$$h = h_{\mathrm{d}}, \quad \text{on } \partial\Omega.$$

It is used for instance where the porous medium is in contact with a river.

**Neumann boundary conditions** set Darcy's velocities at the domain boundary:

$$\mathbf{u} \cdot \mathbf{n} = q_{\mathrm{n}}, \quad \text{on } \partial\Omega,$$

where $\mathbf{n}$ is the outgoing normal at the boundary, and $q_{\mathrm{n}}$ a function modeling a sink or a source term.

**Robin boundary conditions,** which are a mix between Dirichlet and Neumann boundary conditions. We have the relation

$$\mathbf{u} \cdot \mathbf{n} + \alpha h = q_{\mathrm{r}}, \quad \text{on } \partial\Omega,$$

where $\alpha$ and $q_{\mathrm{r}}$ are given. It may be used on lake border, when hydraulic head depends on Darcy's velocities of the medium.

**Periodic boundary conditions** can be set on both sides of the porous medium to simulate large domains.

If fluid characteristics vary in time, then we must specify hydraulic head at initial time. Otherwise, the system is in steady state and writes for homogeneous Dirichlet conditions ($h_{\mathrm{d}} = 0$):

$$\begin{aligned} \mathbf{u} &= -\mathbb{K} \nabla h && \text{in } \Omega, \\ \nabla \cdot \mathbf{u} &= f && \text{in } \Omega, \\ h &= 0 && \text{on } \partial\Omega, \end{aligned}$$

or equivalently,

$$\begin{aligned} \mathbf{u} &= -\boldsymbol{K} \nabla p && \text{in } \Omega, \\ \nabla \cdot \mathbf{u} &= f && \text{in } \Omega, \\ p &= 0 && \text{on } \partial\Omega. \end{aligned}$$

In this case, we also assume that concentration of particles dissolved in the fluid is enough small to not modify fluid density. Darcy's equations can be solved regardless of transport equation.

## 1.2 Transport equation

Transport equation is obtain by applying mass conservation law to particles dissolved in fluid. It involves complex phenomena which are presented in [58, Chapter 9] and in [13, Chapter 4] in general form. If the porosity is constant in time, transport equation writes

$$w\frac{\partial c}{\partial t} + \nabla\cdot \boldsymbol{j} = f,$$

where:

- $c$ (mol.l$^{-1}$) is the concentration of the dissolved contaminant in the fluid,
- $\boldsymbol{j} = \boldsymbol{j}_{\text{adv}} + \boldsymbol{j}_{\text{diff}} + \boldsymbol{j}_{\text{disp}}$ is the flux of chemical species, i.e. the amount of species going through a surface over time. We distinguish three mainly fluxes moving radioactive particles. First one is advection $\boldsymbol{j}_{\text{adv}}$, which is quantity of species being carried along by underground flows:

$$\boldsymbol{j}_{\text{adv}} = \mathbf{u}c.$$

- The second kind of flux is the molecular diffusion $\boldsymbol{j}_{\text{diff}}$ caused by Brownian motion of the molecules. In fluid phase, dissolved particles move in all directions. If the concentration of particles is uniform, then there is as many particles which come in and go out an elementary volume. Otherwise, molecular diffusion follows gradient of concentration. Its expression is given in liquid phase by Flick's law:

$$\widetilde{\boldsymbol{j}}_{\text{diff}} = -d_{\text{m}}\,\nabla\, c,$$

where $d_{\text{m}}$ (m$^2$s$^{-1}$) is the molecular diffusion coefficient of the medium, depending on temperature and dynamic viscosity of the fluid. However in porous medium, rock slows down brownian motion of particles, which leads us to use a smaller coefficient according to the medium porosity. If we denote $d_{\text{e}}$ (m$^2$s$^{-1}$) the effective diffusion coefficient of the medium, Flick's law writes for porous medium:

$$\boldsymbol{j}_{\text{diff}} = -d_{\text{e}}\,\nabla\, c.$$

The ratio between both coefficients may vary from 0.7 for sand to 0.1 for clay.

- Last studied flux is dispersion $\boldsymbol{j}_{\text{disp}}$, which is specific to porous media. Dispersion is caused by irregular flows going through pores of porous medium, which increases spread of dissolved particles. This phenomenon is ignored in advection because Darcy's velocity is an averaged velocity. The motion of particles is simulated using the gradient of concentration as molecular diffusion, but is guided by the dispersion tensor $\boldsymbol{D}_{\text{disp}}$ which depends on Darcy's velocity. Expression of dispersive flux is then

$$\boldsymbol{j}_{\text{disp}} = -\boldsymbol{D}_{\text{disp}}(\mathbf{u})\,\nabla\, c,$$

where the dispersion tensor is defined from Scheidegger's model:

$$\boldsymbol{D}_{\text{disp}}(\mathbf{u}) = \|\mathbf{u}\|(\alpha_{\text{L}}\boldsymbol{E}(\mathbf{u}) + \alpha_{\text{T}}(\boldsymbol{I} - \boldsymbol{E}(\mathbf{u}))),$$

with $\boldsymbol{I}$ the identity matrix,

$$\boldsymbol{E}_{i,j}(\mathbf{u}) = \frac{\mathbf{u}_i\mathbf{u}_j}{\|\mathbf{u}\|^2}, \qquad\qquad i,j = 1,\ldots,3,$$

and where $\alpha_{\mathrm{L}}$ and $\alpha_{\mathrm{T}}$ are the longitudinal and transverse dispersion coefficients. Longitudinal dispersion coefficient is usually larger than the transverse coefficient, which means that concentration of particles spreads faster in flow direction.

• $f = f_{\mathrm{c}} + f_{\mathrm{ads}} + f_{\mathrm{r}}$ models contributions or extinctions of the considered element. With $f_{\mathrm{c}}$ which represents a source term in the domain, we retain two other physic phenomena which alter concentration of radioactive particles in porous medium.

• First one is adsorption modeled by $f_{\mathrm{ads}}$ and simulating the deposit of particles on rock surface. Over an elementary volume, we define the mass concentration of particles $c_{\mathrm{s}}$, which is the mass of adsorbed particles divided by solid mass m (kg). If $\rho_{\mathrm{s}}$ is the mass density of the solid, then the solid mass $m = \rho_{\mathrm{s}}(1-w)$ over an elementary volume, and $\rho_{\mathrm{s}}(1-w)c_{\mathrm{s}}$ is particle mass sticked to the rock. Source term is the variation over time of particle mass,

$$f_{\mathrm{ads}} = -\rho_{\mathrm{s}}(1-w)\frac{\partial c_{\mathrm{s}}}{\partial t}.$$

There exists several adsorption laws linking particle concentration in liquid phase and at rock surface. We choose to model adsorption with the relation:

$$c_{\mathrm{s}} = Kc$$

where $K$ (ml.g$^{-1}$) is the adsorption constant. We assume then that adsorption is linear and reversible. Radioactive particles are not confined inside porous medium. Moreover, adsorption phenomenon is considered as instantaneous. For clay porous medium, steady state of both concentrations is obtained after few minutes, which is relatively fast compared with flow speed. Using this adsorption law in transport equation, we obtain

$$wR\frac{\partial c}{\partial t} + \nabla\cdot\boldsymbol{j} = f_{\mathrm{r}} + f_{\mathrm{c}},$$

where $R = 1 + \rho_{\mathrm{s}}\frac{(1-w)}{w}K$ is the retard coefficient. We can see that porous medium acts as a filter by slowing movement of radioactive particles.

• Second phenomenon is radioactivity expressed by $f_{\mathrm{r}}$. Over time, radioactive particles decay to other chemistry species by emitting radiations. The number of radioactive particles $n$ follows the law of radioactive decay

$$\frac{\partial n}{\partial t} = -\lambda n,$$

where $\lambda$ (s$^{-1}$) is the constant of radioactive decay. Solving this equation allow us to estimate the number of radioactive particles over time. If $n_0$ is the number of radioactive particles at time $t = 0$, then we have

$$n(t) = n_0 \exp(-\lambda t).$$

On average, half of radioactive particles are decaying at time $t_{1/2} = \lambda^{-1}\ln 2$ (s) which is defined as half-life of radioactive particles. Moreover, the behavior of radioactive particles is similar in liquid phase and in adsorbed phase. The mass of radioactive particles to consider over an elementary volume is $wc + \rho_{\mathrm{s}}(1-w)c_{\mathrm{s}}$ and then the source term $f_{\mathrm{r}}$ is

$$f_{\mathrm{r}} = -\lambda(wc + \rho_{\mathrm{s}}(1-w)c_{\mathrm{s}}) = -\lambda wRc.$$

During transport computing, we should take into account the presence of several radioactive

chemical species together with other chemical species resulting from their radioactivity but we neglect this aspect.

Combining all these physical phenomena, transport equation writes

$$wR\frac{\partial c}{\partial t} + \nabla\cdot(\mathbf{u}c - \boldsymbol{D}(\mathbf{u})\,\nabla\, c) - \lambda wRc = f_{\mathrm{c}},$$

where phenomena of molecular diffusion and dispersion have been gathered in the dispersion-diffusion tensor $\boldsymbol{D}(\mathbf{u})$,

$$\boldsymbol{D}(\mathbf{u}) = d_{\mathrm{e}}\boldsymbol{I} + \boldsymbol{D}_{\mathrm{disp}}(\mathbf{u}).$$

Dispersion often makes insignificant molecular diffusion except when flow speed is slow. As Darcy's system, transport equation must be completed with boundary conditions at domain border together with concentration of radioactive particles at initial time.

# Chapter 2

# A 2-D Composite Polygonal Mixed Finite Element

**Abstract**

General hexahedral and quadrangular grids present a challenge for mixed finite elements for second-order, elliptic problems. We define and analyze a mixed finite element method for a mesh made up of star-shaped polygons. The scalar unknown is approximated by element-wise constants and the vector unknown is determined by its flux through the edges of the polygons. The elements are composite elements. Each polygon is split into triangles by taking an interior point of the polygon, one for which it is star-shaped, and considering the triangles radiating from that point and having one side as a side of the polygon. Convergence of the method is proven, and numerical experiments are shown to confirm the theoretical results.

**Keywords:** mixed finite element, polygonal mesh, flow in porous media

## 2.1 Introduction

Single-phase, incompressible flow in a porous medium is governed by the Darcy flow equation, a second-order elliptic equation, which when written in mixed form as a system of first order equations consists of a conservation equation together with Darcy's law. If gravity is neglected, these equations may be written as follows:

$$\nabla\cdot\,\mathbf{u} = f \quad \text{and} \quad \mathbf{u} = -\mathbf{K}\,\nabla\, p,$$

where $p$ is the fluid pressure, $\mathbf{u}$ is the Darcy flow velocity, the coefficient $\mathbf{K}$ is a symmetric, positive-definite tensor, and $f$ is a source term. It has been known since the early 1980's that mixed finite element methods are particularly well suited to solving these equations numerically. In particular, a mixed method is locally conservative, it calculates the Darcy velocity $\mathbf{u}$ simultaneously with the pressure $p$ and to the same order of accuracy, it is well adapted to handling a highly discontinuous and non diagonal permeability tensor $\mathbf{K}$. For most applications it is desirable to have the discretization of the domain into finite elements conform to the layering of the domain by the permeability coefficient $\mathbf{K}$. This is of course easily done with a grid of triangles or tetrahedra. However there are obvious advantages to using a logically rectangular grid, and for a grid of rectangles or rectangular solids, adapting to the natural layering of the domain leads to a deformation of the rectangular structure.

Several mixed finite element methods for second-order elliptic problems, both for meshes of triangles or tetrahedra and for meshes of rectangles or rectangular solids have been introduced and analyzed. The most well known of these are probably the elements defined by Raviart and Thomas (and by Nédélec in 3D) [66, 61] and the elements defined by Brezzi, Douglas and Marini (and with Fortin for rectangular solids and by Brezzi, Douglas, Duran and Fortin for tetrahedra), [24, 23, 22]. Methods have also been developed for meshes of parallelograms or parallelepipeds and for triangular prisms. See also [19] or [68] for an extensive bibliography. However straight forward extensions of these methods to handle meshes of quadrilateral polygons or hexahedra lack essential approximation properties. Several articles have addressed the problem of defining a mixed finite element on a mesh of quadrilaterals or hexahedra. Some of these, such as [72, 9, 43, 81, 5], have constructed mixed methods by enriching the polynomial approximation space, but the number of degrees of freedom can quickly become unmanageable, particularly in 3 dimensions. Others, such as [54, 55, 71], have instead kept the original degrees of freedom of the lowest order Raviart-Thomas-(Nédélec) elements, but, following an idea introduced by Kuznetsov and Repin in [54], have used composite elements. In [71], each hexahedron is divided into 5 tetrahedra, each face being divided into 2 triangles. The method has optimal convergence properties, but there is no evident way to extend the method to the case of generalized hexahedra which might have a non planar face. To overcome this problem, a composite element, in which a deformed cube is divided into 24 tetrahedra, was introduced in [18]. This element, obtained by dividing each of the 6 faces of the deformed cube into 4 triangles and considering the cones over the 24 resulting triangles emanating from an interior point of the deformed cube, has in addition the following desirable attributes: it has good symmetry properties and the division into 24 tetrahedra is uniquely defined.

The aim of the present article is to analyze the two-dimensional counterpart of the composite element of [18]. The results of [54, 55, 71] are extended for the 2D setting to the case of a composite element whose division into subcells has a vertex in the interior of the cell. This we view as a first step towards the analysis of the 3D composite element of [18].

The remainder of this article is organized as follows: Section 2.2 recalls some of the basic theory for mixed finite element methods. In Section 2.3, the composite method is defined for a mesh made up of polygons. Approximation spaces are defined locally on each polygonal cell using a triangular submesh constructed by adding an additional vertex inside the cell. With this additional point in the interior of a cell $E$, the local approximation space contains nontrivial velocity vector fields in the image of the mapping curl: $\mathbf{H}^1(E) \to \mathbf{H}(\mathrm{div}, E)$ and thus in the kernel of div: $\mathbf{H}(\mathrm{div}, E) \to L^2(E)$. Section 2.4 highlights the presence of these velocities, which must be taken into account. Section 2.5 gives some preliminary results for this extra difficulty. Optimal order convergence of the method is proven in Section 2.6, and numerical experiments corroborating this result are shown in Section 2.7.

## 2.2 Numerical analysis for mixed methods

Let $\Omega \subset \mathbb{R}^2$ be a polygonal domain that represents the porous medium. The equations that govern an incompressible Darcy flow may be written as follows:

$$\begin{aligned} \mathbf{u} &= -\mathbf{K}\,\nabla p && \text{in } \Omega, \\ \nabla\cdot\,\mathbf{u} &= f && \text{in } \Omega, \\ p &= p_{\mathrm{d}} && \text{on } \partial\Omega, \end{aligned}$$

where the unknowns are the pressure $p$ and the Darcy velocity $\mathbf{u}$. The symmetric, positive-definite tensor $\mathbf{K}$ models the diffusion of the fluid in the porous medium. The function $f\colon \Omega \to \mathbb{R}$ is a source term. For simplicity, we have assumed that the boundary conditions are only Dirichlet conditions. Let $\mathcal{M} = L^2(\Omega)$ and $\mathcal{W} = \mathbf{H}(\mathrm{div}, \Omega)$. The weak mixed formulation of the system is then

$$\begin{aligned} &\text{Find } \mathbf{u} \in \mathcal{W} \text{ and } p \in \mathcal{M} \text{ such that} \\ &a(\mathbf{u}, \mathbf{v}) + b(\mathbf{v}, p) = \mathcal{L}_{\mathcal{W}}(\mathbf{v}), \quad \forall \mathbf{v} \in \mathcal{W}, \\ &b(\mathbf{u}, q) = \mathcal{L}_{\mathcal{M}}(q), \qquad\qquad \forall q \in \mathcal{M}, \end{aligned} \tag{2.1}$$

where the bilinear forms $a\colon \mathcal{W} \times \mathcal{W} \to \mathbb{R}$ and $b\colon \mathcal{W} \times \mathcal{M} \to \mathbb{R}$ are defined by

$$a(\mathbf{u}, \mathbf{v}) = \int_\Omega \mathbf{K}^{-1}\mathbf{u} \cdot \mathbf{v}, \qquad \forall \mathbf{u} \in \mathcal{W}, \forall \mathbf{v} \in \mathcal{W}, \tag{2.2}$$

$$b(\mathbf{u}, q) = -\int_\Omega q \nabla\cdot \mathbf{u}, \qquad \forall \mathbf{u} \in \mathcal{W}, \forall q \in \mathcal{M}, \tag{2.3}$$

and the linear forms $\mathcal{L}_{\mathcal{W}}\colon \mathcal{W} \to \mathbb{R}$, and $\mathcal{L}_{\mathcal{M}}\colon \mathcal{W} \to \mathbb{R}$ by

$$\begin{aligned} \mathcal{L}_{\mathcal{W}}(\mathbf{v}) &= -\int_{\partial\Omega} p_{\mathrm{d}} \mathbf{v} \cdot \mathbf{n}, && \forall \mathbf{v} \in \mathcal{W}, \\ \mathcal{L}_{\mathcal{M}}(q) &= -\int_\Omega f q, && \forall q \in \mathcal{M}, \end{aligned}$$

where $p_{\mathrm{d}}$ is a function on the boundary of $\Omega$ determined by the Dirichlet data. In [21, Proposition 3.1], [19] and [68], it is shown that if the bilinear forms $a$ and $b$ defined respectively in (2.2) and (2.3) satisfy the following conditions:

i.) $a$ is $\mathcal{V}$-elliptic, where $\mathcal{V} = \{\mathbf{v} \in \mathcal{W} : b(\mathbf{v}, q) = 0, \forall q \in \mathcal{M}\}$; i.e.

$$\exists \alpha > 0 \text{ such that } \quad a(\mathbf{v}, \mathbf{v}) \geqslant \alpha \|\mathbf{v}\|^2_{\mathbf{H}(\mathrm{div},\Omega)}, \quad \forall \mathbf{v} \in \mathcal{V}, \tag{2.4a}$$

ii.) $b$ satisfies the following inf-sup condition:

$$\exists \beta > 0 \text{ such that } \quad \inf_{q \in \mathcal{M}} \sup_{\mathbf{v} \in \mathcal{W}} b(\mathbf{v}, q) \geqslant \beta \|\mathbf{v}\|_{\mathbf{H}(\mathrm{div},\Omega)} \|q\|_{0,\Omega}, \tag{2.4b}$$

then problem (2.1) admits a unique solution $(\mathbf{u}, p)$.

We consider now a discrete version of problem (2.1). Let $\mathcal{M}_h \subset \mathcal{M}$ denote an approximation space for the pressure and $\mathcal{W}_h \subset \mathcal{W}$ an approximation space for the velocity. The discrete problem (2.1) obtained by replacing the spaces $\mathcal{W}$ and $\mathcal{M}$ by the finite dimensional spaces $\mathcal{W}_h$ and $\mathcal{M}_h$, respectively in (2.1) is

$$\begin{aligned} &\text{Find } \mathbf{u}_h \in \mathcal{W}_h \text{ and } p_h \in \mathcal{M}_h \text{ such that} \\ &a(\mathbf{u}_h, \mathbf{v}_h) + b(\mathbf{v}_h, p_h) = \mathcal{L}_{\mathcal{W}}(\mathbf{v}_h), \quad \forall \mathbf{v}_h \in \mathcal{W}_h, \\ &b(\mathbf{u}_h, q_h) = \mathcal{L}_{\mathcal{M}}(q_h), \qquad\qquad \forall q_h \in \mathcal{M}_h. \end{aligned} \tag{2.5}$$

As for the continuous problem (2.1), if for the approximation spaces $\mathcal{M}_h$ and $\mathcal{W}_h$ the bilinear forms $a$ and $b$ defined in (2.2) and (2.3) satisfy the following conditions:

i. $a$ is $\mathcal{V}_h$-elliptic, where $\mathcal{V}_h = \{\mathbf{v}_h \in \mathcal{W}_h : b(\mathbf{v}_h, q_h) = 0, \forall q_h \in \mathcal{M}_h\}$; i.e.

$$\exists \alpha_h > 0 \text{ such that } \quad a(\mathbf{v}_h, \mathbf{v}_h) \geqslant \alpha_h \|\mathbf{v}_h\|^2_{\mathbf{H}(\mathrm{div},\Omega)}, \quad \forall \mathbf{v}_h \in \mathcal{V}_h, \tag{2.6a}$$

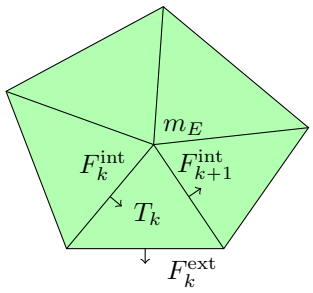


**Figure 2.1:** The mesh $\widetilde{\mathcal{T}}_E$ for a pentagon $E$ divided into 5 triangles

ii. $b$ satisfies the following discrete inf-sup condition:

$$\exists \beta_h > 0 \text{ such that, } \inf_{q_h \in \mathcal{M}_h} \sup_{\mathbf{v}_h \in \mathcal{W}_h} b(\mathbf{v}_h, q_h) \geqslant \beta_h \|\mathbf{v}_h\|_{\mathbf{H}(\text{div},\Omega)} \|q_h\|_{0,\Omega}, \tag{2.6b}$$

then the problem (2.5) admits a unique solution $(\mathbf{u}_h, p_h)$, and further there exists $C > 0$ depending only on the constants of continuity of $a$ and $b$ and the constants $\alpha_h$ and $\beta_h$ such that

$$\|p - p_h\|_{0,\Omega} + \|\mathbf{u} - \mathbf{u}_h\|_{\mathbf{H}(\text{div},\Omega)} \leqslant C \left( \inf_{q_h \in \mathcal{M}_h} \|p - q_h\|_{0,\Omega} + \inf_{\mathbf{v}_h \in \mathcal{W}_h} \|\mathbf{u} - \mathbf{v}_h\|_{\mathbf{H}(\text{div},\Omega)} \right). \tag{2.7}$$

Thus if the constants $\alpha_h$ and $\beta_h$ can be chosen independently of $h$, then $C$ will also be independent of $h$, and the problem of obtaining error estimates is then reduced to a problem of interpolation.

In the following we construct a composite mixed finite element space satisfying conditions (2.6a) and (2.6b) with constants independent of the discretization parameter $h$. Interpolation and approximation errors are shown later in Section 2.6.

## 2.3 A composite method for polygons

In this section we define the finite dimensional spaces $\mathcal{W}_h \subset \mathcal{W}$ and $\mathcal{M}_h \subset \mathcal{M}$ in which the approximations $\mathbf{u}_h$ of $\mathbf{u}$ and $p_h$ of $p$ will be sought. These are two dimensional analogues of the spaces defined in [18].

Denoting by $\mathcal{H}$ a countable set of meshsizes having 0 as its unique accumulation point, we consider mesh sequences $\{\mathcal{T}_h, h \in \mathcal{H}\}$ where for all $h \in \mathcal{H}$, $\mathcal{T}_h$ is a conforming discretization of the domain $\Omega$, made up of polygons $E$ of diameter no greater than $h$. Each polygonal cell $E \in \mathcal{T}_h$ is assumed to be star-shaped with respect to the barycenter $m_E$ of its set of vertices. To define the composite elements we make use of a refinement $\widetilde{\mathcal{T}}_h$ of $\mathcal{T}_h$ made up of triangles. If $E \in \mathcal{T}_h$ is a polygon with $n_E$ edges, then it is divided into $n_E$ triangles each of which is the cone with summit $m_E$ over one of the edges of $E$ as shown in Figure 2.1. The set of these $n_E$ triangles is denoted $\widetilde{\mathcal{T}}_E$, and $\widetilde{\mathcal{T}}_h$ is defined by

$$\widetilde{\mathcal{T}}_h = \bigcup_{E \in \mathcal{T}_h} \widetilde{\mathcal{T}}_E.$$

We let $\mathcal{F}_h$ denote the set of all edges of elements of $\mathcal{T}_h$ and $\widetilde{\mathcal{F}}_h$ the set of all edges of elements of $\widetilde{\mathcal{T}}_h$. Then $\widetilde{\mathcal{F}}_E$ will denote the set of edges of elements of $\widetilde{\mathcal{T}}_E$.

We will also use some intermediate approximation spaces associated with the mesh $\widetilde{\mathcal{T}}_h$

$$\widetilde{\mathcal{M}}_h = \{\tilde{q} \in \mathcal{M} \colon \tilde{q}|_T \text{ is constant on } T,\ \forall T \in \widetilde{\mathcal{T}}_h\}, \qquad \widetilde{\mathcal{W}}_h = \mathbf{RT}_0(\widetilde{\mathcal{T}}_h),$$

and the following spaces associated with the triangular submesh $\widetilde{\mathcal{T}}_E$:

$$\widetilde{\mathcal{M}}_E = \{\tilde{q} \in L^2(E) \colon \tilde{q}|_T \text{ is constant on } T,\ \forall T \in \widetilde{\mathcal{T}}_E\}, \qquad \widetilde{\mathcal{W}}_E = \mathbf{RT}_0(\widetilde{\mathcal{T}}_E),$$

where, for any triangular finite element mesh $\widetilde{\mathcal{T}}$, $\mathbf{RT}_0(\widetilde{\mathcal{T}})$ denotes the Raviart-Thomas space of lowest order associated with $\widetilde{\mathcal{T}}$.

The approximation space for the pressure, $\mathcal{M}_h \subset \widetilde{\mathcal{M}}_h \subset \mathcal{M}$, is defined, just as in the case of the standard Raviart-Thomas method with lowest-order elements, to be the space of functions which are constant on each polygon $E \in \mathcal{T}_h$:

$$\mathcal{M}_h = \{q \in \widetilde{\mathcal{M}}_h \subset \mathcal{M} \colon q|_E \text{ is constant on } E,\ \forall E \in \mathcal{T}_h\}.$$

We would like to define the approximation space for the velocity, $\mathcal{W}_h \subset \widetilde{\mathcal{W}}_h \subset \mathcal{W}$ such that, just as in the case of the standard Raviart-Thomas method, for each $\mathbf{v}_h \in \mathcal{W}_h$,

i) $\nabla \cdot \mathbf{v}_h$ is constant on each cell $E \in \mathcal{T}_h$; i.e. $\nabla \cdot \mathbf{v}_h \in \mathcal{M}_h$.

ii) $\mathbf{v}_h$ is defined uniquely by its (constant) normal components on the edges of the mesh $\mathcal{T}_h$.

The space $\mathcal{W}_h$ will be defined locally; i.e. for each $E \in \mathcal{T}_h$, we will define a space $\mathcal{W}_E \subset \widetilde{\mathcal{W}}_E$, and then $\mathcal{W}_h$ will be defined by

$$\mathcal{W}_h = \{\mathbf{v} \in \widetilde{\mathcal{W}}_h \subset \mathcal{W} : \mathbf{v}|_E \in \mathcal{W}_E,\ \forall E \in \mathcal{T}_h\}.$$

To define the spaces $\mathcal{W}_E$ we introduce some more notations. Let $E$ be a polygon with $n_E$ edges in $\mathcal{T}_h$. Then as noted earlier $\widetilde{\mathcal{T}}_E$ has $n_E$ triangles, $T_1, \ldots, T_{n_E}$. The set $\widetilde{\mathcal{F}}_E$ of edges of these triangles contains $2n_E$ elements, $n_E$ edges $F_1^{\text{ext}}, \ldots, F_{n_E}^{\text{ext}}$ on the boundary of $E$, and $n_E$ edges $F_1^{\text{int}}, \ldots, F_{n_E}^{\text{int}}$ in the interior of $E$. We denote the corresponding sets of edges as follows:

$$\mathcal{F}_E^{\text{ext}} = \{F \in \widetilde{\mathcal{F}}_E : F \subset \partial E\} = \widetilde{\mathcal{F}}_E \bigcap \mathcal{F}_h,$$
$$\mathcal{F}_E^{\text{int}} = \{F \in \widetilde{\mathcal{F}}_E : F \subset E^{\text{o}}\} = \widetilde{\mathcal{F}}_E \backslash \mathcal{F}_E^{\text{ext}}.$$

We suppose that these triangles and edges are numbered such that (see Figure 2.1):

- $F_1^{\text{int}} \in \mathcal{F}_E^{\text{int}}$ is an edge of $T_1$ and of $T_{n_E}$.
- $F_k^{\text{int}} \in \mathcal{F}_E^{\text{int}}$ is an edge of $T_{k-1}$ and of $T_k$, $k = 2, \ldots, n_E$.
- $F_k^{\text{ext}} \in \mathcal{F}_E^{\text{ext}}$ is an edge of $T_k$, $k = 1, \ldots, n_E$.

For each edge $F$ in $\widetilde{\mathcal{F}}_E$ we choose a unit normal vector $\mathbf{n}_F$ such that if $F \in \mathcal{F}_E^{\text{ext}}$ then $\mathbf{n}_F$ points outward from $E$, and if $F = F_k^{\text{int}} \in \mathcal{F}_E^{\text{int}}$ then $\mathbf{n}_{F_k^{\text{int}}}$ points inward toward $T_k$; again see Figure 2.1.

Clearly, if ii) is to be satisfied, the dimension of $\mathcal{W}_E$ should be equal to $n_E$, the number of edges of $E$, whereas that of $\widetilde{\mathcal{W}}_E$ is $2n_E$, the number of edges in $\widetilde{\mathcal{F}}_E$. If $\mathbf{v} \in \widetilde{\mathcal{W}}_E$, then, according to the divergence theorem, the flux through the edges of $T_k$ are related by the equations

$$v_k^{\text{int}} - v_k^{\text{int}} = d_k - v_k^{\text{ext}}, \quad k \in \mathbb{Z}_{n_E}, \tag{2.8}$$

where $v_k^{\text{int}}$ and $v_k^{\text{ext}}$, are the fluxes of $\mathbf{v}$ through $F_k^{\text{int}}$ and $F_k^{\text{ext}}$ respectively, and $d_k$ is the integral of the divergence of $\mathbf{v}$ over $T_k$, $k = 1, \ldots, n_E$. If the $n_E$ values $v_k^{\text{ext}}$ are known then the average value (over $E$) of the divergence is known (again from the divergence theorem), and if i) is satisfied, then so are the $n_E$ values $d_k$. From (2.8), we have then $n_E$ equations in $n_E$ unknowns which are the fluxes on internal edges, however they are clearly not independent: summing these $n_E$ equations we eliminate the unknowns and obtain the divergence theorem for $E$ which we have already used. Clearly if $\{v_k^{\text{int}} : k = 1, \ldots, n_E\}$ is a solution then so is $\{v_k^{\text{int}} + c : k = 1, \ldots, n_E\}$ for any constant $c$; i.e. there remains one extra dimension, in particular that generated by the nontrivial element $\boldsymbol{\varphi} \in \widetilde{\mathcal{W}}_E$ with $\operatorname{div} \boldsymbol{\varphi} = 0$ defined by

$$\varphi_k^{\text{ext}} = \int_{F_k^{\text{ext}}} \boldsymbol{\varphi} \cdot \mathbf{n}_{F_k^{\text{ext}}} = 0, \qquad \varphi_k^{\text{int}} = \int_{F_k^{\text{int}}} \boldsymbol{\varphi} \cdot \mathbf{n}_{F_k^{\text{int}}} = 1, \qquad k = 1, \ldots, n_E.$$

However any $n_E - 1$ of these equations are independent and to obtain a solution it would suffice to fix $v_k^{\text{int}}$ for any $k$, and to avoid a rotation it seems reasonable to set some $v_k^{\text{int}} = 0$. However this leaves an arbitrary choice so instead we require that the average value of the $v_k^{\text{int}}$'s be 0. So we define the space $\mathcal{W}_E$ by

$$\mathcal{W}_E = \{\mathbf{v} \in \widetilde{\mathcal{W}}_E : \operatorname{div} \mathbf{v} \text{ is constant on } E \text{ and } \phi_E(\mathbf{v}) = 0\},$$

where, for $\mathbf{v} \in \widetilde{\mathcal{W}}_E$, $\phi_E(\mathbf{v})$ is defined by

$$\phi_E(\mathbf{v}) = \frac{1}{n_E} \sum_{k=1}^{n_E} \int_{F_k^{\text{int}}} \mathbf{v} \cdot \mathbf{n}_{F_k^{\text{int}}}, \quad \forall \mathbf{v} \in \widetilde{\mathcal{W}}_E. \tag{2.9}$$

Then the local problems (2.10) which are used to compute the basis functions for $\mathcal{W}_E$ are, for all $F \in \mathcal{F}_E^{\text{ext}}$,

$$\begin{aligned} &\text{Find } \mathbf{w}_{E,F} \in \widetilde{\mathcal{W}}_E \text{ such that} \\ \nabla \cdot \mathbf{w}_{E,F} &= \frac{1}{|E|}, \\ \mathbf{w}_{E,F} \cdot \mathbf{n}_{F'} &= \frac{1}{|F|} \delta_F^{F'} \quad \forall F' \in \mathcal{F}_E^{\text{ext}}, \\ \phi_E(\mathbf{w}_{E,F}) &= 0. \end{aligned} \tag{2.10}$$

An explicit formula to compute the normal components of velocities from the conditions defined in (2.10) is given in Lemma 2.4.1. Consequently, the problem (2.10) is well-posed, and has a unique solution.

*Remark* 1. Of course we could define basis functions $\mathbf{w}_{E,F}$ and the space that they generate $\mathcal{W}_E'$ by imposing, instead of the requirement that $\phi_E(\mathbf{w}_{E,F}) = 0$, the requirement that $\mathbf{w}_{E,F}$ be a discrete gradient in the sense that it is a solution of the following problem

$$\begin{aligned} &\text{Find } \mathbf{w}_{E,F} \in \widetilde{\mathcal{W}}_E \text{ and } p_{E,F} \in \widetilde{\mathcal{M}}_E \text{ such that} \\ &\hat{a}(\mathbf{w}_{E,F}, \mathbf{v}) + b(\mathbf{v}, p_{E,F}) = 0 \qquad \forall \mathbf{v} \in \widetilde{\mathcal{W}}_E, \\ &b(\mathbf{w}_{E,F}, \tilde{q}) = -\frac{1}{|E|} \int_E \tilde{q} \qquad \forall \tilde{q} \in \widetilde{\mathcal{M}}_E, \\ &\mathbf{w}_{E,F} \cdot \mathbf{n}_{F'} = \frac{1}{|F|} \delta_F^{F'} \qquad \forall F' \in \mathcal{F}_E^{\text{ext}}, \\ &\int_E p_{E,F} = 0, \end{aligned} \tag{2.11}$$

where the bilinear form $\hat{a} : \mathcal{W} \times \mathcal{W} \to \mathbb{R}$ is defined by $\hat{a}(\mathbf{u}, \mathbf{v}) = \int_E \mathbf{u} \cdot \mathbf{v}$, for $\mathbf{u} \in \widetilde{\mathcal{W}}_E$ and $\mathbf{v} \in \widetilde{\mathcal{W}}_E$.

These definitions coincide in the case that the polygon $E$ is a regular quadrangle, coming from a linear transformation of the reference element. We compared the methods resulting from these two choices of basis functions and could not observe any significant difference in the error behavior. However the computing cost is lower when using (2.10) because unlike (2.11), the solution of this problem does not depends on the shape of the polygon.

## 2.4 An explicit expression for the flux across the interior edges of a composite element

We know that a velocity $\mathbf{v} \in \widetilde{\mathcal{W}}_E$ is uniquely defined by its normal components. An expression is given for the interior fluxes, which depends only on the divergence of $\mathbf{v}$, its normal components at the boundary, and $\phi_E(\mathbf{v})$ defined in (2.9). This expression of the normal components is used later to decompose $\mathbf{v}$ with a velocity rotating around the node $m_E$, and a remainder.

**Lemma 2.4.1.** *Let $\mathbf{v} \in \widetilde{\mathcal{W}}_E$ be arbitrary. Then for all $k = 1, \ldots, n_E$, we have*

$$v_k^{\text{int}} = \sum_{i=1}^{k-1} \frac{i}{n_E} \left(d_i - v_i^{\text{ext}}\right) - \sum_{i=k}^{n_E-1} \frac{n_E - i}{n_E} \left(d_i - v_i^{\text{ext}}\right) + \phi_E(\mathbf{v}), \tag{2.12}$$

*where $\phi_E(\mathbf{v})$ is defined in* (2.9)*, and*

$$d_i = \int_{T_i} \nabla \cdot \mathbf{v}, \qquad v_i^{\text{int}} = \int_{F_i^{\text{int}}} \mathbf{v} \cdot \mathbf{n}_{F_i^{\text{int}}}, \qquad v_i^{\text{ext}} = \int_{F_i^{\text{ext}}} \mathbf{v} \cdot \mathbf{n}_{F_i^{\text{ext}}}, \qquad \text{for } i = 1, \ldots, n_E.$$

*Proof.* Let $\mathbf{v} \in \widetilde{\mathcal{W}}_E$ and $k \in \{1, \ldots, n_E\}$. To prove (2.12), we introduce the divergence theorem in (2.8) for $\mathbf{v}$ on triangles $T_i$ for $i = 1, \ldots, n_E - 1$. Counting the definition of $\phi_E(\mathbf{v})$ in (2.9), there is $n_E$ equations, which are written in matrix form and where the definition of $\phi_E(\mathbf{v})$ is placed on the $k^{\text{th}}$ line. We obtain the linear system

$$\mathbf{M_k} \mathbf{v}^{\text{int}} = \mathbf{b_k},$$

where the components of the unknown vector $\mathbf{v}^{\text{int}}$ are its normal components to the internal edges, $v_i^{\text{int}} = \int_{F_i^{\text{int}}} \mathbf{v} \cdot \mathbf{n}_{F_i^{\text{int}}}$. The matrix is

$$\mathbf{M_k} = \begin{pmatrix} -1 & 1 & & & & & & \\ & \ddots & \ddots & & & & & \\ & & -1 & 1 & & & & \\ 1 & \cdots & 1 & 1 & 1 & \cdots & 1 & \leftarrow \text{ line } k, \\ & & & -1 & 1 & & & \\ & & & & \ddots & \ddots & & \\ & & & & & -1 & 1 & \end{pmatrix}$$

and the righthand side is

$$\begin{aligned} b_{ki} &= d_i - v_i^{\text{ext}} && \text{for } i < k, \\ b_{kk} &= n_E \phi_E(\mathbf{v}) && \text{for } i = k, \\ b_{ki} &= d_{i-1} - v_{i-1}^{\text{ext}} && \text{for } i > k. \end{aligned}$$

Moreover, we can find an expression of the normal component $v_k^{\text{int}}$ using the structure of the matrix, by summing the lines from 1 to $k-1$ to the $k^{\text{th}}$ line, and subtracting the lines from $k+1$ to $n_E$. On one hand we have

$$\sum_{i=1}^{k-1} i b_{ki} = \sum_{i=1}^{k-1} i \left(d_i - v_i^{\text{ext}}\right) = \sum_{i=1}^{k-1} i \left(v_{i+1}^{\text{int}} - v_i^{\text{int}}\right) = k v_k^{\text{int}} - \sum_{i=1}^{k} v_i^{\text{int}}.$$

and on the other hand we have

$$\begin{aligned} \sum_{i=k+1}^{n_E} (i - 1 - n_E) b_{ki} &= \sum_{i=k}^{n_E - 1} (i - n_E) \left(d_i - v_i^{\text{ext}}\right) \\ &= \sum_{i=k}^{n_E - 1} (i - n_E) \left(v_{i+1}^{\text{int}} - v_i^{\text{int}}\right) \\ &= (n_E - k) v_k^{\text{int}} - \sum_{i=k+1}^{n_E} v_i^{\text{int}}. \end{aligned}$$

Therefore,

$$b_{kk} + \sum_{i=1}^{k-1} i b_{ki} + \sum_{i=k+1}^{n_E} (i - 1 - n_E) b_{ki} = n_E \phi_E(\mathbf{v}) + n_E v_k^{\text{int}} - \sum_{i=1}^{n_E} v_i^{\text{int}}.$$

And using the definition of $\phi_E(\mathbf{v})$ in (2.9), it follows that

$$v_k^{\text{int}} = \frac{1}{n_E} \left( b_{kk} + \sum_{i=1}^{k-1} i b_{ki} + \sum_{i=k+1}^{n_E} (i - 1 - n_E) b_{ki} \right),$$

which can be rewritten as (2.12). □

**Definition 1.** According to (2.12), any velocity $\mathbf{v} \in \widetilde{\mathcal{W}}_E$ can be split into a velocity rotating around the interior point of $E$ denoted by $\mathbf{\Phi}_E(\mathbf{v}) \in \widetilde{\mathcal{W}}_E$ and a remainder $\mathbf{\Psi}_E(\mathbf{v}) \in \widetilde{\mathcal{W}}_E$:

$$\mathbf{v} = \mathbf{\Phi}_E(\mathbf{v}) + \mathbf{\Psi}_E(\mathbf{v}). \tag{2.13}$$

Both projections are defined by their normal components on interior edges $F_k^{\text{int}} \in \mathcal{F}_E^{\text{int}}$ and on edges included in the boundary of the mesh $F_k^{\text{ext}} \in \mathcal{F}_E^{\text{ext}}$. $\mathbf{\Phi}_E(\mathbf{v})$ is defined by using the definition of $\phi_E(\mathbf{v})$ in (2.9):

$$\int_{F_k^{\text{int}}} \mathbf{\Phi}_E(\mathbf{v}) \cdot \mathbf{n}_{F_k^{\text{int}}} = \phi_E(\mathbf{v}), \quad \int_{F_k^{\text{ext}}} \mathbf{\Phi}_E(\mathbf{v}) \cdot \mathbf{n}_{F_k^{\text{ext}}} = 0, \quad k = 1, \ldots, n_E,$$

and the remainder $\mathbf{\Psi}_E(\mathbf{v})$:

$$\begin{aligned}\int_{F_k^{\text{int}}} \mathbf{\Psi}_E(\mathbf{v}) \cdot \mathbf{n}_{F_k^{\text{int}}} &= \sum_{i=1}^{k-1} \frac{i}{n_E} \left( \int_{T_i} \nabla \cdot \mathbf{v} - \int_{F_i^{\text{ext}}} \mathbf{v} \cdot \mathbf{n}_{F_i^{\text{ext}}} \right) \\ &\quad - \sum_{i=k}^{n_E-1} \frac{n_E - i}{n_E} \left( \int_{T_i} \nabla \cdot \mathbf{v} - \int_{F_i^{\text{ext}}} \mathbf{v} \cdot \mathbf{n}_{F_i^{\text{ext}}} \right), \\ \int_{F_k^{\text{ext}}} \mathbf{\Psi}_E(\mathbf{v}) \cdot \mathbf{n}_{F_k^{\text{ext}}} &= \int_{F_k^{\text{ext}}} \mathbf{v} \cdot \mathbf{n}_{F_k^{\text{ext}}}, \qquad k = 1, \ldots, n_E. \end{aligned} \tag{2.14}$$

## 2.5 A bound on the velocities

From the Definition 1, we can study the behavior of a velocity $\mathbf{v} \in \widetilde{\mathcal{W}}_E$ inside the composite element. This decomposition allow us to estimate the norm of $\mathbf{v}$, from its divergence, its normal components at the boundary and $\phi_E(\mathbf{v})$.

### 2.5.1 A bound of the remainder

We need first to introduce the following norm for functions of $\widetilde{\mathcal{W}}_h$

$$[\![\mathbf{v}]\!]_T = \int_{\partial T} |\mathbf{v} \cdot \mathbf{n}|, \quad \forall T \in \widetilde{\mathcal{T}}_h, \quad \forall \mathbf{v} \in \widetilde{\mathcal{W}}_h,$$

and a shape regularity assumption to estimate the $\mathbf{L}^2$ norm of $\mathbf{v}$.

**Definition 2** (Shape regularity)**.** Let $\rho_T$ be the radius of the inscribed circle of the triangle $T$ and $h_T$ be its diameter. The shape constant of $T$ is $\sigma_T = \frac{h_T}{\rho_T}$. $\sigma_E$, the shape constant of the mesh $\widetilde{\mathcal{T}}_E$ and $\sigma_h$, that of the mesh $\mathcal{T}_h$ are

$$\sigma_E = \max_{T \in \widetilde{\mathcal{T}}_E} \sigma_T, \qquad\qquad \sigma_h = \max_{E \in \mathcal{T}_h} \sigma_E = \max_{T \in \widetilde{\mathcal{T}}_h} \sigma_T.$$

The family of meshes $\{\mathcal{T}_h, h \in \mathcal{H}\}$ is shape regular if $\sigma_h$ is uniformly bounded.

**Lemma 2.5.1** (Norm equivalence)**.** *For any velocity $\mathbf{v} \in \mathbf{RT}_0(T)$, there are constants $\alpha_T$ and $\beta_T$ such that*

$$\alpha_T \leqslant \frac{\|\mathbf{v}\|_{0,T}^2}{[\![\mathbf{v}]\!]_T^2} \leqslant \beta_T,$$

*with $\alpha_T$ and $\beta_T$ non-negative constants that depend on $T$.*

*Moreover, if the family of meshes $\{\mathcal{T}_h, h \in \mathcal{H}\}$ is shape regular, then there are constants $\alpha$ and $\beta$ independent of $T$ and $h$ such that $\forall T \in \widetilde{\mathcal{T}}_E$, $E \in \mathcal{T}_h$, $h \in \mathcal{H}$*

$$\alpha \leqslant \frac{\|\mathbf{v}\|_{0,T}^2}{[\![\mathbf{v}]\!]_T^2} \leqslant \beta. \tag{2.15}$$

*Proof.* The proof is a scaling argument. It is similar to that in [71] where $E$ was an hexahedron divided into 5 tetrahedra. □

We can now estimate the norm of $\mathbf{\Psi}_E(\mathbf{v})$ by the following theorem,

**Theorem 2.5.2.** *For any* $\mathbf{v} \in \widetilde{\mathcal{W}}_E$*, there exists a constant* $C > 0$ *independent of* $h$ *and* $\mathbf{v}$ *such that*

$$\|\mathbf{\Psi}_E(\mathbf{v})\|_{0,E}^2 \leqslant C \left( \int_E |\nabla \cdot \mathbf{v}| + \sum_{F \in \mathcal{F}_E^{\text{ext}}} \int_F |\mathbf{v} \cdot \mathbf{n}_F| \right)^2. \tag{2.16}$$

*Proof.* Let $\mathbf{v} \in \widetilde{\mathcal{W}}_E$. By using the norm equivalence (2.15), we have

$$\|\mathbf{\Psi}_E(\mathbf{v})\|_{0,E}^2 \leqslant \beta \sum_{i=1}^{n_E} \|[\mathbf{\Psi}_E(\mathbf{v})]\|_{T_i}^2 \leqslant 4\beta \left( \sum_{F \in \tilde{\mathcal{F}}_E} \int_F |\mathbf{\Psi}_E(\mathbf{v}) \cdot \mathbf{n}_F| \right)^2.$$

We deduce inequality (2.16) from the expression of normal components of $\mathbf{\Psi}_E(\mathbf{v})$ in (2.14). □

### 2.5.2 Projection operators

It remains to bound the norm of $\mathbf{\Phi}_E(\mathbf{v})$, which is possible if $\mathbf{v}$ is the projection of a velocity in $\mathbf{H}^1(E)$. We define then the projection operators onto the approximation spaces.

Let $\pi_h$ be the projection operator from $\mathcal{M} = L^2(\Omega)$ onto the approximation space $\mathcal{M}_h$ defined as

$$\pi_h(q)|_E = \pi_E(q), \qquad \pi_E(q) = \frac{1}{|E|} \int_E q, \qquad \forall E \in \mathcal{T}_h, \forall q \in \mathcal{M}.$$

Let $\mathbf{\Pi}_h$ be the projection operator from $\mathbf{H}^1(\Omega)$ onto the space $\mathcal{W}_h$ defined as

$$\mathbf{\Pi}_h(\mathbf{v})|_E = \mathbf{\Pi}_E(\mathbf{v}), \quad \mathbf{\Pi}_E(\mathbf{v}) = \sum_{F \in \mathcal{F}_E^{\text{ext}}} v_F \mathbf{w}_{E,F}, \quad v_F = \int_F \mathbf{v} \cdot \mathbf{n}_F, \quad \forall E \in \mathcal{T}_h, \forall \mathbf{v} \in \mathbf{H}^1(\Omega) \tag{2.17}$$

with $\mathbf{w}_{E,F}, F \in \mathcal{F}_E^{\text{ext}}$, the basis functions of $\mathcal{W}_E$, solutions of problems (2.10).

Similarly, the projection operators onto the approximation spaces $(\widetilde{\mathcal{M}}_h, \widetilde{\mathcal{W}}_h)$ for the **RTN** method are defined on Let $\tilde{\pi}_h$ be the projection operator from $\mathcal{M} = L^2(\Omega)$ onto $\mathcal{M}_h$ defined as

$$\tilde{\pi}_h(q)|_T = \tilde{\pi}_E(q), \qquad \tilde{\pi}_E(q) = \frac{1}{|T|} \int_T q, \qquad \forall T \in \widetilde{\mathcal{T}}_h, \forall q \in \mathcal{M}.$$

Let $\widetilde{\mathbf{\Pi}}_h$ be the projection operator from $\mathbf{H}^1(\Omega)$ onto $\widetilde{\mathcal{W}}_h$ defined as

$$\widetilde{\mathbf{\Pi}}_h(\mathbf{v})|_T = \widetilde{\mathbf{\Pi}}_T(\mathbf{v}), \quad \widetilde{\mathbf{\Pi}}_T(\mathbf{v}) = \sum_{F \in \mathcal{F}_T} v_F \mathbf{w}_{T,F}, \quad v_F = \int_F \mathbf{v} \cdot \mathbf{n}_F, \quad \forall T \in \widetilde{\mathcal{T}}_h, \forall \mathbf{v} \in \mathbf{H}^1(\Omega)$$

where the basis functions $\mathbf{w}_{T,F}$ of the $\mathbf{RT}_0$ method are associated with the edges $F \in \mathcal{F}_T$ of the triangle $T$.

We deduce some known results from the definition of the projection operators. It is

known [14, 64] that the following results hold for constants $C > 0$ independent of $h$:

$$\begin{aligned}
&\text{For } q \in L^2(E) && \|q - \pi_E(q)\|_{0,E} \leqslant C\|q\|_{0,E} && \forall E \in \mathcal{T}_h. && (2.18)\\
&\text{For } q \in L^2(T) && \|q - \widetilde{\pi}_E(q)\|_{0,T} \leqslant C\|q\|_{0,T} && \forall T \in \widetilde{\mathcal{T}}_h. && (2.19)\\
&\text{For } q \in \mathbf{H}^1(E) && \|q - \pi_E(q)\|_{0,E} \leqslant Ch\|\nabla q\|_{0,E} && \forall E \in \mathcal{T}_h. && (2.20)\\
&\text{For } q \in H^1(T) && \|q - \widetilde{\pi}_E(q)\|_{0,T} \leqslant Ch\|\nabla q\|_{0,T} && \forall T \in \widetilde{\mathcal{T}}_h.
\end{aligned}$$

For vector functions, we have the following commutative properties:

$$\begin{aligned}
&\text{For } \mathbf{v} \in \mathbf{H}^1(E) && \pi_E(\nabla\cdot \mathbf{v}) = \nabla\cdot \mathbf{\Pi}_E(\mathbf{v}), && \forall E \in \mathcal{T}_h. && (2.21)\\
&\text{For } \mathbf{v} \in \mathbf{H}^1(T) && \widetilde{\pi}_E(\nabla\cdot \mathbf{v}) = \nabla\cdot \widetilde{\mathbf{\Pi}}_T(\mathbf{v}), && \forall T \in \widetilde{\mathcal{T}}_h. && (2.22)
\end{aligned}$$

The interpolation errors for $\widetilde{\mathbf{\Pi}}_h$ are known and proven in [68, Theorem 6.3] or in [19, Proposition 2.5.1]:

$$\begin{aligned}
&\text{For } \mathbf{v} \in \mathbf{H}^1(E) && \|\mathbf{v} - \widetilde{\mathbf{\Pi}}_h(\mathbf{v})\|_{0,E} \leqslant Ch|\mathbf{v}|_{1,E}, && \forall E \in \mathcal{T}_h. && (2.23)\\
&\text{For } \mathbf{v} \in \mathbf{H}^1(E) && \|\nabla\cdot \mathbf{v} - \nabla\cdot \widetilde{\mathbf{\Pi}}_h(\mathbf{v})\|_{0,E} \leqslant Ch\|\nabla\cdot \mathbf{v}\|_{1,E}, && \forall E \in \mathcal{T}_h.
\end{aligned}$$

The interpolation errors for $\mathbf{\Pi}_h$ will be proven in Section 2.6.2.

### 2.5.3 A bound of the rotating velocity

If $\mathbf{v} \in \mathbf{H}^1(E)$, the velocity $\mathbf{\Phi}_E(\widetilde{\mathbf{\Pi}}_h(\mathbf{v}))$ can be interpreted as an interpolation error because these normal components at the boundary of $E$ are zero. Consequently, its norm can be bounded like the estimate (2.23). We recall first the Bramble-Hilbert lemma in [20, Theorem 2], which is used to bound the interpolation errors. Later we give an estimate of $\|\mathbf{\Phi}_E(\widetilde{\mathbf{\Pi}}_h(\mathbf{v}))\|_{0,E}$.

**Lemma 2.5.3** (Bramble-Hilbert)**.** *Let $E \subset \Omega$ be a Lipschitz domain. If the linear operator $\mathcal{F}\colon \mathbf{H}^1(E) \to \mathbb{R}$ meets the following conditions for any $\mathbf{v} \in \mathbf{H}^1(E)$:*

*i.* $\|\mathcal{F}(\mathbf{v})\|_{0,E} \leqslant C\|\mathbf{v}\|_{1,E}$,

*ii.* $\mathcal{F}(\mathbf{v}) = 0$ *when* $\mathbf{v}$ *is constant,*

*then there exists a constant $C > 0$ independent of $h$ and $\mathbf{v}$ such that*

$$\|\mathcal{F}(\mathbf{v})\|_{0,E} \leqslant Ch\|\mathbf{v}\|_{1,E}.$$

**Theorem 2.5.4.** *Let $\mathbf{v} \in \mathbf{H}^1(E)$. There exists a constant $C > 0$ independent of $h$ and $\mathbf{v}$ such that*

$$\|\mathbf{\Phi}_E(\widetilde{\mathbf{\Pi}}_h(\mathbf{v}))\|_{0,E} \leqslant Ch\|\mathbf{v}\|_{1,E}. \tag{2.24}$$

*Proof.* We prove the estimate of Theorem 2.5.4, by showing that on $E \in \mathcal{T}_h$, the operator $\mathcal{F} := \mathbf{\Phi}_E \circ \widetilde{\mathbf{\Pi}}_h$ satisfies the conditions of Lemma 2.5.3. For $\mathbf{v} \in \mathbf{H}^1(E)$ we have

$$\|\mathcal{F}(\mathbf{v})\|_{0,E} \leqslant \|\mathbf{v}\|_{0,E} + \|\mathbf{\Psi}_E(\widetilde{\mathbf{\Pi}}_h(\mathbf{v}))\|_{0,E} \leqslant C\|\mathbf{v}\|_{1,E},$$

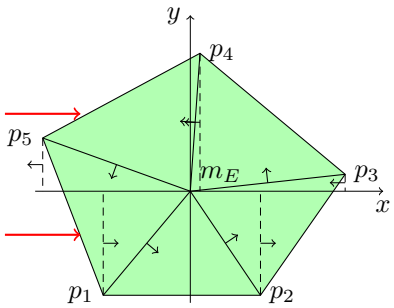


**Figure 2.2:** The mesh $\widetilde{\mathcal{T}}_E$ with a constant velocity

by using the decomposition of $\mathbf{v}$ in (2.13), the estimate (2.16) and the norm equivalence in (2.15).

Remains to prove the condition $\mathcal{F}(\mathbf{v}) = 0$ when $\mathbf{v}$ is constant. As shown in Figure 2.2, we place ourselves into the coordinate system centered on $m_E$, where the $x$ axis is oriented to follow $\mathbf{v}$. For $i = 1, \ldots, n_E$, the different vertices of $E$ are denoted $p_i = \binom{x_i}{y_i}$. We deduce that $\int_{F_i^{\text{int}}} \mathbf{v} \cdot \mathbf{n}_{F_i^{\text{int}}} = -\|\mathbf{v}\| y_i$ because $\mathbf{v}$ follows the $x$ axis and $\nabla \cdot \mathbf{v} = 0$. Consequently,

$$\phi_E(\mathbf{v}) = -\frac{\|\mathbf{v}\|}{n_E} \sum_{i=1}^{n_E} y_i = 0,$$

because $m_E$ is the barycenter of the vertices of $E$. □

## 2.6 A priori error estimation

From the previous results, we can now prove the convergence of the composite method. First, we estimate the norm of the projection $\mathbf{\Pi}_E(\mathbf{v})$, needed to have the estimate (2.7). Then we prove the convergence of the composite method.

### 2.6.1 A bound of the projection operator for the velocities

From a trace theorem [48, Theorem 1.5.1.10], there exists a constant $C > 0$ independent of $h$ such that,

$$\left| \int_F \mathbf{v} \cdot \mathbf{n}_F \right| \leqslant C \|\mathbf{v}\|_{1,E} \qquad \forall F \in \mathcal{F}_E, \forall \mathbf{v} \in \mathbf{H}^1(E), \forall E \in \mathcal{T}_h. \tag{2.25}$$

With this result, the norm of the velocities projected by $\mathbf{\Pi}_h$ can be estimated, which is necessary to prove the convergence of the method.

**Theorem 2.6.1.** *For velocities $\mathbf{v} \in \mathbf{H}^1(\Omega)$, there exists a constant $C > 0$ independent of $h$ such that*

$$\|\mathbf{\Pi}_h(\mathbf{v})\|_{\mathbf{H}(\text{div},\Omega)} \leqslant C \|\mathbf{v}\|_{1,\Omega}. \tag{2.26}$$

*Proof.* Let $\mathbf{v} \in \mathbf{H}^1(\Omega)$. The norm is studied on each element $E \in \mathcal{T}_h$. By definition of the projection operator (2.17), we have

$$\|\mathbf{\Pi}_E(\mathbf{v})\|_{0,E} \leqslant \sum_{F \in \mathcal{F}_E} \left| \int_F \mathbf{v} \cdot \mathbf{n}_F \right| \|\mathbf{w}_{E,F}\|_{0,E}.$$

For an edge $F \in \mathcal{F}_E$, the basis function $\mathbf{w}_{E,F}$ solves the problem (2.10). From it, we deduce that the norm of $\mathbf{w}_{E,F}$ can be bounded by (2.16), by using the decomposition (2.13) of velocities, and the property $\phi_E(\mathbf{w}_{E,F}) = 0$. There exists then a constant $C > 0$ such that

$$\|\mathbf{w}_{E,F}\|_{0,E}^2 \leqslant C \left( \int_E |\nabla\cdot \mathbf{w}_{E,F}| + \sum_{F' \in \mathcal{F}_E} \int_{F'} |\mathbf{w}_{E,F} \cdot \mathbf{n}_{F'}| \right)^2 .$$

Moreover, we have $\nabla\cdot \mathbf{w}_{E,F} = |E|^{-1}$ and $\mathbf{w}_{E,F} \cdot \mathbf{n}_{F'} = |F|^{-1}\delta_F^{F'}$, for an edge $F' \in \mathcal{F}_E$. Consequently,

$$\|\mathbf{\Pi}_E(\mathbf{v})\|_{0,E} \leqslant C \sum_{F \in \mathcal{F}_E} \left| \int_F \mathbf{v} \cdot \mathbf{n}_F \right|,$$

and from (2.25), we obtain $\|\mathbf{\Pi}_E(\mathbf{v})\|_{0,E} \leqslant C\|\mathbf{v}\|_{1,E}$.

Concerning the divergence of $\mathbf{\Pi}_E(\mathbf{v})$, using the commutativity property (2.21) we obtain

$$\begin{aligned} \|\nabla\cdot \mathbf{\Pi}_E(\mathbf{v})\|_{0,E} &\leqslant \|\nabla\cdot \mathbf{\Pi}_E(\mathbf{v}) - \nabla\cdot \mathbf{v}\|_{0,E} + \|\nabla\cdot \mathbf{v}\|_{0,E} \\ &\leqslant \|\pi_E(\nabla\cdot \mathbf{v}) - \nabla\cdot \mathbf{v}\|_{0,E} + \|\nabla\cdot \mathbf{v}\|_{0,E}. \end{aligned}$$

We conclude by using inequality (2.18). □

We can prove that the approximation spaces $\mathcal{M}_h$ and $\mathcal{W}_h$ satisfy the conditions (2.6a) and (2.6b), and so prove the estimate (2.7) with the previous results. The first condition (2.6a) on the bilinear form $a$ holds using (2.4a) and the fact that $\mathcal{V}_h$ is a subset of $\mathcal{V}$.

To prove (2.6b), another condition is shown from (2.4b) in [68, Theorem 13.2]. The bilinear form $b$ satisfies the inf-sup condition with respect to the spaces $\mathcal{M}_h$ and $\mathbf{H}^1(\Omega)$,

$$\exists \beta > 0, \quad \inf_{q_h \in \mathcal{M}_h} \sup_{\mathbf{v} \in \mathbf{H}^1(\Omega)} b(\mathbf{v}, q_h) \geqslant \beta \|\mathbf{v}\|_{1,\Omega} \|q_h\|_{0,\Omega}.$$

Consequently, for $q_h \in \mathcal{M}_h$, there exists a velocity $\mathbf{v} \in \mathbf{H}^1(\Omega)$ such that

$$b(\mathbf{v}, q_h) \geqslant \beta \|\mathbf{v}\|_{1,\Omega} \|q_h\|_{0,\Omega}.$$

Since $b(\mathbf{\Pi}_h(\mathbf{v}), q_h) = b(\mathbf{v}, q_h)$ and since the velocity is bounded by (2.26), we have

$$b(\mathbf{\Pi}_h(\mathbf{v}), q_h) \geqslant \beta C \|\mathbf{\Pi}_h(\mathbf{v})\|_{\mathbf{H}(\mathrm{div},\Omega)} \|q_h\|_{0,\Omega}.$$

This inequality holds for a velocity $\mathbf{v}_h = \mathbf{\Pi}_h(\mathbf{v}) \in \mathcal{W}_h$, so for the supremum, and for all functions $q_h \in \mathcal{M}_h$, which proves the estimate (2.7).

### 2.6.2 Error estimates

It remains to estimate the interpolation errors for the composite method.

**Theorem 2.6.2** (Interpolation errors)**.** *Let $\mathbf{u} \in \mathcal{W}$, $p \in \mathcal{M}$ be the solution of problem* (2.1)*. If $\mathbf{u} \in \mathbf{H}^1(\Omega)$ and $\nabla\cdot \mathbf{u} \in L^2(\Omega)$, then there exist constants $C > 0$ independent of $h$ such that*

$$\|p - \pi_h(p)\|_{0,\Omega} \leqslant Ch\|p\|_{1,\Omega}, \tag{2.27}$$

$$\|\mathbf{u} - \mathbf{\Pi}_h(\mathbf{u})\|_{0,\Omega} \leqslant Ch\|\mathbf{u}\|_{1,\Omega}, \tag{2.28}$$

$$\|\nabla\cdot(\mathbf{u} - \mathbf{\Pi}_h(\mathbf{u}))\|_{0,\Omega} \leqslant Ch\|\nabla\cdot \mathbf{u}\|_{1,\Omega}. \tag{2.29}$$

*Proof.* The estimate of the interpolation error for the scalar functions (2.27) is just inequality (2.20) extended to $\Omega$.

For the interpolation error of the vector functions (2.28) we have

$$\|\mathbf{u}-\mathbf{\Pi}_h(\mathbf{u})\|_{0,\Omega} \leqslant \|\mathbf{u}-\widetilde{\mathbf{\Pi}}_h(\mathbf{u})\|_{0,\Omega} + \|\widetilde{\mathbf{\Pi}}_h(\mathbf{u})-\mathbf{\Pi}_h(\mathbf{u})\|_{0,\Omega}.$$

Estimate (2.23) gives a bound on $\|\mathbf{u}-\widetilde{\mathbf{\Pi}}_h(\mathbf{u})\|_{0,\Omega}$. To bound $\|\widetilde{\mathbf{\Pi}}_h(\mathbf{u})-\mathbf{\Pi}_h(\mathbf{u})\|_{0,\Omega}$, we use the decomposition of velocities in (2.13) on a polygon $E \in \mathcal{T}_h$. We also remark that $\phi_E(\mathbf{\Pi}_h(\mathbf{u})) = 0$, since it is a linear combination of the basis functions, which are solutions of problems (2.10). Therefore we obtain

$$\|\widetilde{\mathbf{\Pi}}_h(\mathbf{u})-\mathbf{\Pi}_h(\mathbf{u})\|_{0,E} \leqslant \|\mathbf{\Phi}_E(\widetilde{\mathbf{\Pi}}_h(\mathbf{u}))\|_{0,E} + \|\mathbf{\Psi}_E(\widetilde{\mathbf{\Pi}}_h(\mathbf{u})-\mathbf{\Pi}_h(\mathbf{u}))\|_{0,E}.$$

Since $\mathbf{u} \in \mathbf{H}^1(E)$, the rotating velocity $\mathbf{\Phi}_E(\widetilde{\mathbf{\Pi}}_h(\mathbf{u}))$ is bounded by (2.24). The remainder is bounded by (2.16), which gives

$$\|\mathbf{\Psi}_E(\widetilde{\mathbf{\Pi}}_h(\mathbf{u})-\mathbf{\Pi}_h(\mathbf{u}))\|_{0,E} \leqslant C\left(\int_E \left|\nabla\cdot\left(\widetilde{\mathbf{\Pi}}_h(\mathbf{u})-\mathbf{\Pi}_h(\mathbf{u})\right)\right| + \sum_{F\in\mathcal{F}_E}\int_F \left|\left(\widetilde{\mathbf{\Pi}}_h(\mathbf{u})-\mathbf{\Pi}_h(\mathbf{u})\right)\cdot\mathbf{n}_F\right|\right),$$

with $C > 0$ independent of $h$ and $\mathbf{u}$. On an edge $F \in \mathcal{F}_E$ at the boundary, $\mathbf{\Pi}_h(\mathbf{u})|_F = \widetilde{\mathbf{\Pi}}_h(\mathbf{u})|_F$, so

$$\int_F \left|\left(\widetilde{\mathbf{\Pi}}_h(\mathbf{u})-\mathbf{\Pi}_h(\mathbf{u})\right)\cdot\mathbf{n}_F\right| = 0.$$

Concerning the estimate of divergence in the sum, the Cauchy-Schwarz inequality used together with the commutative properties (2.21) and (2.22), and inequalities (2.18) and (2.19) gives:

$$\begin{aligned}\int_E \left|\nabla\cdot\left(\widetilde{\mathbf{\Pi}}_h(\mathbf{u})-\mathbf{\Pi}_h(\mathbf{u})\right)\right| &\leqslant |E|^{1/2}\|\nabla\cdot\left(\widetilde{\mathbf{\Pi}}_h(\mathbf{u})-\mathbf{\Pi}_h(\mathbf{u})\right)\|_{0,E}\\ &\leqslant h\left(\|\widetilde{\pi}_h\left(\nabla\cdot\mathbf{u}\right)-\nabla\cdot\mathbf{u}\|_{0,E} + \|\nabla\cdot\mathbf{u}-\pi_h\left(\nabla\cdot\mathbf{u}\right)\|_{0,E}\right)\\ &\leqslant Ch\|\nabla\cdot\mathbf{u}\|_{0,E}\end{aligned}$$

where $C$ is a constant independent of $h$.

Finally to prove inequality (2.29), the commutativity property (2.21) together with inequality (2.20) imply

$$\|\nabla\cdot\left(\mathbf{u}-\mathbf{\Pi}_h(\mathbf{u})\right)\|_{0,E} = \|\nabla\cdot\mathbf{u}-\pi_h(\nabla\cdot\mathbf{u})\|_{0,E} \leqslant Ch\|\nabla\cdot\mathbf{u}\|_{1,E}$$

where $C$ is a constant independent of $h$. This concludes the proof of Theorem 2.6.2. □

**Theorem 2.6.3.** *Let $\mathbf{u} \in \mathcal{W}$, $p \in \mathcal{M}$ be the solution of problem (2.1), and $\mathbf{u}_h \in \mathcal{W}_h$, $p_h \in \mathcal{M}_h$ be the solution of (2.5). If $\mathbf{u} \in \mathbf{H}^1(\Omega)$, then there exists a constant $C > 0$ independent of $h$ such that*

$$\|p-p_h\|_{0,\Omega} + \|\mathbf{u}-\mathbf{u}_h\|_{\mathbf{H}(\mathrm{div},\Omega)} \leqslant Ch\left(\|p\|_{1,\Omega} + \|\mathbf{u}\|_{1,\Omega} + \|\nabla\cdot\mathbf{u}\|_{1,\Omega}\right).$$

*Proof.* The error of the convergence is proved by using the error estimate (2.7) and the interpolation errors (2.27), (2.28) and (2.29). □

## 2.7 Numerical experiments

The convergence of the composite method is shown on the domain $\Omega = [0\,;1]^2$ with meshes of quadrangles. $n$ denotes the number of discretization intervals in each direction. The exact scalar solution to compute is

$$p(x,y) = \frac{x^3}{2} + xy^2.$$

With an anisotropic tensor $\mathbf{K} = \left(\begin{smallmatrix} 2 & 1 \\ 1 & 20 \end{smallmatrix}\right)$, the expression of the exact velocity $\mathbf{u}$ is:

$$\mathbf{u}(x,y) = -\begin{pmatrix} 3x^2 + 2y^2 + 2xy \\ \frac{3}{2}x^2 + y^2 + 40xy \end{pmatrix}.$$

The first numerical experiment is performed on rectangular meshes, shown in Figure 2.3. The convergence errors and orders of convergence of the composite method are shown in Table 2.1, and compared with the errors of the $\mathbf{RT}_0$ method on the corresponding triangular submesh in Table 2.2 and one can check that the two methods converge with the same rate.

The second numerical experiment uses non rectangular meshes shown in Figure 2.4. These meshes are not built by refining a coarse mesh, so all meshes maintain the same aspect ratio for the quadrangles. Even on this kind of meshes, the method converges with an optimal rate as shown in Table 2.3, even though the errors are a little larger than that of the $\mathbf{RT}_0$ method on the triangular submeshes shown in Table 2.4.

Note that in both experiments the triangular $\mathbf{RT}_0$ method uses for velocity 3 times as many degrees of freedom as the composite method and 4 times as many for pressure.

## 2.8 Conclusion

We constructed a two-dimensional composite mixed finite element for polygonal meshes by adding an interior point to the polygonal cell which serves as a vertex as well as the polygon vertices for a triangular submesh of the polygon. We analyzed the method and showed optimal convergence. This convergence was confirmed by numerical experiments. This analysis is a first step towards the analysis of a 3-D composite mixed finite element with one interior point inside the element [18].

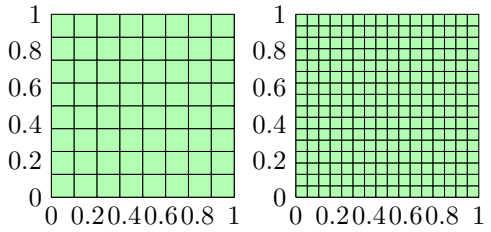


**Figure 2.3:** Rectangular meshes for $n = 8$ and $n = 16$.

| | | $\|p - p_h\|_{0,\Omega}$ | | $\|\mathbf{u} - \mathbf{u}_h\|_{0,\Omega}$ | |
|---|---|---|---|---|---|
| $n$ | $h$ | error | rate | error | rate |
| 2 | $7.07 \cdot 10^{-1}$ | $1.66 \cdot 10^{-1}$ | | $3.79 \cdot 10^{0}$ | |
| 4 | $3.54 \cdot 10^{-1}$ | $8.55 \cdot 10^{-2}$ | 0.96 | $1.91 \cdot 10^{0}$ | 0.99 |
| 8 | $1.77 \cdot 10^{-1}$ | $4.30 \cdot 10^{-2}$ | 0.99 | $9.57 \cdot 10^{-1}$ | 1.00 |
| 16 | $8.84 \cdot 10^{-2}$ | $2.15 \cdot 10^{-2}$ | 1.00 | $4.79 \cdot 10^{-1}$ | 1.00 |
| 32 | $4.42 \cdot 10^{-2}$ | $1.08 \cdot 10^{-2}$ | 1.00 | $2.39 \cdot 10^{-1}$ | 1.00 |
| 64 | $2.21 \cdot 10^{-2}$ | $5.39 \cdot 10^{-3}$ | 1.00 | $1.20 \cdot 10^{-1}$ | 1.00 |
| 128 | $1.10 \cdot 10^{-2}$ | $2.69 \cdot 10^{-3}$ | 1.00 | $5.98 \cdot 10^{-2}$ | 1.00 |
| 256 | $5.52 \cdot 10^{-3}$ | $1.35 \cdot 10^{-3}$ | 1.00 | $2.99 \cdot 10^{-2}$ | 1.00 |

**Table 2.1:** Error of the composite method on rectangular meshes.

| | | $\|p - p_h\|_{0,\Omega}$ | | $\|\mathbf{u} - \mathbf{u}_h\|_{0,\Omega}$ | |
|---|---|---|---|---|---|
| $n$ | $h$ | error | rate | error | rate |
| 2 | $5.00 \cdot 10^{-1}$ | $1.03 \cdot 10^{-1}$ | | $3.85 \cdot 10^{0}$ | |
| 4 | $2.50 \cdot 10^{-1}$ | $5.01 \cdot 10^{-2}$ | 1.03 | $1.95 \cdot 10^{0}$ | 0.98 |
| 8 | $1.25 \cdot 10^{-1}$ | $2.49 \cdot 10^{-2}$ | 1.01 | $9.77 \cdot 10^{-1}$ | 1.00 |
| 16 | $6.25 \cdot 10^{-2}$ | $1.25 \cdot 10^{-2}$ | 1.00 | $4.89 \cdot 10^{-1}$ | 1.00 |
| 32 | $3.13 \cdot 10^{-2}$ | $6.22 \cdot 10^{-3}$ | 1.00 | $2.44 \cdot 10^{-1}$ | 1.00 |
| 64 | $1.56 \cdot 10^{-2}$ | $3.11 \cdot 10^{-3}$ | 1.00 | $1.22 \cdot 10^{-1}$ | 1.00 |
| 128 | $7.81 \cdot 10^{-3}$ | $1.56 \cdot 10^{-3}$ | 1.00 | $6.11 \cdot 10^{-2}$ | 1.00 |
| 256 | $3.91 \cdot 10^{-3}$ | $7.78 \cdot 10^{-4}$ | 1.00 | $3.06 \cdot 10^{-2}$ | 1.00 |

**Table 2.2:** Error of the $\mathbf{RT}_0$ method on the triangular submeshes of the rectangular meshes.

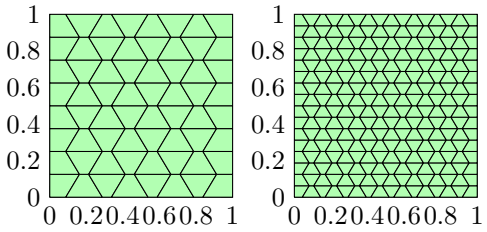


**Figure 2.4:** Non rectangular meshes with fixed aspect ratio for $n = 8$ and $n = 16$.

| | | $\|p - p_h\|_{0,\Omega}$ | | $\|\mathbf{u} - \mathbf{u}_h\|_{0,\Omega}$ | |
|---|---|---|---|---|---|
| $n$ | $h$ | error | rate | error | rate |
| 2 | $8.20 \cdot 10^{-1}$ | $1.63 \cdot 10^{-1}$ | | $5.11 \cdot 10^{0}$ | |
| 4 | $4.10 \cdot 10^{-1}$ | $9.07 \cdot 10^{-2}$ | 0.85 | $3.20 \cdot 10^{0}$ | 0.67 |
| 8 | $2.05 \cdot 10^{-1}$ | $4.65 \cdot 10^{-2}$ | 0.96 | $1.61 \cdot 10^{0}$ | 0.99 |
| 16 | $1.03 \cdot 10^{-1}$ | $2.35 \cdot 10^{-2}$ | 0.98 | $7.79 \cdot 10^{-1}$ | 1.05 |
| 32 | $5.13 \cdot 10^{-2}$ | $1.18 \cdot 10^{-2}$ | 0.99 | $3.81 \cdot 10^{-1}$ | 1.03 |
| 64 | $2.56 \cdot 10^{-2}$ | $5.91 \cdot 10^{-3}$ | 1.00 | $1.88 \cdot 10^{-1}$ | 1.02 |
| 128 | $1.28 \cdot 10^{-2}$ | $2.96 \cdot 10^{-3}$ | 1.00 | $9.34 \cdot 10^{-2}$ | 1.01 |
| 256 | $6.41 \cdot 10^{-3}$ | $1.48 \cdot 10^{-3}$ | 1.00 | $4.65 \cdot 10^{-2}$ | 1.01 |

**Table 2.3:** Error of the composite method on non rectangular meshes with fixed aspect ratio.

| | | $\|p - p_h\|_{0,\Omega}$ | | $\|\mathbf{u} - \mathbf{u}_h\|_{0,\Omega}$ | |
|---|---|---|---|---|---|
| $n$ | $h$ | error | rate | error | rate |
| 2 | $6.50 \cdot 10^{-1}$ | $1.12 \cdot 10^{-1}$ | | $4.88 \cdot 10^{0}$ | |
| 4 | $4.00 \cdot 10^{-1}$ | $6.63 \cdot 10^{-2}$ | 0.76 | $3.10 \cdot 10^{0}$ | 0.66 |
| 8 | $2.00 \cdot 10^{-1}$ | $3.30 \cdot 10^{-2}$ | 1.01 | $1.58 \cdot 10^{0}$ | 0.97 |
| 16 | $1.00 \cdot 10^{-1}$ | $1.63 \cdot 10^{-2}$ | 1.02 | $7.74 \cdot 10^{-1}$ | 1.03 |
| 32 | $5.00 \cdot 10^{-2}$ | $8.13 \cdot 10^{-3}$ | 1.00 | $3.80 \cdot 10^{-1}$ | 1.02 |
| 64 | $2.50 \cdot 10^{-2}$ | $4.08 \cdot 10^{-3}$ | 0.99 | $1.88 \cdot 10^{-1}$ | 1.01 |
| 128 | $1.25 \cdot 10^{-2}$ | $2.05 \cdot 10^{-3}$ | 1.00 | $9.36 \cdot 10^{-2}$ | 1.01 |
| 256 | $6.25 \cdot 10^{-3}$ | $1.03 \cdot 10^{-3}$ | 1.00 | $4.67 \cdot 10^{-2}$ | 1.00 |

**Table 2.4:** Error of the $\mathbf{RT}_0$ method on non rectangular meshes with fixed aspect ratio.

# Chapter 3

# Composite Methods on Irregular Hexahedral and Pyramidal Meshes

**Abstract**

We develop mixed methods for polyhedral meshes for second order elliptic problems. They are based on the construction of a tetrahedral submesh of the polyhedra. All methods have one degree of freedom per element for the pressure, and one degree of freedom per face for the velocity. Pyramidal meshes is a special case which can be treated as an extension of a work done previously. For hexahedra and prisms, a different method must be used. Meshes with curved faces are also considered. Convergence is proved for all methods and confirmed by numerical experiments. The hexahedral method is used in a realistic simulation.

**Keywords:** mixed finite elements, composite finite elements, polyhedral mesh, flow in porous media

## 3.1 Introduction

Let $\Omega \subset \mathbb{R}^3$ be a polyhedral domain. We consider the following problem governing incompressible one-phase flow in porous media

$$\begin{aligned} \mathbf{u} &= -\mathbf{K}\nabla p && \text{in } \Omega, \\ \nabla\cdot \mathbf{u} &= f && \text{in } \Omega, \\ p &= p_{\mathrm{d}} && \text{on } \partial\Omega, \end{aligned} \tag{$\mathcal{P}_0$}$$

where $p$ is the fluid pressure, $\mathbf{u}$ the Darcy flow velocity, $\mathbf{K}$ is a positive definite permeability tensor and $f$ is a source term.

We are interested in the discretization of $(\mathcal{P}_0)$ by mixed finite element methods. The velocity $\mathbf{u}$ is calculated simultaneously with the pressure $p$ with the same order of accuracy. Also in many applications, the permeability $\mathbf{K}$ is discontinuous and its magnitude varies over several orders from one geological region to another. Mixed finite element methods are particularly well suited to handle these difficulties. Moreover these methods are locally conservative and can be used both on meshes of tetrahedra and hexahedra which are

obtained from a reference element using a linear mapping. Several methods have been developed and we refer to [19] for a large bibliography.

However these methods cannot be readily extended to general polyhedral meshes since their mapping to the reference element is not linear and several methods have been proposed to overcome this difficulty [60, 63]. In [5], a solution was proposed in two dimensions but in three dimensions, the proposed methods increase the number of degrees of freedom [72, 9, 43, 81]. In this work, in order to ease the implementation into existing codes, we impose to stick to standard discretization techniques requiring one degree of freedom per cell for the pressure and one degree of freedom per face for the velocity, as in a standard cell-centered finite volume method or in the Raviart-Thomas-Nédélec mixed finite element method of lowest order, which we call the $\mathbf{RTN}_0$ method. To achieve this goal we construct in this paper a composite mixed finite element.

Composite mixed finite elements were already introduced in [54, 55, 71] and in Chapter 2. In [71] an hexahedron is divided into five tetrahedra and a face into 2 triangular subfaces. The method has optimal convergence properties for hexahedral meshes but the division into 5 tetrahedra is not unique and the element does not have good symmetry properties. Furthermore it is not possible to use the method to meshes of deformed cubes with non-planar faces.

Therefore we are drawn to the idea of dividing an hexahedron $E$ into 24 tetrahedra, by adding an interior point and dividing each of its 6 faces into 4 triangular subfaces. This division is unique and has good symmetry properties. The local approximate space must be a subset of $\mathbf{H}(\mathrm{div}, E)$ whose elements are defined piecewise as functions of $\mathbf{RTN}_0$ and must be uniquely defined by their constant divergence on $E$ and by their normal components on the boundary of $E$. However such an approximation space may have velocity vector fields turning around the internal edges, which are in the kernel of the mapping $\mathrm{div}\colon \mathbf{H}(\mathrm{div}, E) \to L^2(E)$. Therefore the basis functions of our approximation space will be defined by solving numerically a local Neumann problem on $E$ and unlike in the 2-D case in Chapter 2, we will not have an explicit formula for the basis functions.

On the other hand the method presented in Chapter 2, in two dimensions, in which a polygon is split into triangles by adding an internal node, extends readily to the case of pyramids with a quadrilateral base.

The contents of this article is as follows. Firstly Section 3.2 gives known results for the mixed finite element method. Common results used later to show the convergence of the composite methods are presented in Section 3.3. A definition of a first composite method is given in Section 3.4 together with the proof of its convergence. This method is a follow up of a 2-D polygonal method presented in [17]. Then a definition of a composite method for general polyhedral meshes is given in Section 3.5. Section 3.6 presents numerical experiments confirming the previous theoretical results. Additional test cases are studied when the mesh has curved faces. A posteriori error estimators are presented with numerical experiments in Section 3.7 and a realistic numerical experiment is shown in Section 3.8. Finally, conclusions are drawn in Section 3.9 and auxiliary results giving trace inequalities are shown in Section 3.A.

## 3.2 Mixed finite element methods

Let $\mathcal{M} = L^2(\Omega)$ and $\mathcal{W} = \mathbf{H}(\mathrm{div}, \Omega)$. The weak mixed formulation of $(\mathcal{P}_0)$ is then

$$\begin{aligned} &\text{Find } \mathbf{u} \in \mathcal{W} \text{ and } p \in \mathcal{M} \text{ such that} \\ &a(\mathbf{u}, \mathbf{v}) + b(\mathbf{v}, p) = \mathcal{L}_{\mathcal{W}}(\mathbf{v}), \quad \forall \mathbf{v} \in \mathcal{W}, \\ &b(\mathbf{u}, q) = \mathcal{L}_{\mathcal{M}}(q), \qquad\qquad \forall q \in \mathcal{M}, \end{aligned} \tag{$\mathcal{P}$}$$

where the bilinear forms $a\colon \mathcal{W} \times \mathcal{W} \to \mathbb{R}$, $b\colon \mathcal{W} \times \mathcal{M} \to \mathbb{R}$ are defined such that

$$\forall \mathbf{u} \in \mathcal{W}, \quad \forall \mathbf{v} \in \mathcal{W}, \qquad a(\mathbf{u}, \mathbf{v}) = \int_\Omega \mathbf{K}^{-1}\mathbf{u} \cdot \mathbf{v}, \tag{3.1}$$

$$\forall \mathbf{u} \in \mathcal{W}, \quad \forall q \in \mathcal{M}, \qquad b(\mathbf{u}, q) = -\int_\Omega q \nabla \cdot \mathbf{u}, \tag{3.2}$$

and the linear forms $\mathcal{L}_{\mathcal{W}}\colon \mathcal{W} \to \mathbb{R}$, $\mathcal{L}_{\mathcal{M}}\colon \mathcal{M} \to \mathbb{R}$ such that

$$\begin{aligned} &\forall \mathbf{v} \in \mathcal{W}, && \mathcal{L}_{\mathcal{W}}(\mathbf{v}) = -\int_{\partial\Omega} p_{\mathrm{d}} \mathbf{v} \cdot \mathbf{n}_\Omega, \\ &\forall q \in \mathcal{M}, && \mathcal{L}_{\mathcal{M}}(q) = -\int_\Omega f q. \end{aligned}$$

It is shown in [21, Proposition 3.1] and [68] that if $a$ and $b$ defined respectively in (3.1) and (3.2) satisfy the conditions:

i) $a$ is $\mathcal{V}$-elliptic, where $\mathcal{V} = \{\mathbf{v} \in \mathcal{W} : b(\mathbf{v}, q) = 0, \forall q \in \mathcal{M}\}$, i.e.

$$\exists \alpha > 0, \qquad a(\mathbf{v}, \mathbf{v}) \geqslant \alpha \|\mathbf{v}\|^2_{\mathbf{H}(\mathrm{div},\Omega)}, \qquad \forall \mathbf{v} \in \mathcal{V}, \tag{3.3a}$$

ii) $b$ satisfies the inf-sup condition:

$$\exists \beta > 0, \qquad \inf_{q \in \mathcal{M}} \sup_{\mathbf{v} \in \mathcal{W}} b(\mathbf{v}, q) \geqslant \beta \|\mathbf{v}\|_{\mathbf{H}(\mathrm{div},\Omega)} \|q\|_{0,\Omega}, \tag{3.3b}$$

then there exists a unique solution $(\mathbf{u}, p)$ to the problem $(\mathcal{P})$.

We give now the discrete formulation of $(\mathcal{P})$. For $h > 0$, we set $\mathcal{M}_h \subset \mathcal{M}$ as the approximation space for the pressure and $\mathcal{W}_h \subset \mathcal{W}$ the approximation space for the velocity. The discrete formulation of problem $(\mathcal{P})$ is to find $\mathbf{u}_h \in \mathcal{W}_h$ and $p_h \in \mathcal{M}_h$ such that

$$\begin{aligned} &a(\mathbf{u}_h, \mathbf{v}_h) + b(\mathbf{v}_h, p_h) = \mathcal{L}_{\mathcal{W}}(\mathbf{v}_h), \quad \forall \mathbf{v}_h \in \mathcal{W}_h, \\ &b(\mathbf{u}_h, q_h) = \mathcal{L}_{\mathcal{M}}(q_h), \qquad\qquad \forall q_h \in \mathcal{M}_h. \end{aligned} \tag{$\mathcal{P}_h$}$$

If the bilinear forms $a$ and $b$ satisfy the conditions:

i) $a$ is $\mathcal{V}_h$-elliptic, where $\mathcal{V}_h = \{\mathbf{v}_h \in \mathcal{W}_h : b(\mathbf{v}_h, q_h) = 0, \forall q_h \in \mathcal{M}_h\}$, i.e.

$$\exists \alpha_h > 0, \qquad a(\mathbf{v}_h, \mathbf{v}_h) \geqslant \alpha_h \|\mathbf{v}_h\|^2_{\mathbf{H}(\mathrm{div},\Omega)}, \qquad \forall \mathbf{v}_h \in \mathcal{V}_h. \tag{3.4a}$$

ii) $b$ satisfies the discrete inf-sup condition:

$$\exists \beta_h > 0, \qquad \inf_{q_h \in \mathcal{M}_h} \sup_{\mathbf{v}_h \in \mathcal{W}_h} b(\mathbf{v}_h, q_h) \geqslant \beta_h \|\mathbf{v}_h\|_{\mathbf{H}(\mathrm{div},\Omega)} \|q_h\|_{0,\Omega}. \tag{3.4b}$$

Then the problem $(\mathcal{P}_h)$ admits a unique solution $(\mathbf{u}_h, p_h)$, and there exists $C > 0$ depending only on the constants of continuity of $a$ and $b$, and the constants $\alpha_h$ and $\beta_h$ such that

$$\|p - p_h\|_{0,\Omega} + \|\mathbf{u} - \mathbf{u}_h\|_{\mathbf{H}(\mathrm{div},\Omega)} \leqslant C \left( \inf_{q_h \in \mathcal{M}_h} \|p - q_h\|_{0,\Omega} + \inf_{\mathbf{v}_h \in \mathcal{W}_h} \|\mathbf{u} - \mathbf{v}_h\|_{\mathbf{H}(\mathrm{div},\Omega)} \right). \tag{3.5}$$

In the following, we construct composite mixed finite elements with spaces $\mathcal{W}_h$ and $\mathcal{M}_h$ which satisfy conditions (3.4a) and (3.4b) and we will evaluate the interpolation errors.

Denoting by $\mathcal{H}$ a countable set of meshsizes having 0 as its unique accumulation point, we consider mesh sequences $\{\mathcal{T}_h, h \in \mathcal{H}\}$ where for all $h \in \mathcal{H}$, $\mathcal{T}_h$ is a conforming discretization of the domain $\Omega$, made up of pyramids, prisms and hexahedra of diameter no greater than $h$. We denote by $\mathcal{F}_h$ the set of faces of the mesh. The approximation spaces are defined such that $\mathbf{v}_h \in \mathcal{W}_h$ and $q_h \in \mathcal{M}_h$ satisfy the following conditions:

i) $q_h$ is constant on each cell $E \in \mathcal{T}_h$.

ii) $\nabla \cdot \mathbf{v}_h$ is constant on each cell $E \in \mathcal{T}_h$.

iii) $\mathbf{v}_h$ is defined uniquely by its normal components on the faces $F \in \mathcal{F}_h$.

Thus, the approximation space for pressure is

$$\mathcal{M}_h = \{q \in \mathcal{M} : q|_E \text{ is constant on } E, \ \forall E \in \mathcal{T}_h\}.$$

Concerning velocity, $\mathcal{W}_h$ is defined locally on each cell of the mesh. We will define a local finite element space $\mathcal{W}_E \subset \mathbf{H}(\mathrm{div}, E)$ for each cell $E \in \mathcal{T}_h$ and

$$\mathcal{W}_h = \{\mathbf{w} \in \mathcal{W} \colon \mathbf{w}|_E \in \mathcal{W}_E, \ \forall E \in \mathcal{T}_h\}.$$

We denote $\mathcal{F}_E = \{F \in \mathcal{F}_h, F \subset \partial E\} \subset \mathcal{F}_h$ the set of faces of $E$. To define our composite method, we construct a tetrahedral submesh $\mathcal{T}_E$ of $E$ and $\mathcal{W}_E$ will be defined as spanned by its basis functions $\mathbf{w}_{E,F} \in \mathbf{RTN}_0(\mathcal{T}_E)$ associated to faces $F \in \mathcal{F}_E$ of the cell. We introduce $\widetilde{\mathcal{F}}_E$ the set of triangular faces of $\mathcal{T}_E$ and we distinguish the internal faces $\mathcal{F}_E^{\mathrm{int}} \subset \widetilde{\mathcal{F}}_E$ from the external faces $\mathcal{F}_E^{\mathrm{ext}} \subset \widetilde{\mathcal{F}}_E$:

$$\mathcal{F}_E^{\mathrm{int}} = \{\widetilde{F} \in \widetilde{\mathcal{F}}_E, \widetilde{F} \not\subset \partial E\}, \qquad \mathcal{F}_E^{\mathrm{ext}} = \{\widetilde{F} \in \widetilde{\mathcal{F}}_E, \widetilde{F} \subset \partial E\}.$$

The normal components of the velocity though internal faces $\widetilde{F} \in \mathcal{F}_E^{\mathrm{int}}$ are obtained using the divergence theorem on the tetrahedron $T \in \mathcal{T}_E$. If we denote $\mathcal{F}_T = \{\widetilde{F} \in \widetilde{\mathcal{F}}_E, \widetilde{F} \subset \partial T\}$ the set of faces of $T$, we introduce

$$\mathcal{F}_T^{\mathrm{int}} = \{\widetilde{F} \in \mathcal{F}_T, \widetilde{F} \not\subset \partial E\}, \qquad \mathcal{F}_T^{\mathrm{ext}} = \{\widetilde{F} \in \mathcal{F}_T, \widetilde{F} \subset \partial E\}.$$

The divergence theorem applied to a velocity $\mathbf{v} \in \mathbf{RTN}_0(\mathcal{T}_E)$ gives

$$\forall T \in \mathcal{T}_E, \qquad \sum_{\widetilde{F} \in \mathcal{F}_T^{\mathrm{int}}} \int_{\widetilde{F}} \mathbf{v} \cdot \mathbf{n}_T = \int_T \nabla \cdot \mathbf{v} - \sum_{\widetilde{F} \in \mathcal{F}_T^{\mathrm{ext}}} \int_{\widetilde{F}} \mathbf{v} \cdot \mathbf{n}_T, \tag{3.6}$$

where $\mathbf{n}_T$ is the outward normal on $\partial T$.

However if the submesh $\mathcal{T}_E$ contains an internal edge which is the case with the methods that we consider in this paper, then the system (3.6) does not have a unique solution. Let $\mathcal{E}_E^{\text{int}}$ be the set of internal edges of $E$. As shown in Chapter 2 in two dimensions, we can define a velocity $\boldsymbol{\varphi}_e \in \mathbf{RTN}_0(\mathcal{T}_E)$ turning around the internal edge $e \in \mathcal{E}_E^{\text{int}}$ which is in the kernel of the matrix of system (3.6). For this, we define the set of faces $\mathcal{F}_e \subset \mathcal{F}_E^{\text{int}}$ which have $e$ included in their boundaries:

$$\mathcal{F}_e = \{\widetilde{F} \in \mathcal{F}_E^{\text{int}}, e \subset \partial\widetilde{F}\}.$$

Moreover for each face $\widetilde{F} \in \mathcal{F}_e$, we associate a normal $\mathbf{n}_{\widetilde{F}}^e$ in order that the set of these normals is oriented to turn around $e$. Thus the velocity $\boldsymbol{\varphi}_e$ is defined such that

$$\forall \widetilde{F} \in \mathcal{F}_e, \quad \int_{\widetilde{F}} \boldsymbol{\varphi}_e \cdot \mathbf{n}_{\widetilde{F}}^e = 1, \qquad \forall \widetilde{F} \in \widetilde{\mathcal{F}}_E \backslash \mathcal{F}_e, \quad \int_{\widetilde{F}} \boldsymbol{\varphi}_e \cdot \mathbf{n}_{\widetilde{F}} = 0.$$

Consequently we have $\nabla \cdot \boldsymbol{\varphi}_e = 0$, $\int_{\widetilde{F}} \boldsymbol{\varphi}_e \cdot \mathbf{n}_{\widetilde{F}} = 0$ for all faces $\widetilde{F} \in \mathcal{F}_E^{\text{ext}}$ and system (3.6) does not have a unique solution.

In order to define uniquely a velocity $\mathbf{v} \in \mathbf{RTN}_0(\mathcal{T}_E)$ from its divergence and its normal components at the boundary, we introduce for $e \in \mathcal{E}_E^{\text{int}}$ the function $\phi_e$ as

$$\phi_e(\mathbf{v}) = \frac{1}{n_e} \sum_{\widetilde{F} \in \mathcal{F}_e} \int_{\widetilde{F}} \mathbf{v} \cdot \mathbf{n}_{\widetilde{F}}^e, \qquad \forall \mathbf{v} \in \mathbf{RTN}_0(\mathcal{T}_E), \tag{3.7}$$

where $n_e$ is the cardinal of $\mathcal{F}_e$ i.e. the number of faces which have $e$ included in their boundary. Adding equation (3.7) to the system (3.6), we obtain an expression of the flux of $\mathbf{v}$ across all internal faces in terms of the divergence of $\mathbf{v}$, the flux of $\mathbf{v}$ across the faces included in $\partial E$ and of the $\phi_e(\mathbf{v})$'s.

**Lemma 3.2.1.** *Let $E \in \mathcal{T}_h$ be a polyhedron and $\widetilde{F} \in \mathcal{F}_E^{\text{int}}$ be a triangular face of the mesh $\mathcal{T}_E$ located inside $E$. There exists sets of coefficient $\{\alpha_{\widetilde{F}'}, \widetilde{F}' \in \mathcal{F}_E^{\text{ext}}\}$, $\{\beta_T, T \in \mathcal{T}_E\}$ and $\{\gamma_e, e \in \mathcal{E}_E^{\text{int}}\}$ depending only on $\widetilde{F}$ such that for any velocity $\mathbf{v} \in \mathbf{RTN}_0(\mathcal{T}_E)$:*

$$\int_{\widetilde{F}} \mathbf{v} \cdot \mathbf{n}_{\widetilde{F}} = \sum_{\widetilde{F}' \in \mathcal{F}_E^{\text{ext}}} \alpha_{\widetilde{F}'} \int_{\widetilde{F}} \mathbf{v} \cdot \mathbf{n}_{\widetilde{F}'} + \sum_{T \in \mathcal{T}_E} \beta_T \int_T \nabla \cdot \mathbf{v} + \sum_{e \in \mathcal{E}_E^{\text{int}}} \gamma_e \phi_e(\mathbf{v}) \tag{3.8}$$

This will be proved in (3.8) Lemma 3.4.1 for pyramids and Lemma 3.5.1 for any polyhedra. Also in Lemma 3.4.1, an explicit formula of the coefficients is given for the case of pyramids.

For a pyramid $E$, the tetrahedral submesh can be built with only one internal edge $e$ connecting the apex of $E$ to the barycenter of the vertices of its base. Basis functions for $\mathcal{W}_E$ are defined as defined by their normal components on the faces of $E$ and by setting $\phi_e(\mathbf{w}_{E,F}) = 0$ for all $F \in \mathcal{F}_E$. Following ideas from the two dimensional analysis in Chapter 2, we show in Section 3.4 that this is sufficient to construct $\mathcal{W}_E$ and $\mathcal{W}_h$ satisfying the inf sup condition and optimal convergence properties.

However this method can not be extended to hexahedra and prisms. Therefore we consider a second composite mixed finite element method that call polyhedral method, which applies to meshes of a combination of pyramids, prisms and hexahedra. To construct the tetrahedral submesh $\mathcal{T}_E$, we proceed as before for pyramids but for prisms and hexahedra, we add an internal vertex inside $E$ and quadrangular faces are divided into four triangular

subfaces by adding a vertex at the barycenter of the vertices of the face, as we have done for the pyramid bases. Setting $\phi_e(\mathbf{w}_{E,F}) = 0$, the resulting approximation spaces $\mathcal{W}_E$ and $\mathcal{W}_h$ do not have optimal approximation properties. Consequently, in Section 3.5, velocity basis functions are instead computed by solving a Neumann problem on the tetrahedral mesh with a vanishing average pressure.

## 3.3 Convergence of composite mixed finite elements

We now outline the main steps for obtaining convergence results. We introduce the projection operators $\pi_h \colon \mathcal{M} \to \mathcal{M}_h$ onto the scalar approximation space:

$$\forall q \in \mathcal{M}, \qquad \pi_h(q)|_E = \pi_E(q), \qquad \pi_E(q) = \frac{1}{|E|}\int_E q, \qquad \forall E \in \mathcal{T}_h.$$

Interpolation errors of scalar functions are bounded by the Poincaré inequalities given in [14, 64]. There exists constant $C_{\mathrm{p}} > 0$ independent of $h$ such that

$$\forall q \in H^1(E), \qquad \|q - \pi_E(q)\|_{0,E} \leqslant C_{\mathrm{p}} h \|\nabla q\|_{0,E} \qquad \forall E \in \mathcal{T}_h. \tag{3.9}$$

(3.9) gives the interpolation error for the pressure in the righthand side of (3.5).

Concerning velocities, we introduce the projection operator $\mathbf{\Pi}_h \colon \mathbf{H}^1(\Omega) \to \mathcal{W}_h$ defined as

$$\forall \mathbf{v} \in \mathbf{H}^1(\Omega), \quad \mathbf{\Pi}_h(\mathbf{v})|_E = \mathbf{\Pi}_E(\mathbf{v}), \quad \mathbf{\Pi}_E(\mathbf{v}) = \sum_{F \in \mathcal{F}_E} \int_F \mathbf{v}\cdot\mathbf{n}_E \, \mathbf{w}_{E,F}, \quad \forall E \in \mathcal{T}_h, \tag{3.10}$$

where $\mathbf{n}_E$ is the outward normal on $\partial E$. For a polyhedron $E \in \mathcal{T}_h$ and a velocity $\mathbf{v} \in \mathbf{H}^1(E)$, we have

$$\int_E \nabla\cdot\mathbf{\Pi}_E(\mathbf{v}) = \int_{\partial E} \mathbf{\Pi}_E(\mathbf{v})\cdot\mathbf{n}_E = \int_{\partial E} \mathbf{v}\cdot\mathbf{n}_E = \int_E \nabla\cdot\mathbf{v},$$

which implies the commutative property

$$\forall \mathbf{v} \in \mathbf{H}^1(E), \quad \nabla\cdot\mathbf{\Pi}_E(\mathbf{v}) = \pi_E(\nabla\cdot\mathbf{v}). \tag{3.11}$$

The interpolation error for the velocity will be obtained by applying the following lemma given in [20, Theorem 2].

**Lemma 3.3.1** (Bramble-Hilbert)**.** *Let $E \subset \Omega$ be a Lipschitz domain. If the linear operator $\mathbf{\Pi}_E \colon \mathbf{H}^1(E) \to \mathcal{W}_E$ satisfy the following conditions for every $\mathbf{v} \in \mathbf{H}^1(E)$:*

*i)* $\|\mathbf{v} - \mathbf{\Pi}_E(\mathbf{v})\|_{0,E} \leqslant C\|\mathbf{v}\|_{1,E}$,

*ii)* $\|\mathbf{v} - \mathbf{\Pi}_E(\mathbf{v})\|_{0,E} = 0$ *when* $\mathbf{v}$ *is constant,*

*then there exists a constant $C > 0$ independent of $h$ and $\mathbf{v}$ such that*

$$\|\mathbf{v} - \mathbf{\Pi}_E(\mathbf{v})\|_{0,E} \leqslant Ch\|\mathbf{v}\|_{1,E}. \tag{3.12}$$

We show condition *i*) of the Bramble-Hilbert lemma by bounding the norm of the

projection operator. By definition we have that

$$\forall \mathbf{v} \in \mathbf{H}^1(E), \qquad \|\mathbf{\Pi}_E(\mathbf{v})\|_{0,E} \leqslant \sum_{F \in \mathcal{F}_E} \int_F |\mathbf{v} \cdot \mathbf{n}_F| \ \|\mathbf{w}_{E,F}\|_{0,E}. \tag{3.13}$$

The $\mathbf{L}^2$ norm of basis functions must be estimated according to their normal components. For this purpose, we introduce the norm of normal components defined in [17] and [71],

$$[\![\mathbf{v}]\!]_T = \int_{\partial T} |\mathbf{v} \cdot \mathbf{n}_T| \,, \qquad \forall \mathbf{v} \in \mathbf{RTN}_0(T), \quad \forall T \in \mathcal{T}_E. \tag{3.14}$$

Its link to the velocity $\mathbf{L}^2$ norm is given below, assuming that the mesh used is shape regular. The assumption of shape regularity needs to be applied on the tetrahedral submesh of the elements because the composite method is built by using functions of the $\mathbf{RTN}_0$ method on this submesh.

**Definition 3** (Shape regularity)**.** Let $h \in \mathcal{H}$ and $\mathcal{T}_E$ a tetrahedral mesh of a polyhedron $E \in \mathcal{T}_h$. For a tetrahedron $T \in \mathcal{T}_E$, we denote $h_T$ its diameter and $\rho_T$ the radius of the inscribed sphere of $T$. The shape constant of $T$ is $\sigma_T = \frac{h_T}{\rho_T}$. Thus we define the shape constant $\sigma_E = \max_{T \in \mathcal{T}_E} \sigma_T$ of a polyhedron $E$ as the supremum of the shape constants $\sigma_T$ for $T \in \mathcal{T}_E$. Similarly, the shape constant of the mesh $\sigma_h = \max_{E \in \mathcal{T}_h} \sigma_E$ is the supremum of the shape constants $\sigma_E$ for $E \in \mathcal{T}_h$. Therefore, the family of meshes $\{\mathcal{T}_h, h \in \mathcal{H}\}$ is said to be shape regular if the shape constants for the meshes $\sigma_h$ are uniformly bounded.

Assuming that the mesh is shape regular, we can estimate the norm of normal components given in (3.14) according to the velocity $\mathbf{L}^2$ norm.

**Lemma 3.3.2** (Norm equivalence)**.** *Let $T$ be a tetrahedron. For any velocity $\mathbf{v} \in \mathbf{RTN}_0(T)$, there are non-negative constants $\alpha_T$ and $\beta_T$ such that*

$$\alpha_T \leqslant \frac{\|\mathbf{v}\|_{0,T}^2}{[\![\mathbf{v}]\!]_T^2} \leqslant \beta_T.$$

*Moreover, if the family of meshes $\{\mathcal{T}_h, h \in \mathcal{H}\}$ is shape regular, then there are non-negative constants $\alpha$ and $\beta$ independent of $T$ and $h$ such that for any $h \in \mathcal{H}$, $E \in \mathcal{T}_h$ and $T \in \mathcal{T}_E$,*

$$\alpha \leqslant \frac{|T|}{h^2} \frac{\|\mathbf{v}\|_{0,T}^2}{[\![\mathbf{v}]\!]_T^2} \leqslant \beta. \tag{3.15}$$

*Proof.* The proof is a scaling argument. It is similar to that in [71] where $E$ is an hexahedron divided into 5 tetrahedra. □

Following norm equivalence given in previous Lemma 3.3.2, we can bound the $\mathbf{L}^2$ norm of a velocity according to its normal components. From Lemma 3.2.1 giving the expression of normal components of a velocity on internal faces, we deduce the following estimate:

**Lemma 3.3.3.** *Let $E \in \mathcal{T}_h$ be a polyhedron and $\mathbf{v} \in \mathbf{RTN}_0(\mathcal{T}_E)$ be arbitrary. Then there exists a constant $C > 0$ independent of $\mathbf{v}$ and $h$ such that*

$$\|\mathbf{v}\|_{0,E}^2 \leqslant C \frac{h^2}{|E|} \left( \int_{\partial E} |\mathbf{v} \cdot \mathbf{n}_E| + \int_E |\nabla \cdot \mathbf{v}| + \sum_{e \in \mathcal{E}_E^{\text{int}}} |\phi_e(\mathbf{v})| \right)^2. \tag{3.16}$$

*Proof.* Inequality (3.16) is obtained by using both the norm equivalence (3.15) and the expression of the normal components on internal faces (3.8). □

Now that we can bound the norm of basis functions, it remains to estimate the normal components of a velocity $\mathbf{v} \in \mathbf{H}^1(E)$. An estimate similar to the norm equivalence is obtained by using the trace inequality [37, Lemma 1.49].

**Lemma 3.3.4.** *Let $E \in \mathcal{T}_h$ be a polyhedron and $F \in \mathcal{F}_E \bigcup \mathcal{F}_E^{\text{ext}}$ be a face of $E$ or a triangular subface included in the boundary of $E$. For $q \in H^1(E)$ be arbitrary, we have*

$$\|q\|_{0,F}^2 \leqslant C \left( \|\nabla q\|_{0,E} + h^{-1} \|q\|_{0,E} \right) \|q\|_{0,E}. \tag{3.17}$$

With inequality (3.16), we can show condition *i*) of the Bramble-Hilbert lemma which is done below depending on the definition of basis functions, in Theorem 3.4.2 if the cell is a pyramid and in Theorem 3.5.2 for any polyhedron. Condition *ii*) of the Bramble-Hilbert lemma is shown thereafter.

Thus from error estimate (3.5), if the constants $\alpha_h$ and $\beta_h$ can be chosen independently of $h$, then $C$ will also be independent of $h$ and the problem of obtaining error estimates is then reduced to a problem of interpolation. The first condition (3.4a) on the bilinear form $a$ holds using (3.3a) and the fact that $\mathcal{V}_h$ is a subset of $\mathcal{V}$. To show the second condition (3.4b), we apply condition (3.3b) to the space $\mathbf{H}^1(\Omega) \subset \mathbf{H}(\text{div}, \Omega)$ as in [68, Theorem 13.2],

$$\exists \beta > 0, \qquad \inf_{q_h \in \mathcal{M}_h} \sup_{\mathbf{v} \in \mathbf{H}^1(\Omega)} b(\mathbf{v}, q_h) \geqslant \beta \|\mathbf{v}\|_{1,\Omega} \|q_h\|_{0,\Omega}.$$

Consequently, for any function $q_h \in \mathcal{M}_h$, there exists a velocity $\mathbf{v} \in \mathbf{H}^1(\Omega)$ such that

$$b(\mathbf{v}, q_h) \geqslant \beta \|\mathbf{v}\|_{1,\Omega} \|q_h\|_{0,\Omega}. \tag{3.18}$$

Below in Theorem 3.3.5, we show that the norm of a velocity is greater than the norm of its projection, which allows us to show condition (3.4b) from (3.18) and to show estimate (3.5).

**Theorem 3.3.5.** *Let $E \in \mathcal{T}_h$ be a polyhedron and $\mathbf{v} \in \mathbf{H}^1(E)$ be arbitrary. There exists a constant $C > 0$ independent of $h$ such that*

$$\|\mathbf{\Pi}_E(\mathbf{v})\|_{\mathbf{H}(\text{div},E)} \leqslant C \|\mathbf{v}\|_{1,E}.$$

*Proof.* The $\mathbf{L}^2$ norm of the projection operator is bounded below in Theorem 3.4.2 for a pyramid and in Theorem 3.5.2 for any polyhedra. The norm of the divergence is bounded by using the commutative property in (3.11) together with the Cauchy-Schwarz inequality. □

## 3.4 A composite mixed finite element method for pyramids

We consider here the particular case of a pyramidal mesh.

### 3.4.1 Definition of the method

If $E$ is a pyramid, the submesh $\mathcal{T}_E$ can be built by dividing the pyramid into 4 tetrahedra by adding one node at the barycenter of the vertices of its base.

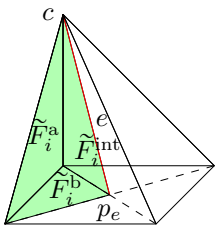


**Figure 3.1:** The mesh $\mathcal{T}_E$ for a pyramid $E$, divided into 4 tetrahedra

As shown in Figure 3.1, the submesh contains only one internal edge joining this node to the apex. The set of internal edges $\mathcal{E}_E^{\mathrm{int}}$ is reduces to a singleton which is common to all internal faces of the submesh and for $e \in \mathcal{E}_E^{\mathrm{int}}$, we have $\mathcal{F}_e = \mathcal{F}_E^{\mathrm{int}}$. Since the tetrahedral mesh contains 4 triangular faces, system (3.6) resulting from the divergence theorem on each tetrahedra is square but not invertible. Replacing one of the equations of system (3.6) by the definition of $\phi_e(\mathbf{v})$ in (3.7), we obtain a invertible system presented below in Lemma 3.4.1.

To obtain an explicit formula of normal components, it is necessary to number tetrahedra and faces of the submesh. For $i = 1, \ldots, n_e$, the tetrahedron $T_i$ is surrounded by the faces $\widetilde{F}_i^{\mathrm{int}} \in \mathcal{F}_E^{\mathrm{int}}$ and $\widetilde{F}_{k+1}^{\mathrm{int}} \in \mathcal{F}_E^{\mathrm{int}}$, the face $\widetilde{F}_i^{\mathrm{b}} \in \mathcal{F}_E^{\mathrm{ext}}$ located at the base of the pyramid and the face $\widetilde{F}_i^{\mathrm{a}} \in \mathcal{F}_E^{\mathrm{ext}}$, as shown in Figure 3.1.

**Lemma 3.4.1.** *Let $E \in \mathcal{T}_h$ be a pyramid, such that the tetrahedral submesh $\mathcal{T}_E$ of $E$ is build with only one internal edge denoted $e$. For any velocity $\mathbf{v} \in \mathbf{RTN}_0(\mathcal{T}_E)$ and a tetrahedron $T_0 \in \mathcal{T}_E$ chosen arbitrary, the following system whose unknowns are the normal components of $\mathbf{v}$ on internal faces,*

$$\begin{aligned} \forall T \in \mathcal{T}_E \backslash \{T_0\}, \qquad \sum_{\widetilde{F} \in \mathcal{F}_T^{\mathrm{int}}} \int_{\widetilde{F}} \mathbf{v} \cdot \mathbf{n}_T = \int_T \nabla \cdot \mathbf{v} - \sum_{\widetilde{F} \in \mathcal{F}_T^{\mathrm{ext}}} \int_{\widetilde{F}} \mathbf{v} \cdot \mathbf{n}_T, \\ \frac{1}{n_e} \sum_{\widetilde{F} \in \mathcal{F}_e} \int_{\widetilde{F}} \mathbf{v} \cdot \mathbf{n}_{\widetilde{F}}^e = \phi_e(\mathbf{v}), \end{aligned} \tag{3.19}$$

*has a unique solution. Moreover for $k = 1, \ldots, n_e$, we have*

$$\begin{aligned} \int_{\widetilde{F}_k^{\mathrm{int}}} \mathbf{v} \cdot \mathbf{n}_{\widetilde{F}_k^{\mathrm{int}}} = \sum_{i=1}^{k-1} \frac{i}{n_E} \left( \int_{T_i} \nabla \cdot \mathbf{v} - \int_{\widetilde{F}_i^{\mathrm{b}}} \mathbf{v} \cdot \mathbf{n}_{\widetilde{F}_i^{\mathrm{b}}} - \int_{\widetilde{F}_i^{\mathrm{a}}} \mathbf{v} \cdot \mathbf{n}_{\widetilde{F}_i^{\mathrm{a}}} \right) \\ - \sum_{i=k}^{n_E - 1} \frac{n_E - i}{n_E} \left( \int_{T_i} \nabla \cdot \mathbf{v} - \int_{\widetilde{F}_i^{\mathrm{b}}} \mathbf{v} \cdot \mathbf{n}_{\widetilde{F}_i^{\mathrm{b}}} - \int_{\widetilde{F}_i^{\mathrm{a}}} \mathbf{v} \cdot \mathbf{n}_{\widetilde{F}_i^{\mathrm{a}}} \right) + \phi_e(\mathbf{v}). \end{aligned}$$

*Proof.* The proof is similar to that of [17, Lemma 4.1] in two dimensions. □

*Remark* 2. Coefficient of system (3.19) does not depends on $h$ or on the shape of $E$, but only on the topology of the submesh $\mathcal{T}_E$. A similar system is given in Lemma 3.5.1 for a polyhedron whose submesh $\mathcal{T}_E$ is built with an added node inside $E$.

From Lemma 3.4.1, normal components of a velocity are determined uniquely by its divergence, its normal components on faces of $E$, and the average value of its normal components on internal faces. Thus for $E \in \mathcal{T}_h$ and $F \in \mathcal{F}_E$, we define the basis functions

$\mathbf{w}_{E,F} \in \mathbf{RTN}_0(\mathcal{T}_E)$ of $\mathcal{W}_E$ by

$$\begin{aligned} \nabla\cdot \mathbf{w}_{E,F} &= \frac{1}{|E|}, \\ \forall \widetilde{F} \in \mathcal{F}_E^{\text{ext}}, \quad \mathbf{w}_{E,F}\cdot \mathbf{n}_{\widetilde{F}} &= \begin{cases} \dfrac{1}{|F|} & \text{if } \widetilde{F} \subset F, \\ 0 & \text{otherwise,} \end{cases} \\ \forall e \in \mathcal{E}_E^{\text{int}}, \qquad \phi_e(\mathbf{w}_{E,F}) &= 0. \end{aligned} \tag{3.20}$$

### 3.4.2 Interpolation errors for pyramidal mixed finite elements

We now show that condition *i*) and *ii*) in the Bramble-Hilbert Lemma 3.3.1 are satisfied so that the velocity satisfies interpolation errors (3.12). Condition *i*) is a direct consequence of the following theorem:

**Theorem 3.4.2.** *Let $E \in \mathcal{T}_h$ be a pyramid. If the projection operator $\mathbf{\Pi}_E$ is defined as in* (3.10) *with basis functions given in* (3.20)*, then there exist a constant $C > 0$ independent of $h$ such that*

$$\forall \mathbf{v} \in \mathbf{H}^1(E), \qquad \|\mathbf{\Pi}_E(\mathbf{v})\|_{0,E} \leqslant C\|\mathbf{v}\|_{1,E}.$$

*Proof.* Let $E \in \mathcal{T}_h$ be a pyramid and $\mathbf{v} \in \mathbf{H}^1(E)$. Applying inequality (3.16) to the basis functions of $\mathcal{W}_E$, we have

$$\forall F \in \mathcal{F}_E, \qquad \|\mathbf{w}_{E,F}\|_{0,E}^2 \leqslant C\frac{h^2}{|E|}\left(\int_{\partial E}|\mathbf{w}_{E,F}\cdot\mathbf{n}_E| + \int_E |\nabla\cdot\mathbf{w}_{E,F}| + |\phi_e(\mathbf{w}_{E,F})|\right)^2,$$

where $e$ is the internal edge. From the definition (3.20) of basis functions, we have $\int_{\partial E}|\mathbf{w}_{E,F}\cdot\mathbf{n}_E| = 1$, $\int_E |\nabla\cdot\mathbf{w}_{E,F}| = 1$ and $\phi_e(\mathbf{w}_{E,F}) = 0$. Using inequality (3.13), we obtain

$$\|\mathbf{\Pi}_E(\mathbf{v})\|_{0,E} \leqslant C\sum_{F\in\mathcal{F}_E}\frac{h}{|E|^{1/2}}\int_F |\mathbf{v}\cdot\mathbf{n}_F|.$$

Using the Cauchy-Schwarz inequality, we can apply estimate (3.17) since $\mathbf{v}\cdot\mathbf{n}_F \in H^1(\Omega)$. The assumption of shape regularity concludes the proof. □

It remains to show condition *ii*). We have to show that the approximation space $\mathcal{W}_E$ contains the constant velocities. For this purpose, we remark that if $\mathbf{v} \in \mathbf{H}^1(E)$ is a constant velocity, then $\mathbf{v} \in \mathbf{RTN}_0(\mathcal{T}_E)$. Consequently, it remains to show that the normal components of $\mathbf{v}$ and $\mathbf{\Pi}_E(\mathbf{v})$ are equals. Moreover, the decomposition of velocities given by solving (3.19) applies for both on $\mathbf{v}$ and $\mathbf{\Pi}_E(\mathbf{v})$. Thus we have to show that $\mathbf{v}$ and $\mathbf{\Pi}_E(\mathbf{v})$ have the same normal components at the boundary of $E$, that they have the same divergence and that $\phi_e(\mathbf{v}) = \phi_e(\mathbf{\Pi}_E(\mathbf{v}))$ for the internal edge $e \in \mathcal{E}_E^{\text{int}}$. We have by definition of $\mathbf{\Pi}_E$

$$\forall F \in \mathcal{F}_E, \quad \int_F \mathbf{\Pi}_E(\mathbf{v})\cdot\mathbf{n}_F = \int_F \mathbf{v}\cdot\mathbf{n}_F, \qquad \nabla\cdot\mathbf{\Pi}_E(\mathbf{v}) = \nabla\cdot\mathbf{v}, \qquad \phi_e(\mathbf{\Pi}_E(\mathbf{v})) = 0.$$

It remains to prove that $\phi_e(\mathbf{v}) = 0$ for a constant velocity $\mathbf{v}$ so we have $\phi_e(\mathbf{v}) = \phi_e(\mathbf{\Pi}_E(\mathbf{v}))$ and $\mathbf{v} = \mathbf{\Pi}_E(\mathbf{v})$.

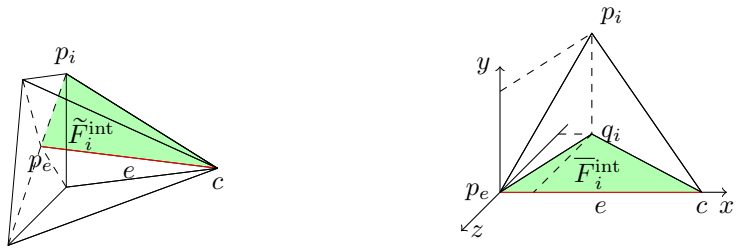


**(a)** Numbering of the nodes of $\mathcal{T}_E$ **(b)** Coordinate system centered on $p_e$

**Figure 3.2:** Coordinate system on a pyramid-shape element

**Lemma 3.4.3.** *Let $E \in \mathcal{T}_h$ be a pyramid such that $\mathcal{T}_E$ is built with only one internal edge denoted $e$ connecting the barycenter of the vertices of the pyramid basis to its apex. If $\mathbf{v} \in \mathbf{H}^1(E)$ is a constant velocity, then*

$$\phi_e(\mathbf{v}) = 0 \tag{3.21}$$

*with $\phi_e(\mathbf{v})$ defined in* (3.7)

*Proof.* Let $E \in \mathcal{T}_h$ be a pyramid and $\mathbf{v} \in \mathbf{H}^1(E)$ be a constant velocity. As shown in Figure 3.2a, the submesh $\mathcal{T}_E$ has only one internal edge denoted $e$. The base of the pyramid have $n_e$ vertices which is equal to the number of faces around $e$. We number these nodes $p_i$ similarly as internal faces $\widetilde{F}_i^{\text{int}} \in \mathcal{F}_E^{\text{int}}$, such that $p_i$ is the node of $\widetilde{F}_i^{\text{int}}$ located at the base of the pyramid, for $i = 1, \ldots, n_e$. The apex of the pyramid is denoted by $c$ and the barycenter of the vertices of the pyramid base $p_e$. We place ourselves in the coordinate system centered on $p_e$ such that the $x$ axis follows the edge $e$. Then we have

$$c = \begin{pmatrix} x_c \\ 0 \\ 0 \end{pmatrix}, \qquad p_i = \begin{pmatrix} x_i \\ y_i \\ z_i \end{pmatrix}, \text{ for } i = 1, \ldots, n_e.$$

Moreover $\mathbf{v}$ is split into three components in this coordinate system:

$$\mathbf{v} = \mathbf{v}_x + \mathbf{v}_y + \mathbf{v}_z.$$

We have $\phi_e(\mathbf{v}_x) = 0$ because $\mathbf{v}_x$ is orthogonal to the normals of the internal faces. To evaluate $\phi_e(\mathbf{v}_y)$, we define $q_i$ as the projection of $p_i$ on the plane $y = 0$, as shown in Figure 3.2b. We denote by $\overline{F}_i^{\text{int}}$ the face whose vertices are $p_e$, $c$ and $q_i$. By using the divergence theorem on the tetrahedron with $p_e$, $c$, $q_i$ and $p_i$, we obtain that the components of $\mathbf{v}$ normal to on faces $\widetilde{F}_i^{\text{int}}$ and $\overline{F}_i^{\text{int}}$ are equal because $\nabla \cdot \mathbf{v} = 0$. Then we have $\int_{\widetilde{F}_i^{\text{int}}} \mathbf{v}_y \cdot \mathbf{n}^e_{\widetilde{F}_i^{\text{int}}} = -\|\mathbf{v}_y\| \frac{x_c z_i}{2}$. and consequently

$$\phi_e(\mathbf{v}_y) = \frac{1}{n_e} \sum_{i=1}^{n_e} \int_{\widetilde{F}_i} \mathbf{v}_y \cdot \mathbf{n}^e_{\widetilde{F}_i} = \frac{-\|\mathbf{v}_y\| x_c}{2n_e} \sum_{i=1}^{n_e} z_i = 0,$$

since $p_e$ which is the center of the coordinate system, is the barycenter of vertices $p_i$, for $i = 1, \ldots, n_e$. Similarly for $\mathbf{v}_z$, we define the projection on the plan $z = 0$ to obtain $\phi_e(\mathbf{v}_z) = 0$, which concludes the proof. □

Thus we have shown that the velocity approximation space contains the constant

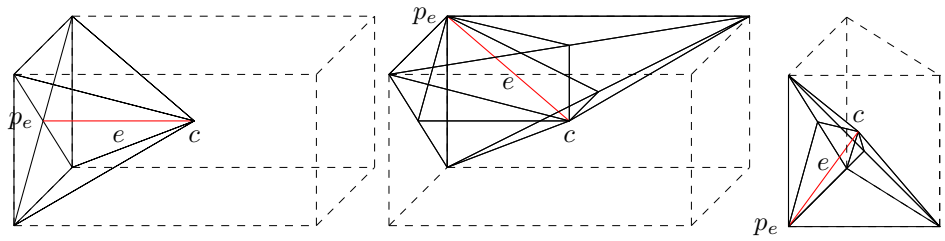


**(a)** Internal edge joining the barycenter of the vertices of a face

**(b)** Internal edge joining the vertex of an hexahedron

**(c)** Internal edge joining the vertex of a prism

**Figure 3.3:** Examples of internal edges joining the barycenter of the vertices

velocities, the velocity approximation space satisfies both conditions of the Bramble-Hilbert lemma so estimate (3.12) holds. Since approximation spaces satisfy conditions (3.4a) and (3.4b), we can now state the following convergence estimate.

**Theorem 3.4.4.** *Let $p \in \mathcal{M}$, $\mathbf{u} \in \mathcal{W}$ be the solution of problem $(\mathcal{P})$. Let $\mathcal{T}_h$ be a mesh made of pyramids, and $p_h \in \mathcal{M}_h$, $\mathbf{u}_h \in \mathcal{W}_h$ be the solution of problem $(\mathcal{P}_h)$. If the family of meshes $\{\mathcal{T}_h, h \in \mathcal{H}\}$ is shape regular, then there exists a constant $C > 0$ independent of $\mathbf{u}$, $p$ and $h$ such that*

$$\|p - p_h\|^2_{0,\Omega} + \|\mathbf{u} - \mathbf{u}_h\|^2_{\mathbf{H}(\mathrm{div},\Omega)} \leqslant Ch^2 \left( \|p\|^2_{1,\Omega} + \|\mathbf{u}\|^2_{1,\Omega} + \|\nabla \cdot \mathbf{u}\|^2_{1,\Omega} \right), \tag{3.22}$$

*assuming that $p$ and $\mathbf{u}$ are enough regular to define the righthand side.*

*Proof.* The convergence error (3.22) is shown by using the estimate given in (3.5) by the inf sup condition with the projection errors shown in (3.9) for the pressure and the divergence, and the projection error in (3.12) given by the Bramble-Hilbert lemma for the velocity. □

*Remark* 3. Theorem 3.4.4 is valid only for pyramids. If we take the basis functions defined previously in (3.20), then the constant velocities may not be inside the approximation space $\mathcal{W}_h$ for any polyhedron. Indeed for an hexahedron $E \in \mathcal{T}_h$, the submesh $\mathcal{T}_E$ is built by adding an internal node at the barycenter. Equality (3.21) is true for edges joining the internal node to the nodes added on the faces (Figure 3.3a) but not for the edges joining the internal node to a vertex of $E$ (Figure 3.3a). We notice however that if $E$ is the reference cube and if $\mathbf{v} \in \mathbf{H}^1(E)$ is constant, then $\phi_e(\mathbf{v}) = 0$ for every edges $e \in \mathcal{E}_E^{\mathrm{int}}$. Therefore Theorem 3.4.4 holds for meshes made of hexahedra coming from a linear mapping of the reference element.

On the other hand if $E$ is the reference prism and $e \in \mathcal{E}_E^{\mathrm{int}}$ the edge joining the barycenter to the origin, as shown in Figure 3.3c, then we have that $\phi_e(\mathbf{v}_x) \neq 0$ for the constant velocity $\mathbf{v}_x$ which follows the $x$ axis. Consequently, velocity approximation space generated by basis functions in (3.20) is not suitable for prisms coming from a linear mapping of the reference element.

## 3.5 A composite mixed finite element method for polyhedra

We present in this section the composite method extended for any polyhedra. The definition of basis functions is different from that of the pyramidal composite method because the tetrahedral submesh is built by adding an internal node.

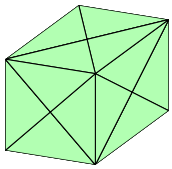

**Figure 3.4:** The mesh $\mathcal{T}_E$ for a cube $E$, divided into 24 tetrahedra

### 3.5.1 Definition of the composite mixed finite elements for polyhedra

If we assume that the mesh $\mathcal{T}_h$ is made only of hexahedra, the tetrahedral submesh $\mathcal{T}_E$ of $E \in \mathcal{T}_h$ is built as following: The faces of the hexahedron are split into four triangular subfaces by adding a node at the barycenter of the vertices. Next we add a node at the barycenter of the vertices of the element and by joining each nodes to this one. The obtained submesh is shown in Figure 3.4. So, every tetrahedra $T \in \mathcal{T}_E$ has three faces located in the interior of $E$ and one face included at the boundary of $E$.

Similarly as the pyramidal composite method, the velocity approximation space $\mathcal{W}_h$ is defined by the local space $\mathcal{W}_E$. The local space is spanned by the basis functions $\mathbf{w}_{E,F} \in \mathbf{H}(\mathrm{div}, E)$ of the method which are associated to the faces $F \in \mathcal{F}_E$ of the hexahedron. If we denote $\widetilde{\mathcal{M}}_E \subset L^2(E)$ and $\widetilde{\mathcal{W}}_E \subset \mathbf{H}(\mathrm{div}, E)$ the spaces associated to the $\mathbf{RTN}_0$ method on the tetrahedral submesh:

$$\widetilde{\mathcal{M}}_E = \{\widetilde{q} \in L^2(E) \colon \widetilde{q}|_T \text{ is constant on } T,\ \forall T \in \mathcal{T}_E\}, \qquad \widetilde{\mathcal{W}}_E = \mathbf{RTN}_0(\mathcal{T}_E),$$

and if we denote $\mathcal{F}_E^{\mathrm{ext}}$ as the set of triangular subfaces located at the boundary of $E$, then $\mathbf{w}_{E,F} \in \widetilde{\mathcal{W}}_E$ is defined as the solution of the following mixed problem:

$$\begin{aligned}
&\text{Find } \mathbf{w}_{E,F} \in \widetilde{\mathcal{W}}_E \text{ and } p_{E,F} \in \widetilde{\mathcal{M}}_E \text{ such that} \\
&\int_E \mathbf{w}_{E,F} \cdot \mathbf{v} - \int_E p_{E,F}\, \nabla\cdot \mathbf{v} = 0 \qquad \forall \mathbf{v} \in \widetilde{\mathcal{W}}_E, \\
&\int_E \widetilde{q}\, \nabla\cdot \mathbf{w}_{E,F} = \frac{1}{|E|} \int_E \widetilde{q} \qquad \forall \widetilde{q} \in \widetilde{\mathcal{M}}_E, \\
&\mathbf{w}_{E,F} \cdot \mathbf{n}_{\widetilde{F}} = \begin{cases} \dfrac{1}{|F|} & \text{if } \widetilde{F} \subset F, \\ 0 & \text{otherwise,} \end{cases} \qquad \forall \widetilde{F} \in \mathcal{F}_E^{\mathrm{ext}}, \\
&\int_E p_{E,F} = 0.
\end{aligned} \tag{3.23}$$

The problem (3.23) has a unique solution, since it is the discrete formulation of the Laplacian with Neumann boundary conditions.

In order to prove the convergence of the composite method for polyhedra, we have to bound the normal components of a velocity on internal faces, as performed for pyramids in Lemma 3.4.1. Equations of divergence theorems are completed by the average value of normal components on faces located around internal edges until that obtaining an invertible system.

**Lemma 3.5.1.** *Let $E \in \mathcal{T}_h$ be a polyhedron such that $\mathcal{T}_E$ is built by adding a node inside the element. Given a velocity $\mathbf{v} \in \widetilde{\mathcal{W}}_E$, a tetrahedron $T_0 \in \mathcal{T}_E$ and an internal edge $e_0 \in \mathcal{E}_E^{\mathrm{int}}$,*

*the following system is invertible:*

$$\begin{aligned} &\forall T \in \mathcal{T}_E \backslash \{T_0\}, \qquad \sum_{\widetilde{F} \in \mathcal{F}_T^{\text{int}}} \int_{\widetilde{F}} \mathbf{v} \cdot \mathbf{n}_T = \int_T \nabla \cdot \mathbf{v} - \sum_{\widetilde{F} \in \mathcal{F}_T^{\text{ext}}} \int_{\widetilde{F}} \mathbf{v} \cdot \mathbf{n}_T. \\ &\forall e \in \mathcal{E}_E^{\text{int}} \backslash \{e_0\}, \quad \frac{1}{n_e} \sum_{\widetilde{F} \in \mathcal{F}_e} \int_{\widetilde{F}} \mathbf{v} \cdot \mathbf{n}_{\widetilde{F}}^e = \phi_e(\mathbf{v}). \end{aligned} \tag{3.24}$$

*Proof.* Let $\mathbf{v} \in \widetilde{\mathcal{W}}_E$, $T_0 \in \mathcal{T}_E$ and $e_0 \in \mathcal{E}_E^{\text{int}}$. We introduce the divergence theorem for $\mathbf{v}$ on tetrahedra of the mesh:

$$\forall T \in \mathcal{T}_E \backslash \{T_0\} \qquad \sum_{\widetilde{F} \in \mathcal{F}_T^{\text{int}}} \int_{\widetilde{F}} \mathbf{v} \cdot \mathbf{n}_T = \int_T \nabla \cdot \mathbf{v} - \sum_{\widetilde{F} \in \mathcal{F}_T^{\text{ext}}} \int_{\widetilde{F}} \mathbf{v} \cdot \mathbf{n}_T.$$

If we denote $\#\mathcal{T}_E$ the number of tetrahedra of the mesh $\mathcal{T}_E$, the above equation gives $\#\mathcal{T}_E - 1$ linearly independent equations. Written in a matrix form, the kernel of this system contains the velocities turning around the internal edges of $\mathcal{T}_E$, because their divergence and their normal components at the boundary are zero. As in Lemma 3.4.1, the previous equations are completed with the definition of $\phi_e(\mathbf{v})$ given in (3.7), for edges $e \in \mathcal{E}_E^{\text{int}} \backslash \{e_0\}$ to obtain the system (3.24).

If $\#\mathcal{F}_E^{\text{int}}$ and $\#\mathcal{E}_E^{\text{int}}$ are respectively the number of internal faces $\mathcal{T}_E$ and the number of internal edges of the tetrahedral submesh $\mathcal{T}_E$, the system (3.24) has $\#\mathcal{F}_E^{\text{int}}$ unknowns for $\#\mathcal{T}_E + \#\mathcal{E}_E^{\text{int}} - 2$ equations. From the incomplete basis theorem, the system is invertible if it is square. We have from the Euler polyhedron formula in [67] that

$$\#\mathcal{V}_E - \#\mathcal{E}_E + \#\mathcal{F}_E = 2,$$

where $\#\mathcal{V}_E$ is the number of vertices of $E$, $\#\mathcal{E}_E$ is the number of edges of $E$ and $\#\mathcal{F}_E$ is the number of faces of $E$. By construction of the tetrahedral submesh, we have

$$\#\mathcal{F}_E^{\text{int}} = \#\mathcal{T}_E + \#\mathcal{E}_E = \#\mathcal{T}_E + \#\mathcal{V}_E + \#\mathcal{F}_E - 2 = \#\mathcal{T}_E + \#\mathcal{E}_E^{\text{int}} - 2.$$

Then the system (3.24) is square and invertible. □

**Definition 4.** From the expression of normal components given in Lemma 3.5.1 for polyhedra or that previously given Lemma 3.4.1 for pyramids, any velocity $\mathbf{v} \in \widetilde{\mathcal{W}}_E$ can be split into a part turning around the internal edges of $\mathcal{T}_E$ denoted by $\mathbf{\Phi}_E(\mathbf{v}) \in \widetilde{\mathcal{W}}_E$ and a remainder $\mathbf{\Psi}_E(\mathbf{v}) \in \widetilde{\mathcal{W}}_E$ such that

$$\mathbf{v} = \mathbf{\Phi}_E(\mathbf{v}) + \mathbf{\Psi}_E(\mathbf{v}),$$

and defined as:

$$\begin{aligned} &\forall T \in \mathcal{T}_E, && \int_T \nabla \cdot \mathbf{\Phi}_E(\mathbf{v}) = 0, && \int_T \nabla \cdot \mathbf{\Psi}_E(\mathbf{v}) = \int_T \nabla \cdot \mathbf{v}. \\ &\forall \widetilde{F} \in \mathcal{F}_E^{\text{ext}}, && \int_{\widetilde{F}} \mathbf{\Phi}_E(\mathbf{v}) \cdot \mathbf{n}_{\widetilde{F}} = 0, && \int_{\widetilde{F}} \mathbf{\Psi}_E(\mathbf{v}) \cdot \mathbf{n}_{\widetilde{F}} = \int_{\widetilde{F}} \mathbf{v} \cdot \mathbf{n}_{\widetilde{F}}. \\ &\forall e \in \mathcal{E}_E^{\text{int}}, && \phi_e(\mathbf{\Phi}_E(\mathbf{v})) = \phi_e(\mathbf{v}), && \phi_e(\mathbf{\Psi}_E(\mathbf{v})) = 0. \end{aligned}$$

### 3.5.2 Projection errors of the composite mixed finite elements for polyhedra

To show the convergence of the composite method, we have to show the conditions *i*) and *ii*) of the Bramble-Hilbert lemma.

**Theorem 3.5.2.** *Let $E \in \mathcal{T}_h$ be a polyhedron such that $\mathcal{T}_E$ is built with an added internal node. If the projection operator $\mathbf{\Pi}_E$ is defined by the basis functions given in* (3.23)*, then there exist a constant $C > 0$ independent of $h$ such that*

$$\forall \mathbf{v} \in \mathbf{H}^1(E), \qquad \|\mathbf{\Pi}_E(\mathbf{v})\|_{0,E} \leqslant C\|\mathbf{v}\|_{1,E}.$$

*Proof.* Let $E \in \mathcal{T}_h$ and $\mathbf{v} \in \mathbf{H}^1(E)$. By definition of the velocity projection operator in (3.10), we have that

$$\|\mathbf{\Pi}_E(\mathbf{v})\|_{0,E} \leqslant \sum_{F \in \mathcal{F}_E} \int_F |\mathbf{v} \cdot \mathbf{n}_E| \ \|\mathbf{w}_{E,F}\|_{0,E}.$$

As in the proof of Theorem 3.4.2, we have to bound the norm of basis function. Given a face $F \in \mathcal{F}_E$, the velocity $\mathbf{w}_{E,F}$ solves the Neumann problem (3.23). Choosing the test function $\mathbf{\Phi}_E(\mathbf{w}_{E,F}) \in \widetilde{\mathcal{W}}_E$ in the first equation, we obtain that

$$\int_E \mathbf{w}_{E,F} \cdot \mathbf{\Phi}_E(\mathbf{w}_{E,F}) = 0.$$

Then from the decomposition of velocities in the Definition 4 and the Cauchy-Schwarz inequality, we deduce that

$$\|\mathbf{\Phi}_E(\mathbf{w}_{E,F})\|_{0,E} \leqslant \|\mathbf{\Psi}_E(\mathbf{w}_{E,F})\|_{0,E}.$$

Moreover we have by definition that $\phi_e(\mathbf{\Psi}_E(\mathbf{w}_{E,F})) = 0$ on every internal edges $e \in \mathcal{E}_E^{\text{int}}$. Thus we obtain from the norm estimate (3.16) that

$$\|\mathbf{w}_{E,F}\|_{0,E} \leqslant C\frac{h}{|E|^{1/2}} \left( \int_{\partial E} |\mathbf{w}_{E,F} \cdot \mathbf{n}_E| + \int_E |\nabla \cdot \mathbf{w}_{E,F}| \right),$$

where $C > 0$ is a constant independent of $h$ and $\mathbf{w}_{E,F}$. By definition of basis functions, we have $\int_{\partial E} |\mathbf{w}_{E,F} \cdot \mathbf{n}_E| = 1$ and $\int_E |\nabla \cdot \mathbf{w}_{E,F}| = 1$, which gives us

$$\|\mathbf{\Pi}_E(\mathbf{v})\|_{0,E} \leqslant C \sum_{F \in \mathcal{F}_E} \frac{h}{|E|^{1/2}} \int_F |\mathbf{v} \cdot \mathbf{n}_F| \,.$$

Finally, the estimate $\|\mathbf{\Pi}_E(\mathbf{v})\|_{0,E} \leqslant C\|\mathbf{v}\|_{1,E}$ is obtained due to the bound of normal components in (3.17) since $\mathbf{v} \cdot \mathbf{n}_F \in H^1(E)$, and the shape regularity assumption. □

It remains to show that the approximation space of the composite method contains the constant velocities. As previously stated the constant velocities may not be in the kernel of the function $\phi_e$ associated to edges $e \in \mathcal{E}_E^{\text{int}}$. However solving the discrete problem (3.23) ensures that the velocity approximation space contains the constant velocities.

Let $\widetilde{\mathbf{u}} \in \mathbf{H}^1(E)$ be a constant velocity. The projection $\mathbf{\Pi}_E(\widetilde{\mathbf{u}}) \in \mathcal{W}_E$ is defined by a linear combination of the basis functions which are solution of (3.23). We deduce from it

that there exists a discrete pressure $\widetilde{p} \in \widetilde{\mathcal{M}}_E$ such that the pair $\mathbf{\Pi}_E(\widetilde{\mathbf{u}})$, $\widetilde{p}$ is the solution to the Neumann problem:

$$\begin{aligned}
&\int_E \mathbf{\Pi}_E(\widetilde{\mathbf{u}}) \cdot \mathbf{v} - \int_E \widetilde{p} \nabla \cdot \mathbf{v} = 0, && \forall \mathbf{v} \in \widetilde{\mathcal{W}}_E, \\
&\int_E \widetilde{q} \nabla \cdot \mathbf{\Pi}_E(\widetilde{\mathbf{u}}) = 0 && \forall \widetilde{q} \in \widetilde{\mathcal{M}}_E, \\
&\mathbf{\Pi}_E(\widetilde{\mathbf{u}}) \cdot \mathbf{n}_{\widetilde{F}} = \widetilde{\mathbf{u}} \cdot \mathbf{n}_{\widetilde{F}}, && \forall \widetilde{F} \in \mathcal{F}_E^{\text{ext}}, \\
&\int_E \widetilde{p} = 0.
\end{aligned}$$

Moreover, we remark that the constant velocity $\widetilde{\mathbf{u}}$, which is the exact solution of a Laplacian, is a solution of the above problem. From the uniqueness of the solution, we have that $\mathbf{\Pi}_E(\widetilde{\mathbf{u}}) = \widetilde{\mathbf{u}}$.

Therefore we can apply the Bramble-Hilbert Lemma 3.3.1 for the velocity projection operator defined from basis functions in (3.23). Thus we have the convergence estimate.

**Theorem 3.5.3.** *Let $p \in \mathcal{M}$, $\mathbf{u} \in \mathcal{W}$ be the solution of problem $(\mathcal{P})$. Let $\mathcal{T}_h$ be a polyhedral mesh, and $p_h \in \mathcal{M}_h$, $\mathbf{u}_h \in \mathcal{W}_h$ the solution of problem $(\mathcal{P}_h)$. If the family of meshes $\{\mathcal{T}_h, h \in \mathcal{H}\}$ is shape regular, then there exists a constant $C > 0$ independent of $\mathbf{u}$, $p$ and $h$ such that*

$$\|p - p_h\|_{0,\Omega}^2 + \|\mathbf{u} - \mathbf{u}_h\|_{\mathbf{H}(\text{div},\Omega)}^2 \leqslant Ch^2 \left( \|p\|_{1,\Omega}^2 + \|\mathbf{u}\|_{1,\Omega}^2 + \|\nabla \cdot \mathbf{u}\|_{1,\Omega}^2 \right), \tag{3.25}$$

*assuming that $p$ and $\mathbf{u}$ are enough regular to define the righthand side.*

*Proof.* The convergence error (3.25) is shown by using the error estimates of projection operators (3.9) and (3.12) with the bound (3.5). □

## 3.6 Numerical experiments for convergence

We present numerical convergence results for both composite methods on the unity cube $\Omega = [0\,;1]^3$, on hexahedral and pyramidal meshes. The pyramidal mesh is built from the hexahedral mesh, by splitting the hexahedra into 6 pyramids. Hence the pyramidal mesh have the same properties as the hexahedral mesh. The chosen exact solution $p$ is

$$p(x, y, z) = 2xz + \frac{y^2}{2} + z,$$

and the tensor $\mathbf{K}$ is

$$\mathbf{K} = \begin{pmatrix} 3 & 1 & \frac{1}{2} \\ 1 & 2 & 0 \\ \frac{1}{2} & 0 & 1 \end{pmatrix}.$$

Then the expression of the exact velocity $\mathbf{u}$ is

$$\mathbf{u}(x, y, z) = -\begin{pmatrix} x + y + 6z + 1/2 \\ 2y + 2z \\ 2x + z + 1 \end{pmatrix}.$$

Dirichlet boundary conditions are set at the boundary of $\Omega$.

We recall that the pyramidal composite method uses for the velocity basis functions the solution of the problem (3.20). Due to Lemma 3.5.1, one can easily see that it can actually be readily extended to an hexahedral mesh by stating the condition $\phi_e(\mathbf{w}_{E,F}) = 0$ for

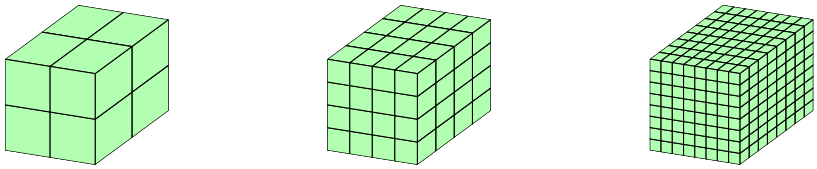

**Figure 3.5:** Regular meshes with respectively 8, 64 and 512 hexahedra.

| | | Method 1 | | | | Method 2 | | | |
|---|---|---|---|---|---|---|---|---|---|
| | | $\|p-p_h\|_{0,\Omega}$ | | $\|\mathbf{u}-\mathbf{u}_h\|_{0,\Omega}$ | | $\|p-p_h\|_{0,\Omega}$ | | $\|\mathbf{u}-\mathbf{u}_h\|_{0,\Omega}$ | |
| $n$ | $h$ | error | rate | error | rate | error | rate | error | rate |
| 2 | $8.66\cdot10^{-1}$ | $3.51\cdot10^{-1}$ | | $9.72\cdot10^{-1}$ | | $3.51\cdot10^{-1}$ | | $9.72\cdot10^{-1}$ | |
| 4 | $4.33\cdot10^{-1}$ | $1.76\cdot10^{-1}$ | 0.99 | $4.86\cdot10^{-1}$ | 1.00 | $1.76\cdot10^{-1}$ | 0.99 | $4.86\cdot10^{-1}$ | 1.00 |
| 8 | $2.17\cdot10^{-1}$ | $8.83\cdot10^{-2}$ | 1.00 | $2.43\cdot10^{-1}$ | 1.00 | $8.83\cdot10^{-2}$ | 1.00 | $2.43\cdot10^{-1}$ | 1.00 |
| 16 | $1.08\cdot10^{-1}$ | $4.42\cdot10^{-2}$ | 1.00 | $1.21\cdot10^{-1}$ | 1.00 | $4.42\cdot10^{-2}$ | 1.00 | $1.21\cdot10^{-1}$ | 1.00 |

**Table 3.1:** Convergence errors on regular hexahedral meshes in Figure 3.5

| | | Method 1 | | | | Method 2 | | | |
|---|---|---|---|---|---|---|---|---|---|
| | | $\|p-p_h\|_{0,\Omega}$ | | $\|\mathbf{u}-\mathbf{u}_h\|_{0,\Omega}$ | | $\|p-p_h\|_{0,\Omega}$ | | $\|\mathbf{u}-\mathbf{u}_h\|_{0,\Omega}$ | |
| $n$ | $h$ | error | rate | error | rate | error | rate | error | rate |
| 2 | $7.07\cdot10^{-1}$ | $2.34\cdot10^{-1}$ | | $9.71\cdot10^{-1}$ | | $2.34\cdot10^{-1}$ | | $9.71\cdot10^{-1}$ | |
| 4 | $3.54\cdot10^{-1}$ | $1.17\cdot10^{-1}$ | 1.00 | $4.84\cdot10^{-1}$ | 1.00 | $1.17\cdot10^{-1}$ | 1.00 | $4.84\cdot10^{-1}$ | 1.00 |
| 8 | $1.77\cdot10^{-1}$ | $5.85\cdot10^{-2}$ | 1.00 | $2.42\cdot10^{-1}$ | 1.00 | $5.85\cdot10^{-2}$ | 1.00 | $2.42\cdot10^{-1}$ | 1.00 |
| 16 | $8.84\cdot10^{-2}$ | $2.92\cdot10^{-2}$ | 1.00 | $1.21\cdot10^{-1}$ | 1.00 | $2.92\cdot10^{-2}$ | 1.00 | $1.21\cdot10^{-1}$ | 1.00 |

**Table 3.2:** Convergence errors on regular pyramidal meshes obtained from hexahedral meshes shown in Figure 3.5

the 14 interior edges $e \in \mathcal{E}_E^{\text{int}}$ of the tetrahedral submesh. In the following, we will refer to the pyramidal composite method and its extension to hexahedral meshes as Method 1. Similarly the hexahedral composite method uses for the velocity basis functions the solution of the problem (3.23), but it can actually be implemented also for pyramids by replacing the tetrahedral submesh of 24 tetrahedra for an hexahedron by a tetrahedral submesh of 4 tetrahedra for a pyramid. We will refer to the hexahedral composite method applied to both hexahedral and pyramidal meshes as Method 2.

In all numerical experiments we will compare results on hexahedral meshes shown in Figure 3.5, 3.6, 3.8, 3.9 and those obtained on a pyramidal mesh in which each hexahedron is divided into 6 pyramids whose bases are the 6 faces of the hexahedron.

### 3.6.1 Numerical experiments with meshes having planar faces

The first numerical experiment is performed on regular meshes, as shown in Figure 3.5. The convergence errors are presented in Table 3.1 for hexahedral meshes and in Table 3.2 for pyramidal meshes. $n$ describes the number of hexahedra in one direction, and $h$ is the step of the mesh. We observe that both methods converge with the same accuracy. For both methods, the pressure errors are a little bit smaller for the pyramidal mesh than for the hexahedral mesh, because the number of degree of freedom is larger for the former than for the latter. However, difference in errors is not significant for the velocity.

The second test case is performed on hexahedral meshes in which the elements have a constant aspect ratio. The set of meshes $\{\mathcal{T}_h, h \in \mathcal{H}\}$ is not built by refinement, as shown in

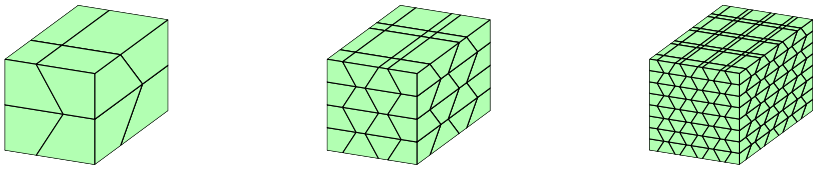

**Figure 3.6:** Family of hexahedral meshes with respectively 8, 64 and 512 hexahedra.

| | | Method 1 | | | | Method 2 | | | |
|---|---|---|---|---|---|---|---|---|---|
| | | $\|p-p_h\|_{0,\Omega}$ | | $\|\mathbf{u}-\mathbf{u}_h\|_{0,\Omega}$ | | $\|p-p_h\|_{0,\Omega}$ | | $\|\mathbf{u}-\mathbf{u}_h\|_{0,\Omega}$ | |
| $n$ | $h$ | error | rate | error | rate | error | rate | error | rate |
| 2 | $1.05 \cdot 10^{0}$ | $3.37 \cdot 10^{-1}$ | | $1.58 \cdot 10^{0}$ | | $3.37 \cdot 10^{-1}$ | | $9.74 \cdot 10^{-1}$ | |
| 4 | $5.66 \cdot 10^{-1}$ | $1.74 \cdot 10^{-1}$ | 0.96 | $2.17 \cdot 10^{0}$ | −0.45 | $1.72 \cdot 10^{-1}$ | 0.97 | $5.16 \cdot 10^{-1}$ | 0.92 |
| 8 | $2.83 \cdot 10^{-1}$ | $8.95 \cdot 10^{-2}$ | 0.96 | $2.45 \cdot 10^{0}$ | −0.17 | $8.63 \cdot 10^{-2}$ | 1.00 | $2.65 \cdot 10^{-1}$ | 0.96 |
| 16 | $1.41 \cdot 10^{-1}$ | $4.92 \cdot 10^{-2}$ | 0.86 | $2.59 \cdot 10^{0}$ | −0.08 | $4.31 \cdot 10^{-2}$ | 1.00 | $1.34 \cdot 10^{-1}$ | 0.98 |

**Table 3.3:** Convergence errors on the family of hexahedral meshes in Figure 3.6

| | | Method 1 | | | | Method 2 | | | |
|---|---|---|---|---|---|---|---|---|---|
| | | $\|p-p_h\|_{0,\Omega}$ | | $\|\mathbf{u}-\mathbf{u}_h\|_{0,\Omega}$ | | $\|p-p_h\|_{0,\Omega}$ | | $\|\mathbf{u}-\mathbf{u}_h\|_{0,\Omega}$ | |
| $n$ | $h$ | error | rate | error | rate | error | rate | error | rate |
| 2 | $9.19 \cdot 10^{-1}$ | $2.32 \cdot 10^{-1}$ | | $9.55 \cdot 10^{-1}$ | | $2.32 \cdot 10^{-1}$ | | $9.59 \cdot 10^{-1}$ | |
| 4 | $5.66 \cdot 10^{-1}$ | $1.22 \cdot 10^{-1}$ | 0.93 | $5.11 \cdot 10^{-1}$ | 0.90 | $1.22 \cdot 10^{-1}$ | 0.93 | $5.12 \cdot 10^{-1}$ | 0.91 |
| 8 | $2.83 \cdot 10^{-1}$ | $6.19 \cdot 10^{-2}$ | 0.98 | $2.64 \cdot 10^{-1}$ | 0.95 | $6.19 \cdot 10^{-2}$ | 0.98 | $2.64 \cdot 10^{-1}$ | 0.95 |
| 16 | $1.41 \cdot 10^{-1}$ | $3.12 \cdot 10^{-2}$ | 0.99 | $1.34 \cdot 10^{-1}$ | 0.98 | $3.12 \cdot 10^{-2}$ | 0.99 | $1.34 \cdot 10^{-1}$ | 0.98 |

**Table 3.4:** Convergence errors on the family of pyramidal meshes obtained from hexahedral meshes shown in Figure 3.6

Figure 3.6. The hexahedra have planar faces but do not come from a linear transformation of the reference element. The convergence errors on hexahedral meshes are shown in Table 3.3. The Method 1 does not converge because for hexahedra which make up the mesh, the condition $\phi_e(\mathbf{v}) = 0$ is not satisfied for constant velocities $\mathbf{v}$ on edges joining the barycenter to the vertices. This condition is only satisfied on regular hexahedra, as shown in Remark 3. Consequently, constant velocities are not inside the approximation space and convergence is not ensured by the Bramble-Hilbert lemma. In the other hand, the Method 2 converges as expected. We study next the convergence errors on the pyramidal meshes in Table 3.4. Similarly, the pyramids have a constant aspect ratio. Unlike the case of the hexahedral meshes, the Method 1 converges because by construction of the tetrahedral submesh, the constant velocities are always inside the approximation space. The Method 2 converges and we remark that the velocity error is the same on both kinds of meshes, as in the case of regular meshes,

### 3.6.2 Numerical experiments with meshes having curved faces

We have proven the convergence of both composite methods in Theorem 3.4.2 and in Theorem 3.5.2 when the mesh contains only planar faces. For meshes having curved faces, we approximate the curved faces by 4 triangular subfaces as shown in Figure 3.7a. Definitions of basis functions in (3.20) and (3.23) remain unchanged for both methods because normal components of basis functions at the boundary are defined on triangular subfaces.

Since triangular subfaces of a face have non constant normals, normal components of

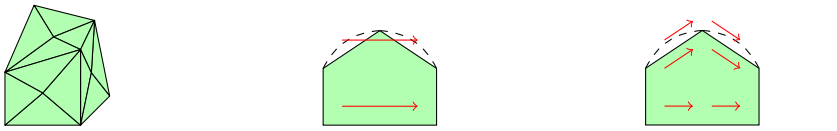

**(a)** Deformed hexahedron **(b)** Exact velocity **(c)** Approximate velocity

**Figure 3.7:** Example of deformed hexahedron, where a constant velocity and its approximation are shown on a diagonal cross section.


**Figure 3.8:** Mesh of the domain $\Omega$ having curved faces.

| | | Method 1 | | | | Method 2 | | | |
|---|---|---|---|---|---|---|---|---|---|
| | | $\|p - p_h\|_{0,\Omega}$ | | $\|\mathbf{u} - \mathbf{u}_h\|_{0,\Omega}$ | | $\|p - p_h\|_{0,\Omega}$ | | $\|\mathbf{u} - \mathbf{u}_h\|_{0,\Omega}$ | |
| $n$ | $h$ | error | rate | error | rate | error | rate | error | rate |
| 2 | $1.07 \cdot 10^{0}$ | $3.56 \cdot 10^{-1}$ | | $1.38 \cdot 10^{0}$ | | $3.56 \cdot 10^{-1}$ | | $1.10 \cdot 10^{0}$ | |
| 4 | $6.23 \cdot 10^{-1}$ | $1.80 \cdot 10^{-1}$ | 0.98 | $6.55 \cdot 10^{-1}$ | 1.07 | $1.80 \cdot 10^{-1}$ | 0.98 | $5.28 \cdot 10^{-1}$ | 1.06 |
| 8 | $3.47 \cdot 10^{-1}$ | $9.02 \cdot 10^{-2}$ | 1.00 | $3.22 \cdot 10^{-1}$ | 1.02 | $9.02 \cdot 10^{-2}$ | 1.00 | $2.61 \cdot 10^{-1}$ | 1.02 |
| 16 | $1.84 \cdot 10^{-1}$ | $4.51 \cdot 10^{-2}$ | 1.00 | $1.60 \cdot 10^{-1}$ | 1.01 | $4.51 \cdot 10^{-2}$ | 1.00 | $1.30 \cdot 10^{-1}$ | 1.00 |

**Table 3.5:** Convergence errors on the hexahedral meshes having curved faces in Figure 3.8

| | | Method 1 | | | | Method 2 | | | |
|---|---|---|---|---|---|---|---|---|---|
| | | $\|p - p_h\|_{0,\Omega}$ | | $\|\mathbf{u} - \mathbf{u}_h\|_{0,\Omega}$ | | $\|p - p_h\|_{0,\Omega}$ | | $\|\mathbf{u} - \mathbf{u}_h\|_{0,\Omega}$ | |
| $n$ | $h$ | error | rate | error | rate | error | rate | error | rate |
| 2 | $9.43 \cdot 10^{-1}$ | $2.39 \cdot 10^{-1}$ | | $1.09 \cdot 10^{0}$ | | $2.39 \cdot 10^{-1}$ | | $1.09 \cdot 10^{0}$ | |
| 4 | $5.37 \cdot 10^{-1}$ | $1.19 \cdot 10^{-1}$ | 1.00 | $5.20 \cdot 10^{-1}$ | 1.07 | $1.19 \cdot 10^{-1}$ | 1.00 | $5.20 \cdot 10^{-1}$ | 1.07 |
| 8 | $2.85 \cdot 10^{-1}$ | $5.97 \cdot 10^{-2}$ | 1.00 | $2.57 \cdot 10^{-1}$ | 1.02 | $5.97 \cdot 10^{-2}$ | 1.00 | $2.57 \cdot 10^{-1}$ | 1.02 |
| 16 | $1.47 \cdot 10^{-1}$ | $2.99 \cdot 10^{-2}$ | 1.00 | $1.28 \cdot 10^{-1}$ | 1.00 | $2.99 \cdot 10^{-2}$ | 1.00 | $1.28 \cdot 10^{-1}$ | 1.00 |

**Table 3.6:** Convergence errors on the pyramidal meshes having curved faces obtained from hexahedral meshes shown in Figure 3.8

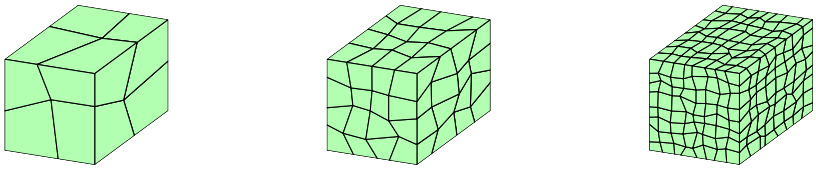

**Figure 3.9:** Family of random meshes with respectively 8, 64 and 512 deformed cubes.

| | | Method 1 | | | | Method 2 | | | |
|---|---|---|---|---|---|---|---|---|---|
| | | $\|p-p_h\|_{0,\Omega}$ | | $\|\mathbf{u}-\mathbf{u}_h\|_{0,\Omega}$ | | $\|p-p_h\|_{0,\Omega}$ | | $\|\mathbf{u}-\mathbf{u}_h\|_{0,\Omega}$ | |
| $n$ | $h$ | error | rate | error | rate | error | rate | error | rate |
| 2 | $1.08 \cdot 10^{0}$ | $3.64 \cdot 10^{-1}$ | | $1.31 \cdot 10^{0}$ | | $3.64 \cdot 10^{-1}$ | | $1.12 \cdot 10^{0}$ | |
| 4 | $5.71 \cdot 10^{-1}$ | $1.81 \cdot 10^{-1}$ | 1.01 | $1.48 \cdot 10^{0}$ | −0.17 | $1.80 \cdot 10^{-1}$ | 1.01 | $1.08 \cdot 10^{0}$ | 0.04 |
| 8 | $3.11 \cdot 10^{-1}$ | $9.29 \cdot 10^{-2}$ | 0.96 | $1.31 \cdot 10^{0}$ | 0.17 | $9.27 \cdot 10^{-2}$ | 0.96 | $8.58 \cdot 10^{-1}$ | 0.34 |
| 16 | $1.59 \cdot 10^{-1}$ | $4.68 \cdot 10^{-2}$ | 0.99 | $1.38 \cdot 10^{0}$ | −0.07 | $4.64 \cdot 10^{-2}$ | 1.00 | $8.92 \cdot 10^{-1}$ | −0.06 |

**Table 3.7:** Convergence errors on the family of random hexahedral meshes in Figure 3.9

| | | Method 1 | | | | Method 2 | | | |
|---|---|---|---|---|---|---|---|---|---|
| | | $\|p-p_h\|_{0,\Omega}$ | | $\|\mathbf{u}-\mathbf{u}_h\|_{0,\Omega}$ | | $\|p-p_h\|_{0,\Omega}$ | | $\|\mathbf{u}-\mathbf{u}_h\|_{0,\Omega}$ | |
| $n$ | $h$ | error | rate | error | rate | error | rate | error | rate |
| 2 | $9.01 \cdot 10^{-1}$ | $2.47 \cdot 10^{-1}$ | | $1.12 \cdot 10^{0}$ | | $2.47 \cdot 10^{-1}$ | | $1.12 \cdot 10^{0}$ | |
| 4 | $5.22 \cdot 10^{-1}$ | $1.23 \cdot 10^{-1}$ | 1.00 | $1.10 \cdot 10^{0}$ | 0.02 | $1.23 \cdot 10^{-1}$ | 1.01 | $1.10 \cdot 10^{0}$ | 0.02 |
| 8 | $2.68 \cdot 10^{-1}$ | $6.31 \cdot 10^{-2}$ | 0.96 | $8.79 \cdot 10^{-1}$ | 0.33 | $6.31 \cdot 10^{-2}$ | 0.96 | $8.74 \cdot 10^{-1}$ | 0.33 |
| 16 | $1.38 \cdot 10^{-1}$ | $3.17 \cdot 10^{-2}$ | 0.99 | $9.16 \cdot 10^{-1}$ | −0.06 | $3.17 \cdot 10^{-2}$ | 0.99 | $9.09 \cdot 10^{-1}$ | −0.06 |

**Table 3.8:** Convergence errors on the family of random pyramidal meshes obtained from hexahedral meshes shown in Figure 3.9

a constant velocity are different on each subfaces, and then different than its average value used by the projection operator on the face. Consequently, a constant velocity can be different from its projection into approximation space $\mathcal{W}_h$. Since constant velocities do not lie anymore in the approximation space, estimate given by the Bramble-Hilbert Lemma 3.3.1 does not hold.

As shown in Figure 3.7b on the diagonal cross section of the deformed cube, a constant velocity can go through the subfaces approaching the curved face. The closest approximation which can be done by the method is shown in Figure 3.7c, where approximate velocity stays inside the element by following the subfaces. It is shown in [63] that it is not possible to reproduce constant velocities with only one degree of freedom per face, and a compact stencil. However, we observe that the method converge while the mesh is refined in a standard manner:

The first mesh is built with a saddle point defined in $\Omega$ and shown in Figure 3.8, and the family of meshes $\{\mathcal{T}_h, h \in \mathcal{H}\}$ is built by refinement to approximate it. The convergence errors are shown in Table 3.5 if the mesh is made of hexahedra, and in Table 3.6 for pyramids. Here, we remark that both methods converge, and that the velocity approximated by the Method 2 is most accurate on pyramidal meshes.

Then we study the convergence of both methods on a family of random meshes shown in Figure 3.9. Each mesh is made up deformed cubes having curved faces. The aspect ratio of the elements is constant, like for the second test case. Table 3.7 and Table 3.8 show the errors of methods on both meshes. This time, the convergence is shown only for the pressure. It seems necessary to increase the degrees of freedom of the velocity to obtain a method

which converges on this kind of mesh.

## 3.7 A posteriori error estimate

We continue the analysis of the composite method by obtaining a posteriori error estimates for the method. From previous results, we decide to restrain this study for the hexahedral composite method, whose velocity basis functions are defined by the following Neumann problem:

$$\begin{aligned}
&\text{Find } \mathbf{w}_{E,F} \in \widetilde{\mathcal{W}}_E \text{ and } p_{E,F} \in \widetilde{\mathcal{M}}_E \text{ such that} \\
&\int_E \mathbf{K}^{-1}\mathbf{w}_{E,F}\cdot\mathbf{v} - \int_E p_{E,F}\,\nabla\cdot\mathbf{v} = 0 \quad && \forall \mathbf{v} \in \widetilde{\mathcal{W}}_E, \\
&\int_E \widetilde{q}\,\nabla\cdot\mathbf{w}_{E,F} = \frac{1}{|E|}\int_E \widetilde{q} && \forall \widetilde{q} \in \widetilde{\mathcal{M}}_E, \\
&\mathbf{w}_{E,F}\cdot\mathbf{n}_{\widetilde{F}} = \begin{cases} \dfrac{1}{|F|} & \text{if } \widetilde{F} \subset F, \\ 0 & \text{otherwise,} \end{cases} && \forall \widetilde{F} \in \mathcal{F}_E^{\text{ext}}, \\
&\int_E p_{E,F} = 0.
\end{aligned} \tag{3.26}$$

Adding the tensor $\mathbf{K}^{-1}$ does not change the convergence proof of the method, nor the obtained convergence results. However, we remark that the coefficients used to build the system (3.26) can be used another time to build the discrete problem $(\mathcal{P}_h)$. Approximation spaces are then defined similarly as for previous composite methods.

We also restrain our study to the error made by the approximate velocity. It will be used later to simulate the particles transport in the deep medium and depends on how the mesh is refined, when this one has curved faces. The velocity error is measured with the energy norm defined as follows:

$$\forall \mathbf{v} \in \mathcal{W}, \qquad |||\mathbf{v}|||_*^2 = \int_\Omega \mathbf{K}^{-1}\mathbf{v}\cdot\mathbf{v}, \qquad |||\mathbf{v}|||_{*,E}^2 = \int_E \mathbf{K}^{-1}\mathbf{v}\cdot\mathbf{v}, \qquad \forall E \in \mathcal{T}_h.$$

### 3.7.1 Definition of the error estimators

As in [77], the velocity error is bounded by using several estimators which are defined to bound the error caused by a specific parameter. The first of them is the residual estimator which is used to bound the error coming from the divergence approximation. Since it is piecewise constant on the elements of the mesh, its error is bounded using the projection error of the source term. The residual estimator is then defined as following:

**Lemma 3.7.1.** *Let $\mathbf{u} \in \mathcal{W}$ solve $(\mathcal{P})$ and $\mathbf{u}_h \in \mathcal{W}_h$ solve $(\mathcal{P}_h)$ such that $\nabla\cdot\mathbf{u}_h = \pi_h(f)$. The residual estimator is*

$$\forall E \in \mathcal{T}_h, \qquad \eta_{\mathrm{R},E} = h_E \frac{C_{\mathrm{p}}^{1/2}}{c_{\mathbf{K},E}^{1/2}} \|f - \pi_E(f)\|_{0,E}, \tag{3.27}$$

*where $h_E$ is the diameter of $E \in \mathcal{T}_h$, $C_{\mathrm{p}}$ is the Poincaré constant defined in* (3.9) *and where $c_{\mathbf{K},E}$ is the smallest eigenvalue of $\mathbf{K}$ in $E$. Moreover, we have that*

$$|||\mathbf{u} - \mathbf{u}_h|||_*^2 \leqslant \inf_{q \in H^1(\Omega)} |||\mathbf{u}_h + \mathbf{K}\,\nabla\, q|||_*^2 + \sum_{E \in \mathcal{T}_h} \eta_{\mathrm{R},E}^2. \tag{3.28}$$

*Proof.* The proof is similar to that in [77, Corollary 6.6] □

To complete our a posteriori error study, we have to find a function $\widetilde{p}_{h,2} \in H^1(\Omega)$ closed to the exact pressure to bound the equation (3.28). This function must be continuous on the domain, it will be defined as the projection of the hybrid solution onto the continuous space $H^1(\Omega)$. However, the hybrid solution can not be defined on the hexahedral mesh because the $\mathbf{RTN}_0$ method does not converge on irregular elements. Here, we take advantage that the union of tetrahedral submesh gives a conforming tetrahedral mesh of the domain.

Let $\widetilde{\mathcal{T}}_h = \bigcup_{E\in\mathcal{T}_h} \mathcal{T}_E$ be the tetrahedral submesh of the domain built by taking the union of tetrahedral submesh of each element. We denote respectively $\widetilde{\mathcal{M}}_h \subset \mathcal{M}$ and $\widetilde{\mathcal{W}}_h \subset \mathcal{W}$ the approximation spaces of the $\mathbf{RTN}_0$ method over the tetrahedral submesh, such that

$$\widetilde{\mathcal{M}}_h = \{q \in \mathcal{M} : q|_T \text{ is constant on } T,\ \forall T \in \widetilde{\mathcal{T}}_h\},$$
$$\widetilde{\mathcal{W}}_h = \{\mathbf{w} \in \mathcal{W} : \mathbf{w}|_T \in \mathbf{RTN}_0(T),\ \forall T \in \widetilde{\mathcal{T}}_h\}.$$

From the approximate solution given by the $\mathbf{RTN}_0$ method, we define a hybrid solution associated to the tetrahedral submesh of the domain. The approximate velocity given by the composite method is already inside $\widetilde{\mathcal{W}}_h$ by definition of the basis functions. However, the approximate pressure is only constant on hexahedra of the mesh. To have a pressure piecewise constant on the tetrahedral submesh, $p_h$ is completed with the pressure variations $p_{E,F}$ defined in (3.26). We define $\widetilde{\mathbf{u}}_h \in \widetilde{\mathcal{W}}_h$ and $\widetilde{p}_h \in \widetilde{\mathcal{M}}_h$ such that

$$\forall E \in \mathcal{T}_h, \qquad \widetilde{\mathbf{u}}_h|_E = \mathbf{u}_h, \qquad \widetilde{p}_h|_E = p_h + \sum_{F\in\mathcal{F}_E} p_{E,F} \int_F \mathbf{u}_h \cdot \mathbf{n}_F.$$

We define from these solution a discontinuous approximation of the pressure. Let $\mathbb{P}^2(\widetilde{\mathcal{T}}_h)$ be the space of discontinuous polynomial of degree at most $n$ on each tetrahedra $T \in \widetilde{\mathcal{T}}_h$. The hybrid form $\varphi_{h,2} \in \mathbb{P}^2(\widetilde{\mathcal{T}}_h)$ is computed by using the following properties:

$$\forall T \in \widetilde{\mathcal{T}}_h, \qquad \widetilde{\mathbf{u}}_h|_T = -\mathbf{K}\,\nabla\,\varphi_{h,2}, \qquad \widetilde{p}_h|_T = \frac{1}{|T|}\int_T \varphi_{h,2}. \tag{3.29}$$

The candidate $\widetilde{p}_{h,2} \in \mathbb{P}^2(\widetilde{\mathcal{T}}_h)\bigcap H^1(\Omega)$ used to estimate the velocity error in (3.28) is the projection of $\varphi_{h,2}$ into the continuous space $H^1(\Omega)$. We define then the averaging operator $\mathcal{I}_{\text{av}}\colon \mathbb{P}^2(\widetilde{\mathcal{T}}_h) \to \mathbb{P}^2(\widetilde{\mathcal{T}}_h)\bigcap H^1(\Omega)$ such that: for a function $\varphi \in \mathbb{P}^2(\widetilde{\mathcal{T}}_h)$ which is defined by its degrees of freedom at Lagrangian's nodes of each tetrahedra, values of the degrees of freedom of $\mathcal{I}_{\text{av}}(\varphi)$ are equal to the average of the degrees de freedom of $\varphi$. So we have

$$\widetilde{p}_{h,2} = \mathcal{I}_{\text{av}}(\varphi_{h,2}), \tag{3.30}$$

which allow us to define the second error estimator:

**Lemma 3.7.2.** *Let $\mathbf{u} \in \mathcal{W}$ solve $(\mathcal{P})$ and $\mathbf{u}_h \in \mathcal{W}$ solve $(\mathcal{P}_h)$. Let $\eta_{\text{R},E}$ be the residual estimator defined in* (3.27) *for all $E \in \mathcal{T}_h$, and $\widetilde{p}_{h,2} \in \mathbb{P}^2(\widetilde{\mathcal{T}}_h)\bigcap H^1(\Omega)$ defined in* (3.30)*. The potential estimator is*

$$\forall T \in \widetilde{\mathcal{T}}_h, \qquad \eta_{\text{P},T} = |||\widetilde{\mathbf{u}}_h + \mathbf{K}\,\nabla\,\widetilde{p}_{h,2}|||_{*,T}, \tag{3.31}$$

*and we obtain that*

$$|||\mathbf{u}-\mathbf{u}_h|||_*^2 \leqslant \eta_h^2, \qquad \eta_h^2 = \sum_{T\in\widetilde{\mathcal{T}}_h} \eta_{\mathrm{P},T}^2 + \sum_{E\in\mathcal{T}_h} \eta_{\mathrm{R},E}^2.$$

*Proof.* The estimate is just inequality (3.28) applied with $\widetilde{p}_{h,2}$. □

Moreover, a local efficiency result ensures that both estimators decrease at the same rate as the error. They are then reliable to approximate the error during the mesh refinement.

**Lemma 3.7.3.** *Let $p \in \mathcal{M}$, $\mathbf{u} \in \mathcal{W}$ solve $(\mathcal{P})$ and $p_h \in \mathcal{M}_h$, $\mathbf{u}_h \in \mathcal{W}$ solve $(\mathcal{P}_h)$. Let $\varphi_{h,2} \in \mathbb{P}^2(\widetilde{\mathcal{T}}_h)$ be the piecewise polynomial approximation of the pressure defined in* (3.29)*. Let the estimators $\eta_{\mathrm{R},E}$ and $\eta_{\mathrm{P},T}$ define respectively in* (3.27) *and* (3.31) *for $E \in \mathcal{T}_h$ and $T \in \widetilde{\mathcal{T}}_h$. Then there exists a constant $C$ independent of $h$ such that:*

$$\eta_{\mathrm{R},E} \leqslant C|||\mathbf{u}-\mathbf{u}_h|||_{*,E},$$
$$\eta_{\mathrm{P},T} \leqslant |||\mathbf{u}-\mathbf{u}_h|||_{*,T} + C|||p-\varphi_{h,2}|||_{*,\widetilde{\mathcal{T}}_T},$$

*where $\widetilde{\mathcal{T}}_T$ is the set of tetrahedra that share at least one node with $T$.*

*Proof.* The proof is similar to that in [77, Theorem 6.16]. □

Finally, a local estimator $\eta_E$ can be computed due to previous results:

$$\forall E \in \mathcal{T}_h, \qquad \eta_E^2 = \eta_{\mathrm{R},E}^2 + \sum_{T\in\mathcal{T}_E} \eta_{\mathrm{P},T}^2. \tag{3.32}$$

It can be used as a refinement criterion but the proof of local error estimate is an ongoing work.

### 3.7.2 Numerical experiments

The study of a posteriori error is performed on the unity cube, $\Omega = [0\,;1]^3$, meshed with regular hexahedra. The domain is split into two part $\Omega_r = [\frac{1}{2}\,;1]^3$ and $\Omega_g = \Omega\backslash\Omega_r$, shown respectively in red and in green in Figure 3.10. In this test case, source term $f = 0$ and the tensor $\mathbf{K}$ is discontinuous:

$$\mathbf{K} = \alpha \begin{pmatrix} 1 & 0 & 0 \\ 0 & 1 & 0 \\ 0 & 0 & 1 \end{pmatrix}, \qquad \begin{cases} \alpha = \dfrac{1}{10} & \text{in } \Omega_r, \\ \alpha = 1 & \text{in } \Omega_g, \end{cases}$$

Both Dirichlet and Neumann boundary conditions are set on the border of the domain:

- on the face $x = 0$, we set $p = 1$,
- on the face $x = 1$, we set $p = 0$,
- homogeneous Neumann boundary conditions are set on other faces of the domain.

From the chosen tensor $\mathbf{K}$ and boundary conditions, we deduce that the velocity goes through the domain from the face $x = 0$ to the face $x = 1$, and is 10 times smaller inside $\Omega_r$.

We show in Figure 3.11 the coefficients $\eta_E$ defined in (3.32) around the plane $x = \frac{1}{2}$, and on $x = \frac{2}{3}$. We can see that coefficient values are not uniform: maximum is reached on $x = \frac{1}{2}$ at the boundary edges of $\Omega_r$ where the coefficient increases up to $6 \cdot 10^{-3}$, whereas on boundary face of $\Omega_r$, it decreases to $5 \cdot 10^{-6}$. This shows that contrary to what one may

think, this is not necessary to refine the mesh on all boundary between $\Omega_r$ and $\Omega_g$, but only one part of it.

This analysis is confirmed by computing another kind of estimator. Figure 3.12 shows the error of approximate velocity using a finer mesh. However we recall that approximate velocity is inside $\mathbf{RTN}_0$ approximate space of the tetrahedral submesh, and therefore this estimator can be computed only because we use a regular mesh with few elements. We can see that errors are distributes similarly than the coefficients $\eta_E$, even though the errors are smaller on $x = \frac{1}{2}$.

Table 3.9 compares the global a posteriori error estimator $\eta_h$ with the approximate error $|||\mathbf{u}_h - \mathbf{u}_{\frac{h}{4}}|||_*$. The estimator $\eta_h$ is greater than the error approximated by a finer mesh but both have the same order of magnitude. They also converge at the same rate which is smaller than 1, because the error is concentrated in a small area of the mesh.

## 3.8 A realistic numerical experiment with parallel computing

The last experiment is done on an industrial test case. Figure 3.13 shows the domain of calculation provided by engineers from *Andra*. It describes underground of Meuse/Haute-Marne districts. The mesh contains a little fewer than 6 millions of elements, most are deformed cubes used to mesh the surface together with geological layers of the domain. Prisms are added to refined locally the mesh around potential location of waste repository, which is shown in pink.

Compared to previous numerical experiments which are performed on the unity cube, characteristics of this industrial test case makes the discrete problem $(\mathcal{P}_h)$ harder to solve:

- The domain is large and flat. It varies of 30 (km) in both $x$ and $y$ directions, and only 1 (km) in the $z$ direction. Consequently, tetrahedral submesh built on deformed cubes is flat, which makes local problem (3.26) used to define basis functions ill conditioned.
- Permeability tensor $\mathbf{K}$ is anisotropic and its coefficients vary strongly from a geological layers to another. The permeability jumps between two geological layers can reach six order of magnitude. Its trace is shown in Figure 3.14 using a logarithmic scale.

The composite method is compared with a $\mathbf{RTN}_0$ method of lowest order extended to deformed cubes. We compare the obtained results on an horizontal cross section located in the middle of the domain, shown in blue in Figure 3.13b.

The pressure fields which are similar for both methods, are shown in Figure 3.15. The main difference between both methods comes from the velocity fields in Figure 3.16, where is shown the $\mathbf{L}^2$ norm of approximate velocities. Compared to the composite method, the norm of the $\mathbf{RTN}_0$ method extended to deformed cubes reaches a non-physical value of $6 \cdot 10^3$, which hides the behavior of velocity in the domain. Its maximum value is clipped in Figure 3.17 to fit to the range of values of the composite method. In this figure, we can see that velocity norm varies according to the permeability tensor, excepts for a small area circled in red where deformations of elements are stronger. Note that this lack of precision of the extended $\mathbf{RTN}_0$ method is important since it will affect the calculation of the transport of radioactive particles.

The numerical results have been obtained using the *Traces* code developed by *Andra* where the composite method has been implemented. It uses the parallel algebraic linear solver MaPHyS [2] based on a domain decomposition method with a direct subdomain solver. Note that if the nonphysical values of the velocity calculated by the extended $\mathbf{RTN}_0$ method

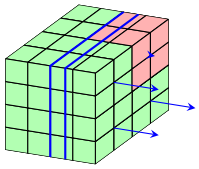

**Figure 3.10:** Domain $\Omega$ with the planes $x = \frac{1}{2}$ and $x = \frac{2}{3}$. The domain $\Omega_r$ is shown in red and $\Omega_g$ in green. The velocity is assumed to move 10 time slower in $\Omega_r$, according to the variation of $\mathbf{K}$.

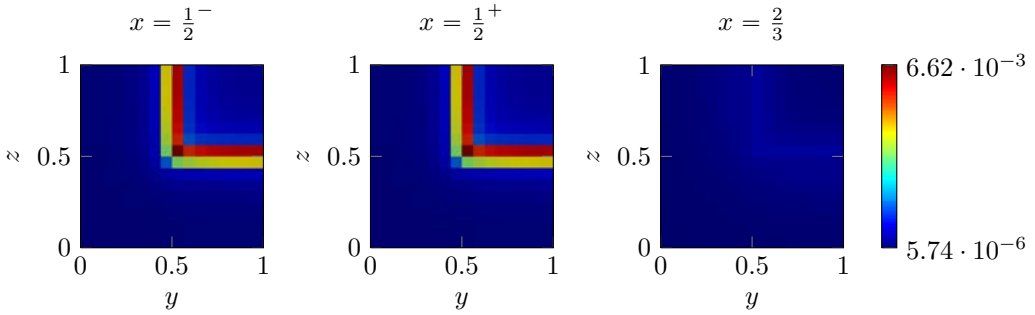


**Figure 3.11:** Coefficients $\eta_E$, around the plane $x = \frac{1}{2}$ and on $x = \frac{2}{3}$

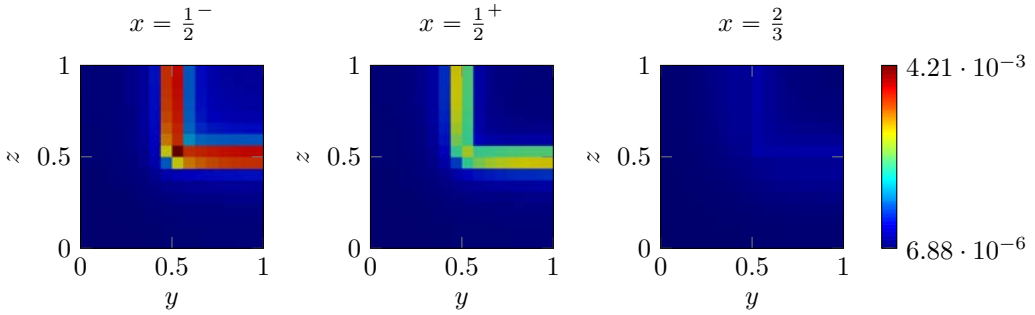


**Figure 3.12:** Approximate error computed using a mesh 4 times finer, $|||\mathbf{u}_h - \mathbf{u}_{\frac{h}{4}}|||_{*,E}$ around the plan $x = \frac{1}{2}$ and on $x = \frac{2}{3}$

| | | | error estimates | | |
|---|---|---|---|---|---|
| $n$ | $h$ | $\eta_h$ | rate | $\|\mathbf{u}_h - \mathbf{u}_{\frac{h}{4}}\|_*$ | rate |
| 2 | $8.66 \cdot 10^{-1}$ | $1.73 \cdot 10^{-1}$ | | $1.15 \cdot 10^{-1}$ | |
| 4 | $4.33 \cdot 10^{-1}$ | $1.07 \cdot 10^{-1}$ | 0.70 | $7.16 \cdot 10^{-2}$ | 0.68 |
| 8 | $2.17 \cdot 10^{-1}$ | $6.49 \cdot 10^{-2}$ | 0.72 | $4.40 \cdot 10^{-2}$ | 0.70 |
| 16 | $1.08 \cdot 10^{-1}$ | $3.92 \cdot 10^{-2}$ | 0.72 | $2.68 \cdot 10^{-2}$ | 0.72 |

**Table 3.9:** Convergence of the global a posteriori error estimate and an approximate error computed with a finer mesh.

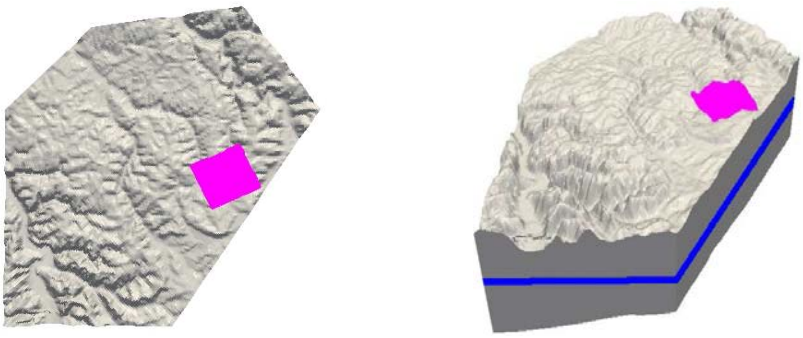

**(a)** Above view **(b)** Side view enlarge 10 time in the $z$ axis

**Figure 3.13:** Computational domain modeling Meuse/Haute Marne district. Pink area is refined locally using prisms. Solutions of both methods are studied on the blue cross section.

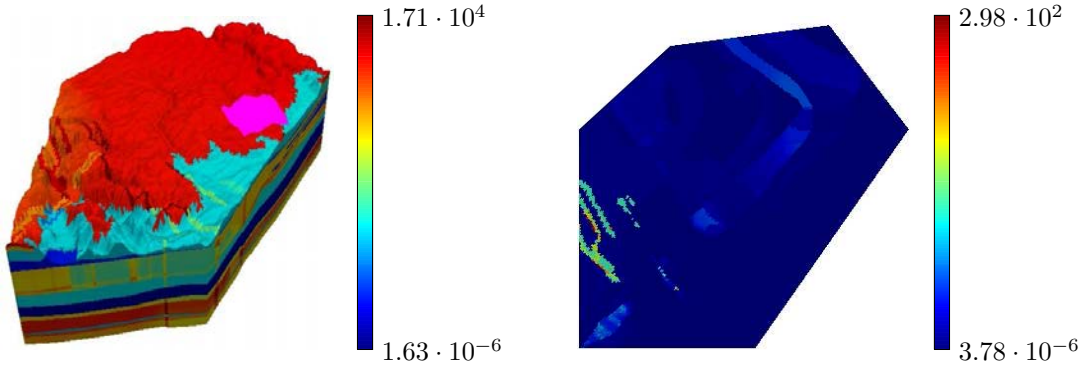


**(a)** on the domain $\Omega$ **(b)** on the horizontal cross section.

**Figure 3.14:** Trace of permeability tensor $\mathbf{K}$ in logarithmic scale

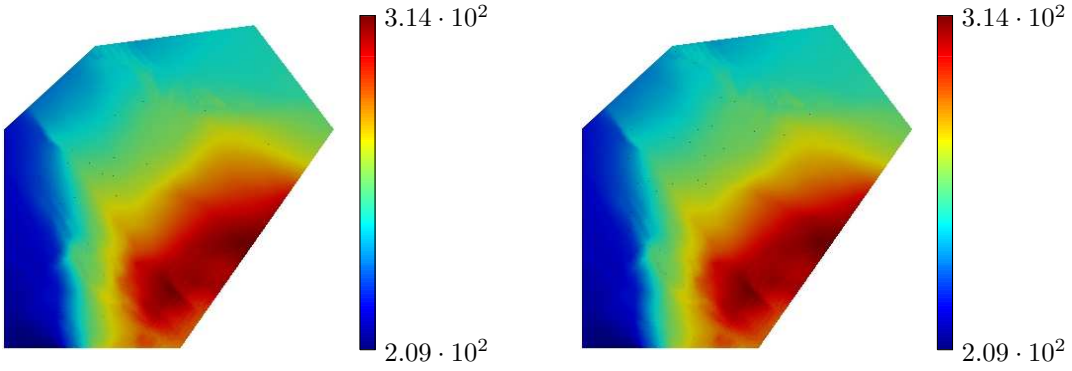


**(a)** $\mathbf{RTN}_0$ method extended to deformed cubes **(b)** Composite method

**Figure 3.15:** Approximate pressure on the horizontal cross section of $\Omega$.

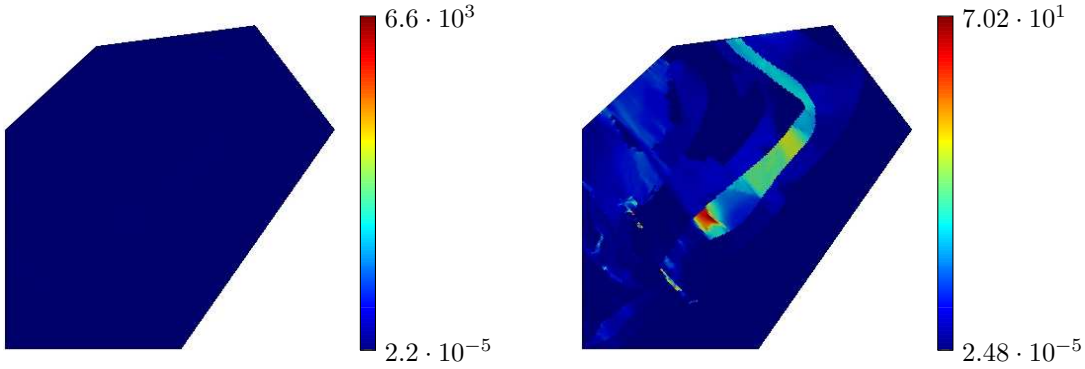


**(a)** $\mathbf{RTN}_0$ method extended to deformed cubes

**(b)** Composite method

**Figure 3.16:** $\mathbf{L}^2$ norm of approximate velocities on the horizontal cross section of $\Omega$.

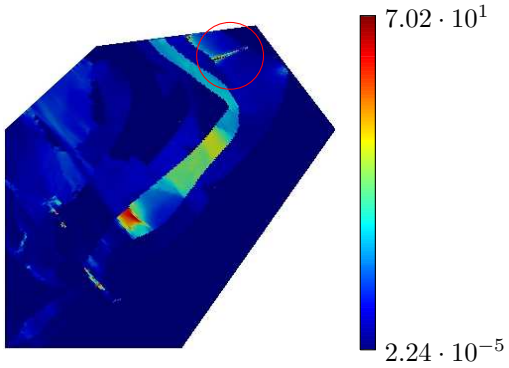


**Figure 3.17:** $\mathbf{L}^2$ norm of velocity approximated by the $\mathbf{RTN}_0$ method extended to deformed cubes, on the horizontal cross section of $\Omega$. The norm is clipped to fit to the range of the composite method. The non-physic maximum jump is located inside the red circle.

are located at the interfaces between subdomains, then the MaPHyS solver may crash. When using the composite method which does not produce such nonphysical values of the velocity, the solution is obtained without any difficulty.

## 3.9 Conclusion

We developed two composite methods, one for pyramids and one for polyhedra. The pyramidal composite method is an extension of the method presented in [17] in two dimensions. A pyramid is split into 4 tetrahedra such that the node added on its basis is the barycenter of the vertices. The velocity basis functions belong to the $\mathbf{RTN}_0$ approximation space defined on the tetrahedral submesh. The velocity basis functions are defined by (3.20) and are given explicitly by solving the systems (3.19). Consequently, the constant velocities are inside the approximation space because the average value of their normal components on internal faces are zero. This ensures the convergence of the method. However, this is no longer true if we try to apply the same method to any polyhedra.

The extension of composite method for polyhedra is similar to that presented in [71]. The tetrahedral submesh is built by adding an internal node and by splitting each of its faces. In particular, an hexahedron is divided into 24 tetrahedra. The new tetrahedral submesh has good symmetry properties but there are no explicit formula for the basis functions. Basis functions are computed by solving the Neumann problem (3.23), which ensures that the constant velocities are inside the approximate space and that the method is convergent. This method can be easily extended to any polyhedra, in particular to prisms.

Theoretical convergence of both methods with optimal order have been proved and was confirmed by numerical experiments. Concerning the case of meshes with curved faces, numerical experiments show converge of both methods only when using standard refinements of the mesh.

A posteriori error estimates have been defined for polyhedral method and shown to be optimal theoretically and numerically.

Finally, the hexahedral composite method has been compared with an extension of the $\mathbf{RTN}_0$ method on a realistic numerical experiment provided by *Andra*. The domain of calculation is large and has industrial characteristics. As expected, the composite method gives satisfying results while the standard $\mathbf{RTN}_0$ method was giving erroneous results for the velocities at some locations in the mesh. The composite method was implemented in an *Andra* software using the massively parallel hybrid solver MaPHyS [2] for parallel computations.

## 3.A Appendix: Trace inequalities

The trace inequalities used for the convergence proof of the composite methods are given in this section. Firstly, we state a general theorem given in [45, Lemma 3] for hexahedra and pyramids, necessary to prove the trace inequalities.

**Lemma 3.A.1.** *Let $E \subset \mathbb{R}^3$ be an hexahedron or a pyramid of diameter $h_E$. Let $F \subset \partial E$ be a face of $E$. For $g \in H^1(E)$, we have the estimate:*

$$\int_F \int_E (g(x) - g(y))^2 \,\mathrm{d}y \,\mathrm{d}x \leqslant C h_E^{d+1} \int_E |\nabla\, g(x))|^2 \,\mathrm{d}x,$$

*where $C$ is a positive constant independent of $h_E$.*

*Proof.* The proof is similar to that given in [45, Lemma 3]. □

From Lemma 3.A.1, we deduce several inequalities given below. Estimation (3.33) has been proven for simplexes in [74, Lemma 3.12] and in [48, Theorem 1.5.1.10]. Another proof is given in [27, Theorem 4.1] for the case of two dimensions. The estimate (3.34) is shown in [45, Lemma 2] and [62, Lemma 3.5] for several kinds of elements. The estimate (3.36) is shown in [75, Lemma 4.1] for simplexes elements.

**Lemma 3.A.2.** *Let $E \subset \mathbb{R}$ be an hexahedron or a pyramid of diameter $h_E$, and let $F \subset \partial E$ be a face of $E$. For $g \in H^1(E)$, with $g_F$ and $g_E$ denoting the average value of $g$ over $F$ and $E$ respectively,*

$$g_F := \frac{1}{|F|}\int_F g(x)\,\mathrm{d}x, \qquad\qquad g_E := \frac{1}{|E|}\int_E g(x)\,\mathrm{d}x,$$

*the following estimates hold for a generic constant $C > 0$ independent of $h_E$:*

$$\int_F g(x)^2\,\mathrm{d}x \leqslant C\left(dh_E\int_E |\nabla g(x)|^2\,\mathrm{d}x + 2h_E^{-1}\int_E g(x)^2\,\mathrm{d}x\right). \tag{3.33}$$

$$\int_F (g(x)-g_F)^2\,\mathrm{d}x \leqslant Ch_E\int_E |\nabla g(x)|^2\,\mathrm{d}x. \tag{3.34}$$

$$\int_F (g(x)-g_E)^2\,\mathrm{d}x \leqslant Ch_E\int_E |\nabla g(x)|^2\,\mathrm{d}x. \tag{3.35}$$

$$\int_E (g(x)-g_F)^2\,\mathrm{d}x \leqslant Ch_E^2\int_E |\nabla g(x)|^2\,\mathrm{d}x. \tag{3.36}$$

*Proof.* Let $E \subset \mathbb{R}$ be an hexahedron or a pyramid, $F \subset \partial E$, and $g \in H^1(E)$. To show (3.33), we note that if $x \in F$,

$$g(x) = \frac{1}{|E|}\int_E (g(x)-g(y))\,\mathrm{d}y + \frac{1}{|E|}\int_E g(y)\,\mathrm{d}y,$$

and therefore

$$g(x)^2 \leqslant 2\left(\frac{1}{|E|}\int_E (g(x)-g(y))\,\mathrm{d}y\right)^2 + 2\left(\frac{1}{|E|}\int_E g(y)\,\mathrm{d}y\right)^2.$$

If we integrate over the above equation over $F$, we obtain using the Cauchy-Schwarz inequality that

$$\int_F g(x)^2\,\mathrm{d}x \leqslant \frac{2}{|E|}\int_F\int_E (g(x)-g(y))^2\,\mathrm{d}y\,\mathrm{d}x + \frac{2|F|}{|E|}\int_E g(y)^2\,\mathrm{d}y,$$

which can be rewritten as (3.33) using Lemma 3.A.1.

To establish estimate (3.34), we note that for $x \in F$ and $y \in E$,

$$\begin{aligned}(g(x)-g_F)^2 &\leqslant 2(g(x)-g(y))^2 + 2(g(y)-g_F)^2\\ &\leqslant 2(g(x)-g(y))^2 + 2\left(\frac{1}{|F|}\int_F g(y)-g(t)\,\mathrm{d}t\right)^2.\end{aligned}$$

Then by using the Cauchy-Schwarz inequality, we have

$$(g(x)-g_F)^2 \leqslant 2(g(x)-g(y))^2 + \frac{2}{|F|}\int_F (g(y)-g(t))^2\,\mathrm{d}t.$$

Integrating over $E$ and $F$, we obtain

$$|E| \int_F (g(x) - g_F)^2 \, \mathrm{d}x \leqslant 4 \int_E \int_F (g(y) - g(t))^2 \, \mathrm{d}t \, \mathrm{d}y.$$

Applying Fubini's theorem and Lemma 3.A.1 gives (3.34).

For (3.35),

$$\int_F (g(x) - g_E)^2 \, \mathrm{d}x = \int_F \left( \frac{1}{|E|} \int_E g(x) - g(y) \, \mathrm{d}y \right)^2 \mathrm{d}x.$$

By using once again the Cauchy-Schwarz inequality, we obtain

$$\int_F (g(x) - g_E)^2 \, \mathrm{d}x \leqslant \frac{1}{|E|} \int_F \int_E (g(x) - g(y))^2 \, \mathrm{d}y \, \mathrm{d}x,$$

which gives (3.35) using Lemma 3.A.1.

Finally for (3.36), we have

$$\int_E (g(x) - g_F)^2 \, \mathrm{d}x = \int_E \left( \frac{1}{|F|} \int_F g(x) - g(y) \, \mathrm{d}y \right)^2 \mathrm{d}x.$$

Then by using the Cauchy-Schwarz inequality, we obtain

$$\int_E (g(x) - g_F)^2 \, \mathrm{d}x \leqslant \frac{1}{|F|} \int_E \int_F (g(x) - g(y))^2 \, \mathrm{d}y \, \mathrm{d}x,$$

which gives (3.36) using Fubini's theorem and Lemma 3.A.1. □

# Bibliography


[1] I. Aavatsmark, G. T. Eigestad, B.-o. Heimsund, B. Mallison, J. M. Nordbotten, E. Øian, et al. A new finite-volume approach to efficient discretization on challenging grids. *SPE Journal*, 15(03):658--669, 2010.

[2] E. Agullo, L. Giraud, A. Guermouche, A. Haidar, and J. Roman. MaPHyS or the development of a parallel algebraic domain decomposition solver in the course of the solstice project. In *Sparse Days 2010 Meeting at CERFACS*, Toulouse, France, June 2010.

[3] T. Arbogast. Mixed multiscale methods for heterogeneous elliptic problems. *Lecture Notes in Computational Science and Engineering*, 83:243--283, 2012.

[4] T. Arbogast and Z. Chen. On the Implementation of Mixed Methods As Nonconforming Methods for Second-order Elliptic Problems. *Math. Comput.*, 64(211):943--972, July 1995.

[5] T. Arbogast and M. R. Correa. Two families of $H(\mathrm{div})$ mixed finite elements on quadrilaterals of minimal dimension. *ICES Report*, pages 15--09, 2015. submitted.

[6] T. Arbogast, C. N. Dawson, P. T. Keenan, M. F. Wheeler, and I. Yotov. Enhanced cell-centered finite differences for elliptic equations on general geometry. *SIAM Journal on Scientific Computing*, 19(2):404--425, 1998.

[7] T. Arbogast, M. F. Wheeler, and I. Yotov. Mixed finite elements for elliptic problems with tensor coefficients as cell-centered finite differences. *SIAM Journal on Numerical Analysis*, 34(2):828--852, 1997.

[8] D. N. Arnold, D. Boffi, and R. S. Falk. Approximation by quadrilateral finite elements. *Mathematics of computation*, 71(239):909--922, 2002.

[9] D. N. Arnold, D. Boffi, and R. S. Falk. Quadrilateral $H(\mathrm{div})$ finite elements. *SIAM Journal on Numerical Analysis*, 42(6):2429--2451, 2005.

[10] D. N. Arnold and F. Brezzi. Mixed and nonconforming finite element methods: implementation, postprocessing and error estimates. *RAIRO Modél. Math. Anal. Numér.*, 19(1):7--32, 1985.

[11] J. Baranger, J.-F. Maitre, and F. Oudin. Connection between finite volume and mixed finite element methods. *Modél. Math. Anal. Numer.*, 30:444--465, 1996.

[12] M. Bause and P. Knabner. Computation of variably saturated subsurface flow by adaptive mixed hybrid finite element methods. *Advances in Water Resources*, 27:565--581, 2004.

[13] J. Bear. *Dynamics of Fluids in Porous Media*. Dover, New York, 1988.

[14] M. Bebendorf. A note on the Poincaré inequality for convex domains. *Zeitschrift für Analysis und ihre Anwendungen*, page 751–756, 2003.

[15] A. Bermúdez, P. Gamallo, M. R. Nogueiras, and R. Rodríguez. Approximation properties of lowest-order hexahedral raviart--thomas finite elements. *Comptes Rendus de l'Académie des Sciences*, 340(9):687--692, 2005.

[16] H. Bhatia, G. Norgard, V. Pascucci, and P.-T. Bremer. The Helmholtz-Hodge decomposition --- A Survey. *IEEE Trans. Visual. Comput. Graphics*, 19(8):1386–1404, 2013.

[17] N. Birgle, J. Jaffré, and J. E. Roberts. A 2-D composite polygonal mixed finite element. *M2AN Math. Model. Numer. Anal.*, . In preparation.

[18] N. Birgle, J. Jaffré, and J. E. Roberts. A composite mixed finite element for meshes of deformed cubes. ., . In preparation.

[19] D. Boffi, F. Brezzi, and M. Fortin. *Mixed finite element methods and applications*. Springer, 2013.

[20] J. H. Bramble and S. Hilbert. Estimation of linear functionals on Sobolev spaces with application to fourier transforms and spline interpolation. *SIAM Journal on Numerical Analysis*, 7(1):112--124, 1970.

[21] F. Brezzi. On the existence, uniqueness and approximation of saddle-point problems arising from Lagrangian multipliers. *ESAIM: Mathematical Modelling and Numerical Analysis-Modélisation Mathématique et Analyse Numérique*, 8(R2):129--151, 1974.

[22] F. Brezzi, J. Douglas Jr, R. Durán, and M. Fortin. Mixed finite elements for second order elliptic problems in three variables. *Numerische Mathematik*, 51(2):237--250, 1987.

[23] F. Brezzi, J. Douglas Jr, M. Fortin, and L. D. Marini. Efficient rectangular mixed finite elements in two and three space variables. *Modélisation mathématique et analyse numérique*, 21(4):581--604, 1987.

[24] F. Brezzi, J. Douglas Jr, and L. D. Marini. Two families of mixed finite elements for second order elliptic problems. *Numerische Mathematik*, 47(2):217--235, 1985.

[25] F. Brezzi, K. Lipnikov, and M. Shashkov. Convergence of mimetic finite difference method for diffusion problems on polyhedral meshes with curved faces. *Mathematical Models and Methods in Applied Sciences*, 16(02):275--297, 2006.

[26] F. Brezzi, K. Lipnikov, M. Shashkov, and V. Simoncini. A new discretization methodology for diffusion problems on generalized polyhedral meshes. *Computer Methods in Applied Mechanics and Engineering*, 196(37):3682--3692, 2007.

[27] C. Carstensen and S. A. Funken. Constants in Clément-interpolation error and residual based a posteriori estimates in finite element methods. *East-West J. Numer. Math*, 8(3):153--175, 2000.

[28] G. Chavent and J. Jaffré. *Mathematical Models and Finite Elements for Reservoir Simulation*. North Holland, Amsterdam, 1986.

[29] G. Chavent, J. Jaffré, G. C. Cohen, and B. Cockburn. Une methode d'elements finis pour la simulation dans un reservoir de deplacements bidimensionnels d'huile par de l'eau. Technical Report RR-0353, INRIA, 1985.

[30] G. Chavent and J. Roberts. A unified physical presentation of mixed, mixed-hybrid finite elements and standard finite difference approximations for the determination of velocities in waterflow problems. *Advances in Water Resources*, 14(6):329--348, 1991.

[31] Z. Chen. *Finite element methods and their applications*. Springer, 2005.

[32] Z. Chen. *Reservoir simulation: mathematics of oil recovery*. SIAM, 2007.

[33] Z. Chen and J. Douglas Jr. Prismatic mixed finite elements for second order elliptic problems. *CALCOLO*, 26(2-4):135--148, 1989.

[34] A. J. Chorin, J. E. Marsden, and J. E. Marsden. *A mathematical introduction to fluid mechanics*, volume 3. Springer, 1990.

[35] C. DAngelo and A. Scotti. A mixed finite element method for darcy flow in fractured porous media with non-matching grids. *ESAIM: Mathematical Modelling and Numerical Analysis*, 46:465--489, 2012.

[36] A. Datta-Gupta and M. J. King. *Streamline simulation: theory and practice*, volume 11. Society of Petroleum Engineers, 2007.

[37] D. A. Di Pietro and A. Ern. *Mathematical aspects of discontinuous Galerkin methods*, volume 69. Springer Science & Business Media, 2011.

[38] D. A. Di Pietro and A. Ern. Arbitrary-order mixed methods for heterogeneous anisotropic diffusion on general meshes. *IMA J. Numer. Math.*, 2016. Accepted for publication.

[39] D. A. Di Pietro, A. Ern, and S. Lemaire. An arbitrary-order and compact-stencil discretization of diffusion on general meshes based on local reconstruction operators. *Computational Methods in Applied Mathematics*, 14(4):461--472, 2014.

[40] J. Douglas Jr, R. E. Ewing, and M. F. Wheeler. The approximation of the pressure by a mixed method in the simulation of miscible displacement. *ESAIM: Mathematical Modelling and Numerical Analysis - Modélisation Mathématique et Analyse Numérique*, 17(1):17--33, 1983.

[41] J. Douglas Jr and J. E. Roberts. Numerical Methods for a Model for Compressible Miscible Displacement in Porous Media. *Mathematics of Computation*, 41(164):441--459, 1983.

[42] J. Droniou, R. Eymard, T. Gallouët, and R. Herbin. A unified approach to mimetic finite difference, hybrid finite volume and mixed finite volume methods. *Mathematical Models and Methods in Applied Sciences*, 20(02):265--295, 2010.

[43] E. Dubach, R. Luce, and J.-M. Thomas. Pseudo-conforming polynomial finite elements on quadrilaterals. *International Journal of Computer Mathematics*, 86(10-11):1798--1816, 2009.

[44] R. Eymard, T. Gallouët, and R. Herbin. The finite volume method. In P. Ciarlet and J. L. Lions, editors, *Handbook for Numerical Analysis*, volume 7, pages 715--1022. North Holland, 2000.

[45] R. Eymard, T. Gallouët, and R. Herbin. Finite volume approximation of elliptic problems and convergence of an approximate gradient. *Applied Numerical Mathematics*, 37(1-2):31–53, Apr 2001.

[46] R. Eymard, T. Gallouët, and R. Herbin. Discretisation of heterogeneous and anisotropic diffusion problems on general non-conforming meshes. SUSHI: a scheme using stabilisation and hybrid interfaces. *IMA J Numer Anal*, 30(4):1009--1043, 2010.

[47] B. Ganis, I. Yotov, and M. Zhong. A stochastic mortar mixed finite element method for flow in porous media with multiple rock types. *SIAM Journal on Scientific Computing*, 33:1439--1474, 2011.

[48] P. Grisvard. *Elliptic problems in nonsmooth domains*, volume 69. SIAM, 2011.

[49] H. Hægland, H. Dahle, G. Eigestad, K.-A. Lie, and I. Aavatsmark. Improved streamlines and time-of-flight for streamline simulation on irregular grids. *Advances in Water Resources*, 30(4):1027--1045, 2007.

[50] H. Hoteit. *Simulation d'écoulements et de transports de polluants en milieu poreux : application à la modélisation de la sûreté des dépôts de déchets radioactifs.* PhD thesis, Rennes 1, IFSIC, 2002.

[51] H. Hoteit, J. Erhel, R. Mosé, B. Philippe, and P. Ackerer. Numerical reliability for mixed methods applied to flow problems in porous media. *Computational geosciences*, 6(2):161--194, 2002.

[52] J. Jaffré. Décentrage et éléments finis mixtes pour les équations de diffusion-convection. *CALCOLO*, 21(2):171--197, 1984.

[53] Y. Kuznetsov, K. Lipnikov, and M. Shashkov. The mimetic finite difference method on polygonal meshes for diffusion-type problems. *Computational Geosciences*, 8(4):301--324, 2004.

[54] Y. Kuznetsov and S. Repin. New mixed finite element method on polygonal and polyhedral meshes. *Russian J. Numer. Anal. Math. Modelling*, 18(3):261--278, 2003.

[55] Y. Kuznetsov and S. Repin. Convergence analysis and error estimates for mixed finite element method on distorted meshes. *Russian J. Numer. Anal. Math. Modelling*, 13(1):33--51, 2005.

[56] K. Lipnikov, M. Shashkov, and D. Svyatskiy. The mimetic finite difference discretization of diffusion problem on unstructured polyhedral meshes. *Journal of Computational Physics*, 211(2):473--491, 2006.

[57] S. M. *Conservative Finite-difference Methods on general grids.* CRC Press, New York, 1996.

[58] G. d. Marsily. *Hydrogéologie quantitative.* Masson, 1981.

[59] V. Martin, J. Jaffré, and J. E. Roberts. Modeling fractures and barriers as interfaces for flow in porous media. *SIAM J. Sci. Comput.*, 26:1667--1691, 2005.

[60] R. L. Naff, T. F. Russell, and J. D. Wilson. Shape functions for velocity interpolation in general hexahedral cells. *Computational Geosciences*, 6(3-4):285--314, 2002.

[61] J.-C. Nédélec. Mixed finite elements in ℝ3. *Numerische Mathematik*, 35(3):315--341, 1980.

[62] S. Nicaise. A posteriori error estimations of some cell-centered finite volume methods. *SIAM Journal on Numerical Analysis*, 43(4):1481--1503, 2005.

[63] J. Nordbotten and H. Hægland. On reproducing uniform flow exactly on general hexahedral cells using one degree of freedom per surface. *Advances in Water Resources*, 32(2):264--267, 2009.

[64] L. E. Payne and H. F. Weinberger. An optimal Poincaré inequality for convex domains. *Archive for Rational Mechanics and Analysis*, 5(1):286--292, 1960.

[65] I. S. Pop, F. Radu, and P. Knabner. Mixed finite elements for the Richards equation: linearization procedure. *Journal of computational and applied mathematics*, 168:365--373, 2004.

[66] P.-A. Raviart and J.-M. Thomas. A mixed finite element method for 2nd order elliptic problems. In I. Galligani and E. Magenes, editors, *Mathematical Aspects of Finite Element Methods*, pages 292--315. Springer, 1977.

[67] D. S. Richeson. *Euler's Gem: The polyhedron formula and the birth of topology.* Princeton University Press, 2012.

[68] J. E. Roberts and J.-M. Thomas. Mixed and hybrid methods. In P. Ciarlet and J.-L. Lions, editors, *Handbook of Numerical Analysis*, volume 2, pages 523--633. North--Holland, Amsterdam, 1991.

[69] T. F. Russell and M. F. Wheeler. Finite element and finite difference methods for continuous flows in porous media. In R. E. Ewing, editor, *The Mathematics of Reservoir Simulation.* SIAM, Philadelphia, PA, 1983.

[70] A. Sboui. *Quelques méthodes numériques robustes pour l'écoulement et le transport en milieu poreux.* PhD thesis, Université Paris Dauphine, 2007.

[71] A. Sboui, J. Jaffré, and J. Roberts. A composite mixed finite element for hexahedral grids. *SIAM Journal on Scientific Computing*, 31(4):2623--2645, 2009.

[72] J. Shen. Mixed finite element methods on distorted rectangular grids. *Technical Report ISC*, 1994.

[73] W. Sprössig. On Helmholtz decompositions and their generalizations-an overview. *Mathematical Methods in the Applied Sciences*, 33(4):374--383, 2010.

[74] A. F. Stephansen. *Discountinuous Galerkin methods and posteriori error analysis for heterogeneous diffusion problems.* Theses, Ecole des Ponts ParisTech, 2007.

[75] M. Vohralík. On the discrete Poincaré--Friedrichs inequalities for nonconforming approximations of the Sobolev space H 1. *Numerical Functional Analysis and Optimization*, 26(7-8):925--952, 2005.

[76] M. Vohralík. A posteriori error estimates for lowest-order mixed finite element discretizations of convection-diffusion-reaction equations. *SIAM Journal on Numerical Analysis*, 45(4):pp. 1570--1599, 2007.

[77] M. Vohralík. Unified primal formulation-based a priori and a posteriori error analysis of mixed finite element methods. *Mathematics of Computation*, 79(272):2001--2032, 2010.

[78] M. Vohralík and B. I. Wohlmuth. Mixed finite element methods: implementation with one unknown per element, local flux expressions, positivity, polygonal meshes, and relations to other methods. *Mathematical Models and Methods in Applied Sciences*, 23(05):803--838, 2013.

[79] Vohralík, Martin. Equivalence between lowest-order mixed finite element and multi-point finite volume methods on simplicial meshes. *ESAIM: M2AN*, 40(2):367--391, 2006.

[80] A. Weiser and M. F. Wheeler. On Convergence of Block-Centered Finite Differences for Elliptic Problems. *SIAM Journal on Numerical Analysis*, 25(2):351--375, 1988.

[81] M. Wheeler, G. Xue, and I. Yotov. A multipoint flux mixed finite element method on distorted quadrilaterals and hexahedra. *Numerische Mathematik*, 121:165--204, 2012.

[82] M. F. Wheeler and I. Yotov. A posteriori error estimates for the mortar mixed finite element method. *SIAM journal on numerical analysis*, 43:1021--1042, 2005.